Lattice Bhatnagar-Gross-Krook studies of hydrodynamic and thermohydrodynamic internal pressure-driven flows.

WHITE, Darren M.

REFERENCE

LATTICE BHATNAGAR-GROSS-KROOK STUDIES OF HYDRODYNAMIC AND THERMOHYDRODYNAMIC INTERNAL PRESSURE-DRIVEN FLOWS.

DARREN MARK WHITE, BSc (Hons.), Grad. Inst. Phys.

A thesis submitted in partial fulfilment of the requirements

of Sheffield Hallam University for the degree of

Doctor of Philosophy

21 September, 1999

Materials Research Institute, Sheffield Hallam University

in collaboration with Rolls Royce & Associates, Derby.

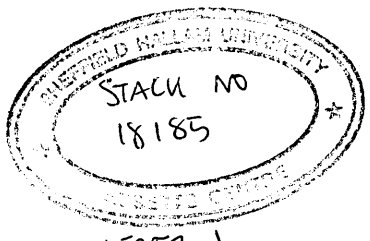
SHEFFIELD HALLAM UNIVERSITY
STACK NO
18185
LEVEL 1

Abstract

In this thesis we develop applications of Lattice-Bhatnagar-Krook (LBGK) models to incompressible flow problems.

We show that in geometries where flow is forced via application of a pressure difference, a modified Exactly Incompressible LBGK (EILBGK) scheme must be applied if significant pressure variations occur. We analyse the model's representation of the no-slip wall boundary condition for flow in a straight duct and recover a friction factor in excellent agreement with theory. Simulation of flow over a backward-facing step produces good agreement with other numerical techniques.

We propose two new LBGK schemes, one directed towards the calculation of depth-averaged flow quantities and the other which focusses on thermal flows in the Boussinesq-Oberbeck limit.

Depth-averaged flow facilitates the two-dimensional simulation of three-dimensional ducts of constant depth. The effect of the unmodelled dimension is accounted for by including momentum sinks in the momentum equations. We apply the scheme to flow in a bifurcating duct and results are again in good agreement with other numerical methods.

We develop a thermal model in which energy is treated efficiently as a passively advected scalar quantity. This approach results in a model which is more simple

and robust than other previously reported LBGK thermal models. Our scheme is then validated by application to flow in a straight duct with constant heat flux applied at the walls. Excellent agreement with theoretical predictions is obtained for the calculated Nusselt number.

Acknowledgements

I would like to express my thanks to the following people who have helped me complete my research. Firstly, my supervisors Dr. I. Halliday and Prof. C. M. Care, and also Dr. A. Stevens from Rolls Royce & Associates.

The Materials Modelling Group within the Materials Research Institute has been a most enjoyable place to work and study, and I must thank everybody who has been part of the group during my time there.

My final expression of gratitude is directed towards my parents and Miriam who have always given me their unreserved support and encouragement.

Contents

Chapter 1

Introduction

The flow of fluids has been extensively studied since fluids impact on so many different aspects of everyday life. Until the early 1960's fluid mechanics was studied either by purely experimental or purely theoretical means. Analytical solutions of theoretical models often required simplified calculations and failed to include all the requisite physics of the flow [1]. Then came computational fluid dynamics (CFD). In the 1960's, mathematical advances and increased computational power allowed the numerical solution of the *exact* governing equations. The computer simulation of flows involving many different physical phenomena became possible and as a result CFD became *and remains* a popular and useful tool for many engineers.

CFD has also had an effect on fluid experiments, which have traditionally played a very important role in the design of systems which depend on flow behaviour. For example, wind tunnels are an effective, but increasingly expensive and time consuming,

way to study scale models of large systems like aircraft or cars. A CFD calculation, for example, can allow an engineer to test many different configurations relatively quickly and economically, thus reducing the amount of final experimentation which needs to be carried out. This example helps to emphasise how CFD complements the traditional approaches of theory and experiment, and although it is an immensely powerful and useful technique it probably will never replace experiment completely.

Compared to lattice Boltzmann (LB) techniques, traditional computational fluid dynamics is a mature subject. As a result it has been developed for many different types of flows, including incompressible and compressible flows, subsonic and supersonic flows, laminar and turbulent flows, as well as multi-component and chemically reacting flows.

LB methods, introduced as an alternative to lattice gas cellular automata (LGCA), are consequently viewed in quite a sceptical light by many fluid dynamicists. Such models are often considered a novel technique offering no real advantage over the traditional methods. This however is not true, and a testament to this is the ever expanding body of literature on the subject as LB models are applied to different types of flow problems.

The work reported in this text investigates the use of lattice Bhatnagar-Gross-Krook (LBGK) models, a variant of the LB approach, to simulate the governing equations of incompressible internal pressure-driven flows, in contrast to the traditional approaches of discretising the same continuum equations and solving via finite-element or finite-volume techniques.

LB schemes are simplified kinetic models based upon microscopic or mesoscopic processes, so that the averaged microscopic properties obey the desired macroscopic behaviour. In molecular dynamics (MD) simulation every particle is tracked. Although physically realistic, MD is an impractical approach to solving large realistic systems, even with modern powerful computers, since the number of tracked molecules which are required is immense. The LB approach avoids such complications and is based on a very much reduced parameter space. The scheme is also by nature ideally suited to massively parallel machines and the implementation of boundary conditions is relatively simple.

1.1 Aims

Whilst it is acknowledged that LB models will never replace traditional CFD methods, there may be areas in which they can enhance its capabilities and should be viewed as a potentially useful tool in the computer simulation of fluids. The principal aim of this project is to study lattice Bhatnagar-Gross-Krook (LBGK) models, a variant of the LB approach, when applied to flow geometries of engineering importance in an attempt to prove the usefulness of the technique.

Thus we apply LBGK models to the simulation of pressure-driven incompressible flows up to moderate Reynolds number in industrially-relevant geometries, via a careful study of the detail of the boundary conditions. Pursuing the theme of industrial relevance, we also aim to develop a thermal LBGK model which is adapted

to flows containing negligible viscous dissipation and so can be applied to certain problems of engineering importance. In the next section we discuss the detailed structure of this thesis which describes the work carried out in order to achieve the above aims.

1.2 Outline of Thesis

The governing hydrodynamic equations which we seek to solve via our LBGK simulations are introduced in chapter 2. These are the incompressible continuity and Navier-Stokes equations, an appropriate energy equation and (for some applications) the equations describing depth-averaged flows. In chapter 3 we introduce lattice gas cellular automata (LGCA), based upon the seminal work of Frisch *et al* [2] in the mid 80's. We then follow the key developments which have led to LBGK models, although, LBGK models tend now to be viewed apart from their parent automata schemes.

In chapter 4 we develop the LBGK models used. We present the theory and fully derive the macroscopic governing equations for the standard $D2Q9$ LBGK model, as introduced by Qian *et al* [3], then proceed to explain a modified exactly incompressible LBGK (EILBGK) scheme. The use of this section is of central importance when simulating internal pressure-driven flow. Also in chapter 4 we detail two schemes not previously reported in the literature which have been developed during the project. Firstly, an EILBGK scheme suitable for the simulation of depth-averaged flows, and,

secondly a novel thermal LBGK scheme incorporating a separate energy variable.

Results of simulations applied to the problem of internal pressure-driven flows are presented in chapter 5. We apply an EILBGK scheme to a backward-facing step, carefully considering the applied boundary conditions, and make comparisons with both traditional CFD and experiment up to intermediate Reynolds numbers.

In chapter 6 we validate our depth-averaged EILBGK scheme numerically, then apply the model to flow in a bifurcating duct and make comparisons with some standard CFD results.

Finally we present, in chapter 7, results of our thermal LBGK model. We apply the scheme to a forced convection flow problem and again make comparisons with analytical solutions and standard CFD results.

Conclusions and suggestions for further work are presented in chapter 8.

Chapter 2

Hydrodynamic Governing Equations

Since we shall be making arguments based upon the microscopic origin of the governing equations of hydrodynamics it is appropriate, for the sake of producing a coherent account, to describe how the macroscopic motion of fluids is modelled and to provide an overview of derivations of key equations governing fluid flow.

Clearly our treatment cannot be exhaustive. Moreover, we shall focus upon those approximations within the system of fluid momentum, continuity and energy equations which are relevant to our applications of internal pressure-driven flow up to moderate Reynolds number (in the limit of negligible viscous dissipation) and upon which we rely in later sections.

The present chapter is also the most appropriate place to develop some non-standard

theoretical results, which we propose to use subsequently without further justification.

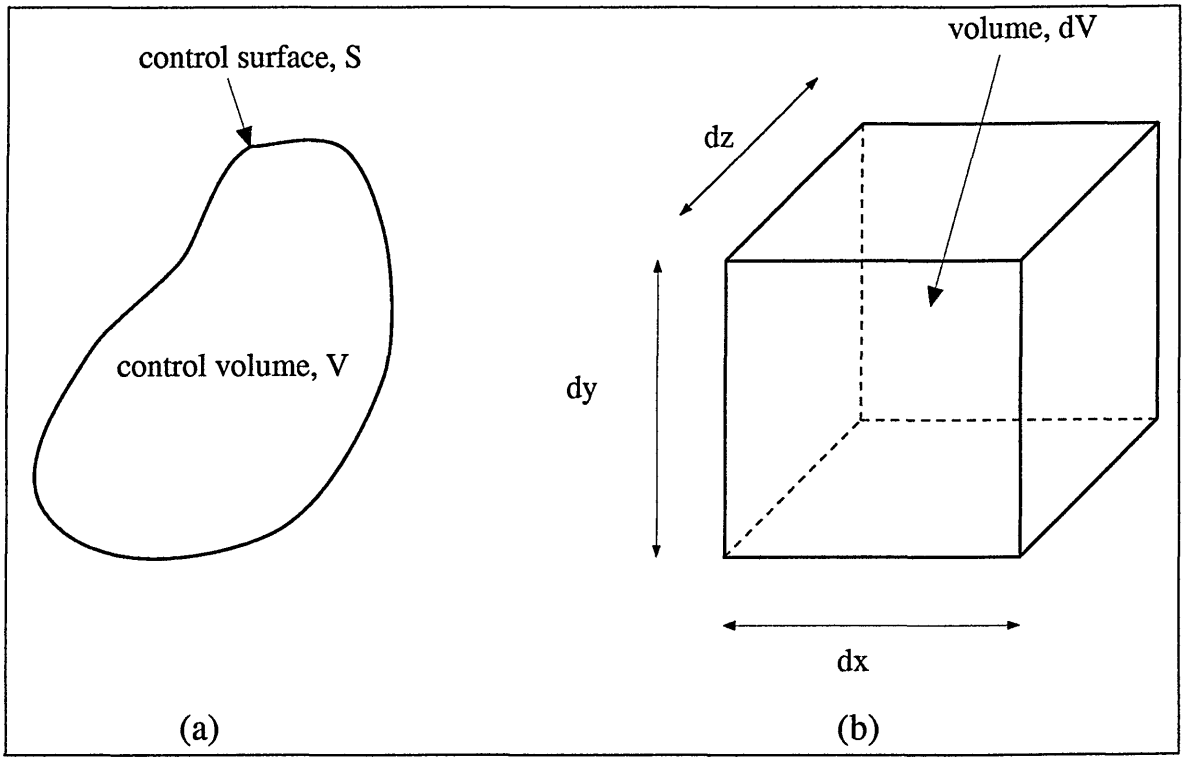

Figure 2.1: Flow models used in deriving macroscopic governing equations.(a)Control volume, V, bounded by control surface, S. (b)Fluid element of volume, dV.

The macroscopic governing equations can be obtained using various different flow models, see fig 2.1, which consider either a control volume, V, bounded by a control surface, S, or an infinitesimal fluid element of volume dV. Either of these models can be static, with the fluid moving through it, or the volume can move with the fluid (the same fluid atoms always being contained within the volume). The governing equations obtained from the various models differ in form, but are none the less equivalent and can be transformed from one to the other by relatively simple algebraic manipulations.

Whether models of type (a) or (b) of figure 2.1 are used, the volume considered is large enough to contain many millions of atoms of the fluid, yet very small compared with the scale of the problem.

A system of five equations is required in order to completely describe the motion of a fluid. These are

1. the continuity equation,
2. the Navier-Stokes equations (3 equations),
3. the energy equation.

2.1 Continuity Equation

The continuity equation is a mathematical expression of the law of conservation of mass. Consider a fluid element of some volume V_o. The mass of fluid flowing through an elemental area of $d\mathbf{A}$ in unit time will be,

$$\rho \mathbf{v} \,.\, d\mathbf{A} \,, \tag{2.1}$$

where $\mathbf{v}$ is fluid velocity.

The vector $d\mathbf{A}$ has magnitude equal to the area of the surface element and its direction is along the normal. The total mass that will be flowing out of the volume, V_o, enclosed by the surface S, in unit time is

$$\iint_S \rho \mathbf{v} \,.\, d\mathbf{A} \,, \tag{2.2}$$

and the decrease in unit time of mass inside V_o is,

$$-\frac{\partial}{\partial t}\iiint_{V_o} \rho \, dV \; . \tag{2.3}$$

Mass must be conserved so (2.2) and (2.3) are equated to give,

$$-\frac{\partial}{\partial t}\iiint_{V_o} \rho \, dV = \iint_{S} \rho \mathbf{v} \, . \, d\mathbf{A} \; . \tag{2.4}$$

The surface integral of (2.4) can be transformed into a volume integral using the Divergence Theorem, so we write (2.2) as,

$$\iint_{S} \rho \mathbf{v} \, . \, d\mathbf{A} = \iiint_{V_o} \nabla . \rho \mathbf{v} \; dV \; . \tag{2.5}$$

Therefore, (2.4) becomes

$$\iiint_{V_o} \left[\frac{\partial \rho}{\partial t} + \nabla . \rho \mathbf{v} \right] dV = 0 \; , \tag{2.6}$$

which must hold for any volume, so the integrand disappears to give,

$$\frac{\partial \rho}{\partial t} + \nabla . (\rho \mathbf{v}) = 0 \; , \tag{2.7}$$

which is the equation of continuity. In tensor notation, with the usual implied Einstein summation convention on repeated Greek subscripts, (2.7) becomes,

$$\frac{\partial \rho}{\partial t} + \partial_\alpha \rho v_\alpha = 0 \; . \tag{2.8}$$

2.2 Euler's Equation

Euler's equation describes the motion of a perfect fluid, ie. a fluid with no internal friction (viscosity), and which is thermodynamically reversible. The total force

acting upon a volume element in the fluid is the pressure, p, integrated over the entire surface of the volume, and again using the Divergence Theorem this can be expressed as a volume integral as follows,

$$\mathbf{F}_T = -\iint_S p \, d\mathbf{A} = -\iiint_{V_o} \nabla p \, dV \ , \tag{2.9}$$

whereupon $(-\nabla p)$ may be expressed as the force per unit volume,

$$\mathbf{F} = -\nabla p \ . \tag{2.10}$$

Using Newton's second law we can now write an equation of motion for our fluid element,

$$\mathbf{F} = -\nabla p = \rho \, \frac{d\mathbf{v}}{dt} \ . \tag{2.11}$$

The velocity derivative that appears in (2.11) has to be carefully considered. It is not simply the rate of change of velocity at a *fixed* point, but is the rate of change of velocity of the chosen fluid element as it moves about in space, so,

$$\begin{aligned} d\mathbf{v} &= \frac{\partial \mathbf{v}}{\partial t} \, dt + \frac{\partial \mathbf{v}}{\partial x} \, dx + \frac{\partial \mathbf{v}}{\partial y} \, dy + \frac{\partial \mathbf{v}}{\partial z} \, dz \ , \\ &= \frac{\partial \mathbf{v}}{\partial t} \, dt + (d\mathbf{r}.\nabla)\, \mathbf{v} \ , \\ \frac{d\mathbf{v}}{dt} &= \frac{\partial \mathbf{v}}{\partial t} + (\mathbf{v}.\nabla)\, \mathbf{v} \ . \end{aligned} \tag{2.12}$$

In more conventional CFD (2.12) is often referred to as the substantive derivative, and using this result in (2.11), we obtain,

$$\frac{\partial \mathbf{v}}{\partial t} + (\mathbf{v}.\nabla)\, \mathbf{v} = -\frac{1}{\rho} \nabla p \ . \tag{2.13}$$

This is Euler's equation, and may be written in tensor form as,

$$\frac{\partial v_\alpha}{\partial t} + v_\beta \partial_\beta v_\alpha = -\frac{1}{\rho} \partial_\alpha p \ , \tag{2.14}$$

or, alternatively,

$$\frac{\partial(\rho v_\alpha)}{\partial t} = -\partial_\beta \Pi_{\alpha\beta} \ , \tag{2.15}$$

$$\Pi_{\alpha\beta} \equiv p\delta_{\alpha\beta} + \rho v_\alpha v_\beta \ , \tag{2.16}$$

where $\Pi_{\alpha\beta}$, the momentum flux tensor, is considered further in section 2.3.

2.3 Momentum Flux Tensor

The momentum of a unit volume is simply $\rho\mathbf{v}$. Its rate of change of momentum can be written,

$$\frac{\partial(\rho v_\alpha)}{\partial t} = \rho\frac{\partial v_\alpha}{\partial t} + v_\alpha\frac{\partial \rho}{\partial t} \ . \tag{2.17}$$

If the continuity equation (2.8) and Euler's equation (2.14) are substituted in (2.17), the following results,

$$\begin{aligned}
\frac{\partial(\rho v_\alpha)}{\partial t} &= -\rho v_\beta \partial_\beta v_\alpha - \partial_\alpha p - v_\alpha \partial_\beta (\rho v_\beta) \ , \\
&= -\partial_\alpha p - \partial_\beta (\rho v_\alpha v_\beta) \ , \\
&= -\partial_\beta (p\delta_{\alpha\beta} + \rho v_\alpha v_\beta) \ , \\
&= -\partial_\beta \Pi_{\alpha\beta} \ .
\end{aligned} \tag{2.18}$$

The physical meaning of $\Pi_{\alpha\beta}$ is that it is the α-component of the momentum flowing in unit time through unit area in direction perpendicular to the β-axis [4].

2.4 Navier-Stokes Equations

To derive the equations which govern the momentum of a viscous fluid, the effect of viscous dissipation must be included by adding additional terms to the equation which describes the motion of a perfect fluid: Euler's equation. The continuity equation does not require any modification, as it is correct for both perfect and viscous fluids.

A viscous fluid is one in which there is an irreversible dissipation of momentum: momentum diffuses from positions in the fluid where the momentum is larger to positions where it is smaller. Internal friction must reduce the momentum flux per unit area, so the momentum flux tensor $\Pi_{\alpha\beta}$, (2.16), is redefined as,

$$\Pi_{\alpha\beta} \rightarrow \Pi_{\alpha\beta} - \sigma'_{\alpha\beta} , \tag{2.19}$$

where $\sigma'_{\alpha\beta}$ is the term that accounts for the dissipation of momentum within the fluid and is known as the *viscosity stress tensor.*

Viscous type processes only occur where there are velocity *gradients* within the fluid. If the velocity gradients are small it is assumed that $\sigma'_{\alpha\beta}$ is dependent only on the first derivatives of velocity, and it is a *linear* function of combinations of $\partial_\beta v_\alpha$, which will be zero when the fluid is in uniform motion.

A fluid should also be free of viscous effects when it is in uniform rotation. If such a fluid has angular velocity ω at a point $\mathbf{r}$ the velocity at that point is given by,

$$\mathbf{v} = \omega \wedge \mathbf{r} .$$

Linear combinations of $(\partial_\alpha v_\beta + \partial_\beta v_\alpha)$ and $\partial_\gamma v_\gamma$ disappear under both uniform motion, and uniform rotation.

A general second rank tensor linear in velocity gradients, vanishing for a fluid in uniform translation and rotation is,

$$\sigma'_{\alpha\beta} = a\,(\partial_\alpha v_\beta + \partial_\beta v_\alpha) + b\;\partial_\gamma v_\gamma\,\delta_{\alpha\beta}\;, \tag{2.20}$$

which can be expressed alternatively as [4],

$$\sigma'_{\alpha\beta} = \eta\left(\partial_\alpha v_\beta + \partial_\beta v_\alpha - \frac{2}{3}\partial_\gamma v_\gamma\,\delta_{\alpha\beta}\right) + \zeta\partial_\gamma v_\gamma\,\delta_{\alpha\beta}\;, \tag{2.21}$$

where η and ζ are known as the coefficients of viscosity.

The equations describing the motion of a viscous fluid are now obtained by substituting for the modified momentum flux tensor, $\Pi_{\alpha\beta}$, in Euler's equation, (2.15).

$$\partial_t\,(\rho v_\alpha) = -\partial_\beta \Pi_{\alpha\beta} = -\partial_\beta\left(p\,\delta_{\alpha\beta} + \rho v_\alpha v_\beta - \sigma'_{\alpha\beta}\right)\;, \tag{2.22}$$

$$\begin{aligned}\rho\,(\partial_t v_\alpha + v_\beta\partial_\beta v_\alpha) \;=\; & -\partial_\alpha p + \partial_\beta\Big(\eta\Big(\partial_\alpha v_\beta + \partial_\beta v_\alpha \\ & -\frac{2}{3}\,\partial_\gamma v_\gamma\delta_{\alpha\beta}\Big) \\ & +\zeta\partial_\gamma v_\gamma\delta_{\alpha\beta}\Big)\;.\end{aligned} \tag{2.23}$$

The coefficients of viscosity are usually considered to be constants, and as a result of this can be moved in front of the differential operators, leaving

$$\partial_t v_\alpha + v_\beta\partial_\beta v_\alpha = -\frac{1}{\rho}\partial_\alpha p + \nu\partial_\beta^2 v_\alpha + \frac{1}{\rho}\left(\zeta + \frac{1}{3}\eta\right)\partial_\alpha(\partial_\beta v_\beta)\;, \tag{2.24}$$

which are the Navier-Stokes equations, where $\nu = \frac{\eta}{\rho}$ is the kinematic viscosity of the fluid.

2.5 Incompressibility

In many cases an assumption that the fluid under study is incompressible is made. This can be interpreted physically to mean that there is negligible variation in the fluid density, even with large variations in pressure, p, and the density may be assumed constant.

This assumption helps to simplify the equations of motion derived in sections 2.2 and 2.4. For constant density, ρ, the continuity equation becomes,

$$\nabla.\mathbf{v} = 0 \,, \tag{2.25}$$

and the Navier-Stokes equations simplify to give,

$$\frac{\partial \mathbf{v}}{\partial t} + (\mathbf{v}.\nabla)\,\mathbf{v} = -\frac{1}{\rho}\nabla p + \nu\nabla^2\mathbf{v} \,. \tag{2.26}$$

Whilst it is often assumed that ρ does not vary with p, ρ can still vary with temperature T, ie. for the non-isothermal calculations we perform, we shall assume $\rho = \rho(T)$ only.

2.6 Reynolds Number

An important dimensionless quantity is the Reynolds number, Re,

$$Re = \frac{Ul}{\nu} \,, \tag{2.27}$$

where U and l are a characteristic velocity and a characteristic length scale of the flow respectively, the choice of which is arbitrary and depends on the flow geometry.

In laminar duct flow l is often taken to be the hydraulic diameter (to be defined below), and U to be the average velocity across the duct.

The hydraulic diameter, D, is defined as,

$$D = \frac{4A}{P} , \tag{2.28}$$

where A is the cross-sectional area, and P is the wetted duct perimeter. For a 2D rectangular duct of width W (2.28) reduces to,

$$D = 2W . \tag{2.29}$$

The importance of the Reynolds number becomes clear if we consider Reynolds' *law of similarity.* Two different flows of the same type, ie. with a similar boundary geometry, are said to be *dynamically similar* provided they have the same Reynolds number. So, in two scaled ducts with a sudden assymetric expansion (say), one containing air and the other water, two dynamically similar flows are obtained if both systems have equivalent values of *Re*. This *similarity* principle is extensively used in wind tunnel and wave tank experiments to test small models of much larger structures.

If we normalise lengths to be measured on l, and velocities on U, the Navier-Stokes equations in their incompressible form become,

$$\frac{\partial \mathbf{v}^*}{\partial t^*} + (\mathbf{v}^*.\nabla^*)\,\mathbf{v}^* = -\nabla^* p^* + \frac{1}{Re}\nabla^{*^2}\mathbf{v}^* , \tag{2.30}$$

where,

$$Re = \frac{Ul}{\nu} \quad \text{and} \quad p^* = \frac{p}{\rho U^2} ,$$

and all the variables in the above $(\mathbf{r}^*, \mathbf{v}^*)$ are now dimensionless and clearly, for given boundary conditions the solution depends only upon Re. Flows which are *similar* can be obtained from one another by changing the normalisation constants of length and velocity.

2.7 Energy Equation

In this section we establish an appropriate energy equation for our target application of internal pressure-driven flow with negligible viscous dissipation. It is appropriate to consider the fluid equation of state concurrently.

A volume element of inviscid fluid has both kinetic and internal energy, the former being small for our applications,

$$\left(\frac{1}{2}\rho v^2 + \rho\epsilon\right) , \tag{2.31}$$

ε being the internal energy per unit mass.

The rate of change of this energy can be expressed as,

$$\frac{\partial}{\partial t}\left(\frac{1}{2}\rho v^2 + \rho\epsilon\right) . \tag{2.32}$$

To evaluate expression (2.32) we consider first the term due to kinetic energy,

$$\frac{\partial}{\partial t}\left(\frac{1}{2}\rho v^2\right) = \frac{1}{2}v^2\frac{\partial \rho}{\partial t} + \rho\mathbf{v}.\frac{\partial \mathbf{v}}{\partial t} . \tag{2.33}$$

By substitution of continuity (2.7) and Euler's equation (2.14), for the first and second terms on the rhs of (2.33) respectively, and using the following combination

of the first and second laws of thermodynamics,

$$dh = T\,ds + \left(\frac{1}{\rho}\right) dp\ , \tag{2.34}$$

(where h is enthalpy, T temperature and s is the entropy), (2.33) may be written [4],

$$\frac{\partial}{\partial t}\left(\frac{1}{2}\rho v^2\right) = -\frac{1}{2}v^2\nabla.\rho\mathbf{v} - \rho\mathbf{v}.\nabla\left(\frac{1}{2}v^2 + h\right) + \rho T\mathbf{v}.\nabla s\ . \tag{2.35}$$

To find a form for $\frac{\partial(\rho\epsilon)}{\partial t}$ in (2.32) use the first law [4],

$$d\epsilon = T\,ds - p\,dV = T\,ds + \frac{p}{\rho^2}\,d\rho\ ,$$

the definition of *specific* enthalpy $h = \epsilon + \frac{p}{\rho}$ and the fact that flow of an ideal (inviscid) fluid must be adiabatic,

$$\frac{ds}{dt} + \mathbf{v}.\nabla s = 0\ ,$$

so that we can write,

$$\begin{aligned}
\frac{\partial}{\partial t}(\rho\varepsilon) &= \rho\frac{\partial\varepsilon}{\partial t} + \varepsilon\frac{\partial\rho}{\partial t}\ , \\
&= \rho\left\{T\frac{\partial s}{\partial t} + \frac{P}{\rho^2}\frac{\partial\rho}{\partial t}\right\} + \varepsilon\frac{\partial\rho}{\partial t}\ , \\
&= \rho T\left(-\mathbf{v}.\nabla s\right) + \left(\varepsilon + \frac{p}{\rho}\right)\left(-\nabla.\rho\mathbf{v}\right)\ ,
\end{aligned}$$

which leads to the desired expression for $\frac{\partial}{\partial t}(\rho\varepsilon)$,

$$\frac{\partial(\rho\epsilon)}{\partial t} = -h\nabla.\rho\mathbf{v} - \rho T\mathbf{v}.\nabla s\ . \tag{2.36}$$

Combining (2.35) and (2.36) we obtain an expression of the law of conservation of energy for an ideal (inviscid) fluid,

$$\frac{\partial}{\partial t}\left(\frac{1}{2}\rho v^2 + \rho\epsilon\right) = -\nabla.\left(\rho\mathbf{v}\left(\frac{1}{2}v^2 + h\right)\right)\ . \tag{2.37}$$

Energy remains conserved in a viscous fluid of course, but there is now an additional flux of energy due to the internal friction, $\mathbf{v}.\sigma'$ (see below) and an energy flux due to conductive transport, $\mathbf{q}$,

$$\mathbf{q} = -k\nabla T \ , \tag{2.38}$$

where k is the thermal conductivity.

These fluxes, due to viscosity and conduction, may be incorporated into the perfect fluid equation in the obvious way to yield the energy equation for a real fluid,

$$\frac{\partial}{\partial t}\left(\frac{1}{2}\rho v^2 + \rho\epsilon\right) = -\nabla.\left(\rho\mathbf{v}\left(\frac{1}{2}v^2 + h\right) - \mathbf{v}.\sigma' - k\nabla T\right) \ . \tag{2.39}$$

Now, the Navier-Stokes equations, continuity equation and the thermodynamic relationships already discussed may be used, along with the definition of specific enthalpy, to transform the left hand side of (2.39) [4],

$$\begin{aligned}\frac{\partial}{\partial t}\left(\frac{1}{2}\rho v^2 + \rho\epsilon\right) \ &= \ -\nabla.\left(\rho\mathbf{v}\left(\frac{1}{2}v^2 + h\right) - \mathbf{v}.\sigma' - k\nabla T\right) \\ &\quad +\rho T\left(\frac{\partial s}{\partial t} + \mathbf{v}.\nabla s\right) - \sigma'_{ik}\frac{\partial v_i}{\partial x_k} - \nabla\left(k\nabla T\right) \ .\end{aligned} \tag{2.40}$$

From a comparison of the last equation, (2.40), and equation (2.39) it is immediate that [4],

$$\rho T\left(\frac{\partial s}{\partial t} + \mathbf{v}.\nabla s\right) = \sigma'_{ik}\frac{\partial v_i}{\partial x_k} + \nabla.\left(k\nabla T\right) \ , \tag{2.41}$$

which is the general equation of heat transfer. Note that, in the absence of conduction or viscosity the ideal fluid equation of conservation of entropy is recovered. Together with an appropriate equation of state for the flowing fluid, momentum and continuity equations, energy equation (2.41) is sufficient to close the description of any fluid.

Now, it is possible to reduce the mathematical complexity of the formulation provided certain approximations are valid, and we proceed now to consider, so-called *Boussinesq-Oberbeck* flow. Equation (2.41) can be applied to our incompressible fluids after some simplifications. If flow velocity is much lower than the speed of sound, density changes due to pressure variations may be ignored. This incompressible assumption is effectively to assume that the equation of state is such that the density of the fluid is independent of the pressure. *Density, however, cannot be assumed independent of temperature for our applications.* Consequently fluid density variation with temperature cannot always be neglected, even at low flow velocities, and Boussinesq-Oberbeck flow treats density as independent of pressure but dependent upon temperature. Therefore, using,

$$c_p = T\left(\frac{\partial s}{\partial T}\right)_p \quad \text{and,} \quad T\nabla s = c_p \nabla T \ ,$$

equation (2.41) becomes,

$$\rho c_p \left(\frac{\partial T}{\partial t} + \mathbf{v}.\nabla T\right) = \nabla.(k\nabla T) + \sigma'_{\alpha\beta}\partial_\alpha v_\beta \ . \tag{2.42}$$

For small temperature differences η, k and c_p may be assumed constant. If (2.21) is substituted for $\sigma_{\alpha\beta}$ in (2.42), the equation of heat transfer for an incompressible fluid is,

$$\frac{\partial T}{\partial t} + \mathbf{v}.\nabla T = \chi\nabla^2 T + \frac{\nu}{2c_p}\left(\partial_\beta v_\alpha + \partial_\alpha v_\beta\right)^2 \ , \tag{2.43}$$

where the thermal diffusivity, χ, is,

$$\chi = \frac{k}{\rho c_p} \ . \tag{2.44}$$

The contribution from the last term in (2.43) is that due to viscous dissipation, which is the degradation of mechanical into thermal energy caused by the friction of adjacent fluid particles moving past each other. However, in the majority of flow problems this contribution is not important [5], and can be neglected. Indeed, this term is smaller than the conduction term in liquids typically by a factor $\times 10^{-7}$ [6]. Therefore, within the *Boussinesq-Oberbeck* flow approximations, the macrodynamic equation (2.43) reduces further,

$$\partial_t T + \mathbf{v}.\nabla T = \chi \nabla^2 T \ . \tag{2.45}$$

It is central to observe that, in the Boussinesq-Oberbeck equation (2.45) energy apparently behaves as a passively transported scalar quantity, the energy being slaved to the velocity. Only if buoyancy forces were to be included would the temperature be coupled back to the velocity through a buoyancy 'body-force' term in the Navier-Stokes equations.

As with the Navier-Stokes equations we can define dimensionless quantities which characterise flow. One such quantity is the Nusselt number, Nu.

The heat transfer coefficient, h, is defined as,

$$h = \frac{q}{(T_w - T_b)} \ , \tag{2.46}$$

where q is the heat flux, and $(T_w - T_b)$ a characteristic temperature difference between the boundary (wall) and the contacting fluid. The Nusselt number is then defined as,

$$Nu = \frac{hl}{k} \ , \tag{2.47}$$

and is characteristic of the heat transfer (l remains a characteristic length).

Another dimensionless quantity which represents an intrinsic fluid property, not dependent on flow geometry or any other flow property is the Prandtl number, Pr, where,

$$Pr = \frac{\nu}{\chi} = \frac{\eta c_p}{k} . \tag{2.48}$$

2.8 Incompressible Depth-Averaged Flow.

Computationally, full three-dimensional simulations can be extremely demanding and commonly, in an attempt to reduce the complexity of the problem, internal flows in ducts of constant depth are computed in two-dimensions, without explicitly modelling the shallow depth of the duct, see figure 2.2. In CFD the results of such calculations are generally assumed to be *depth-averaged* quantities, and the influence of the 'unmodelled' dimension is accounted for by using different momentum sink terms in the flow momentum equations. In this section we explore the basis of these assumptions and in section 6.2 we proceed to examine the domain of applicability of 2D calculations to laminar flow by numerical calculation.

In the following analysis Greek subscripts refer only to coordinates x and y in the explicitly modelled plane, d denotes physical fluid density, and all other symbols have their usual meaning. Taking isothermal, laminar flow in the shallow duct of constant depth shown in figure 2.2 to be governed by the continuity and incompress-

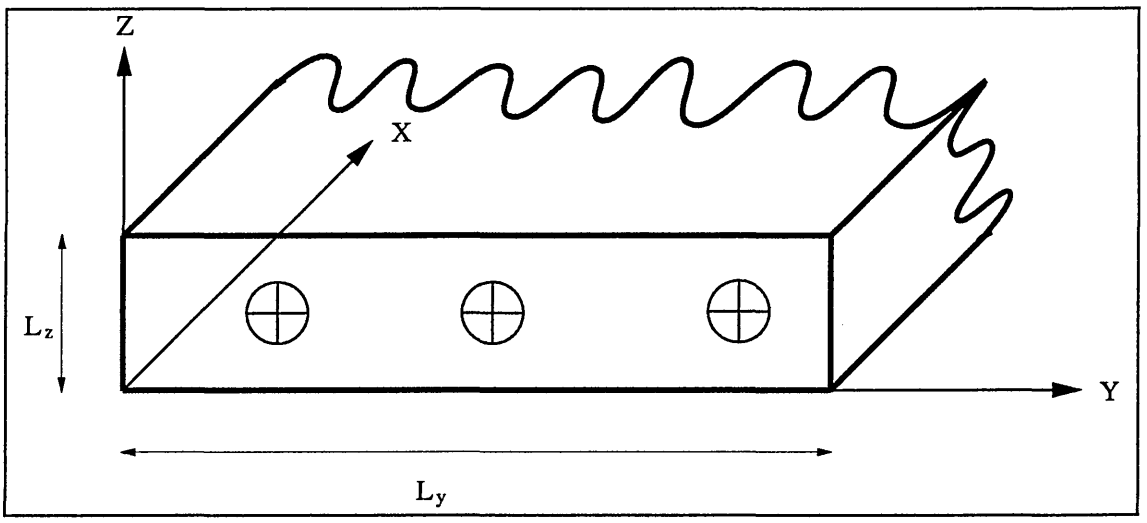

Figure 2.2: Geometry of depth-averaged flow problem.

ible Navier-Stokes equations (written in conservation form [1]) one may perform a z-integration to yield,

$$\partial_t \overline{v_\alpha} + \partial_\beta \overline{v_\alpha v_\beta} + \frac{1}{L_z}\left[v_z v_\alpha\right]_0^{L_z} = -\partial_\alpha\left(\frac{\overline{p}}{d}\right) + \nu \partial_\beta \partial_\beta \overline{v_\alpha} + \frac{\nu}{L_z}\left(\partial_z v_\alpha|_{z=L_z} - \partial_z v_\alpha|_{z=0}\right) , \tag{2.49}$$

$$\partial_\beta \overline{v_\beta} + \frac{1}{L_z}\left[v_z\right]_0^{L_z} = 0 , \tag{2.50}$$

where the overbar denotes a *depth-average* quantity,

$$\overline{v_\alpha} = \frac{1}{L_z}\int_0^{L_z} v_\alpha(x,y,z)\, dz . \tag{2.51}$$

Invoking no-slip boundary conditions on velocity in equations (2.49) and (2.50), $v_\alpha = 0 \ \forall \ \alpha$ at $z = 0, L_z$, a pseudo two-dimensional system is formed, in which, controlling the depth-averaged quantities, are the incompressible continuity equation *exactly* and a momentum equation *similar in form to* the incompressible Navier-

Stokes equations with an additional momentum sink,

$$\partial_\beta \overline{v_\beta} = 0 , \tag{2.52}$$

$$\partial_t \overline{v_\alpha} + \partial_\beta \overline{v_\alpha v_\beta} = -\partial_\alpha \left(\frac{\overline{p}}{d} \right) + \nu \partial_\beta \partial_\beta \overline{v_\alpha} + \frac{1}{L_z} S_\alpha , \tag{2.53}$$

where,

$$S_\alpha \equiv \nu \frac{\partial v_\alpha}{\partial z}\bigg|_{z=L_z} - \nu \frac{\partial v_\alpha}{\partial z}\bigg|_{z=0} . \tag{2.54}$$

We now proceed to define,

$$C_{\alpha\beta} = \overline{v_\alpha}\ \overline{v_\beta} - \overline{v_\alpha v_\beta} , \tag{2.55}$$

which enables (2.53) to be written,

$$\partial_t \overline{v_\alpha} + \partial_\beta \overline{v_\alpha}\ \overline{v_\beta} = \partial_\alpha \left(\frac{\overline{p}}{d} \right) + \nu \partial_\beta \partial_\beta \overline{v_\alpha} + \partial_\beta C_{\alpha\beta} + \frac{S_\alpha}{L_z} . \tag{2.56}$$

Evidently the depth-averaged velocity and pressure fields are governed by the equations of two-dimensional fluid flow with an effective body force of the particular form,

$$\partial_\beta C_{\alpha\beta} + \frac{S_\alpha}{L_z} . \tag{2.57}$$

The second *stress* term represents the influence of the unmodelled surfaces, and the first *cumulant* term an inertial discrepancy. By considering the case of unidirectional flow parallel to the x-direction, characterised by a peak (central) velocity u_0, it is possible to obtain order of magnitude estimates for the two terms in (2.57),

$$\begin{aligned} \frac{1}{L_z} S_\alpha &\sim \frac{1}{L_z} \nu \frac{u_0}{L_z} = \frac{\nu u_0}{L_z^2} , \\ \partial_\beta C_{x\beta} &\sim \frac{u_0^2}{L_y} , \end{aligned} \tag{2.58}$$

from which a comparison of the stress and cumulant terms follows,

$$\frac{S_\alpha / L_z}{\partial_\beta C_{x\beta}} \sim \frac{\nu u_0}{L_z^2} \frac{L_y}{u_0^2} = \frac{1}{Re} A \ , \tag{2.59}$$

where $\mathrm{Re} = \frac{L_z u_0}{\nu}$ is the Reynolds number, calculated from the unmodelled depth, and $A \equiv \frac{L_y}{L_z}$ is the aspect ratio of the duct cross-section. Supported by the results of section 6.2, it becomes clear from (2.59) that, for ducts of sufficiently large aspect ratio, the effective body force impressed on the two-dimensional fluid may be approximated by the stress term S_α of expression (2.57) *alone*. (This observation is relevant to the development of our EILBGK scheme (section 4.3) and is further investigated by numerical techniques in section 6.2.) Our depth-averaged governing equation reduces to,

$$\partial_t \overline{v_\alpha} + \partial_\beta \overline{v_\alpha}\ \overline{v_\beta} = \partial_\alpha \left(\frac{\overline{p}}{d} \right) + \nu \partial_\beta \partial_\beta \overline{v_\alpha} + \frac{S_\alpha}{L_z} \ , \tag{2.60}$$

for large values of aspect ratio A.

For ducts in which aspect ratio A is sufficiently large, we aim to simulate in *two-dimensions* the parent three-dimensional flow, sampled across the unmodelled z-direction and take the flow to exhibit that parabolic velocity profile which is a solution of the incompressible Navier-Stokes equation for flow parallel to two parallel-plane walls,

$$v_x(yz) = \frac{4u_0}{L_z^2} z \left(L_z - z \right) \ , \tag{2.61}$$

where, of course, u_0 depends upon the applied pressure gradient [4]. One may now obtain from (2.61) expressions for the derivatives in definition (2.54),

$$\nu \left. \frac{\partial v_x}{\partial z} \right|_{z=L_z} - \nu \left. \frac{\partial v_x}{\partial z} \right|_{z=0} = -\frac{4\nu u_0}{L_z} \ . \tag{2.62}$$

In the last equation u_0 may be eliminated in favour of z-averaged velocity, obtained from (2.61), whereupon we obtain from (2.52) and (2.53) the equations governing pseudo two-dimensional flow in a shallow duct of large aspect ratio at steady-state,

$$\partial_\beta \overline{v_\beta} = 0 , \tag{2.63}$$

$$\partial_\beta \overline{v_\alpha}\, \overline{v_\beta} = -\partial_\alpha \left(\frac{\overline{p}}{d} \right) + \nu \partial_\beta \partial_\beta \overline{v_\alpha} - \frac{12\nu}{L_z^2} \overline{v_\alpha} , \tag{2.64}$$

where an overbar denotes averaging over the shallow z-direction, Greek subscripts refer only to x, y and the velocity dependent body force in the rhs has its origin in the stresses from the unmodelled surfaces. In section 4.3 we make appropriate modifications to an EILBGK scheme which move its governing macroscopic equations towards equations (2.63) and (2.64).

Chapter 3

Lattice Gases and Lattice Boltzmann Models

3.1 Introduction

In this chapter we seek to outline the key developments leading to the kind of LBGK models used in this thesis. We start with a review of lattice gas cellular automata (LGCA), since lattice Boltzmann (LB) models have evolved from them (though LB models are now viewed apart from their parent automata). Notably, it has even been shown recently, by He *et al* [7], that the LB algorithms can be obtained directly from the continuum Boltzmann equation. (The Boltzmann equation is a differential equation which describes the behaviour of a dilute gas, a gas in which collisions involving more than two particles are neglected.)

3.2 Lattice Gas Cellular Automata

In 1986 Frisch *et al* [8] showed they were able to construct a simple automaton which was able to simulate both 2D and 3D Navier-Stokes equations. They extended earlier work of Hardy, Pazzis and Pomeau [9] who had constructed an automaton, known as the HPP model, based on monoenergetic particles propagating and colliding on a square lattice, that was suitable for modelling certain physical phenomena (for example sound waves) but failed to recover the Navier-Stokes equations - a lack of sufficient symmetry and the conservation of spurious quantities being to blame.

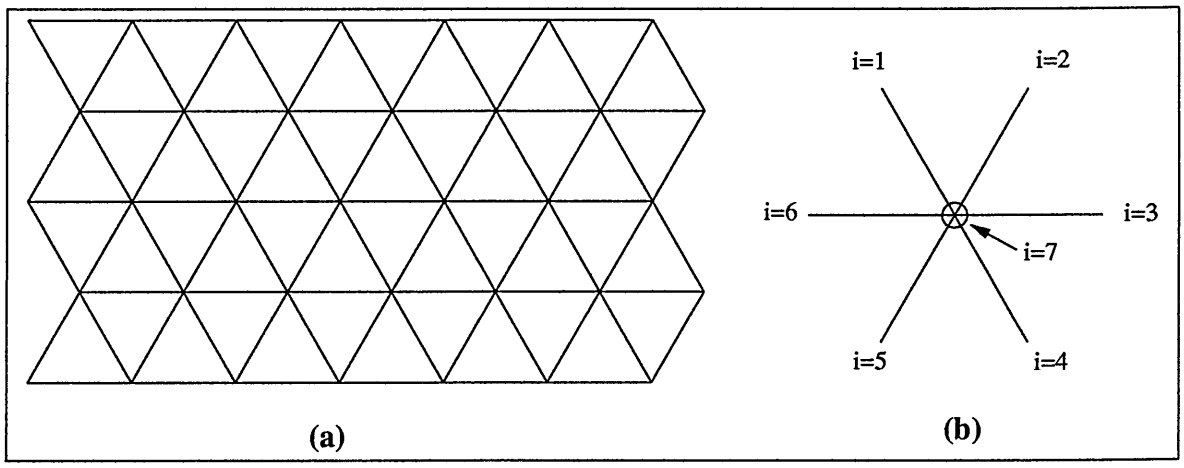

Figure 3.1: a) Hexagonal lattice for FHP model. b) FHP unit cell.

Frisch *et al* found that 'up-grading' to a hexagonal lattice introduced sufficient symmetry to recover equations similar in form to the Navier-Stokes equations (with constraints on particle number density and simulated flow Mach number).

In the simplest 'FHP1' [2] cellular automaton, each node of the lattice, figure 3.1(a),

is joined to its nearest neighbours by six velocity vectors, referred to as lattice links, ($\mathbf{c}_i$, where $i = 1 \ldots 6$), there being 6 allowed velocities on a hexagonal lattice. 'Boolean' particles, of unit mass and velocity, populate the lattice and move along the links, residing at the nodes at the end of each integer timestep, subject to an exclusion principle. Only one particle may move along a particular link during any time step, which leads to a Fermi-Dirac equilibrium distribution.

The evolution of the lattice proceeds in two phases, propagation followed by collision. During the propagation phase each particle moves one lattice link, to the nearest node towards which its velocity was pointing,

$$n_i(\mathbf{r} + \mathbf{c}_i, t + 1) = n_i(\mathbf{r}, t) \ , \tag{3.1}$$

where,

$$n_i = \begin{cases} 1 & \text{for link } i \text{ being } \textit{occupied} \ , \\ 0 & \text{for link } i \text{ being } \textit{unoccupied} \ . \end{cases}$$

During the next stage of evolution collisions are applied at lattice nodes, which conserve both mass and momentum. See figure 3.2, which shows two and three particle interactions. Many more collisions which conserve the required properties are possible, including in 'FHP2' [2] collisions with rest particles, which remain at the node during each time step, see $i = 7$ in figure 3.1, and are discussed at length in the literature (see [2] for example). The effect of collision is incorporated into the evolution equation as follows,

$$n_i(\mathbf{r} + \mathbf{c}_i, t + 1) = n_i(\mathbf{r}, t) + \Delta_i(n) \ . \tag{3.2}$$

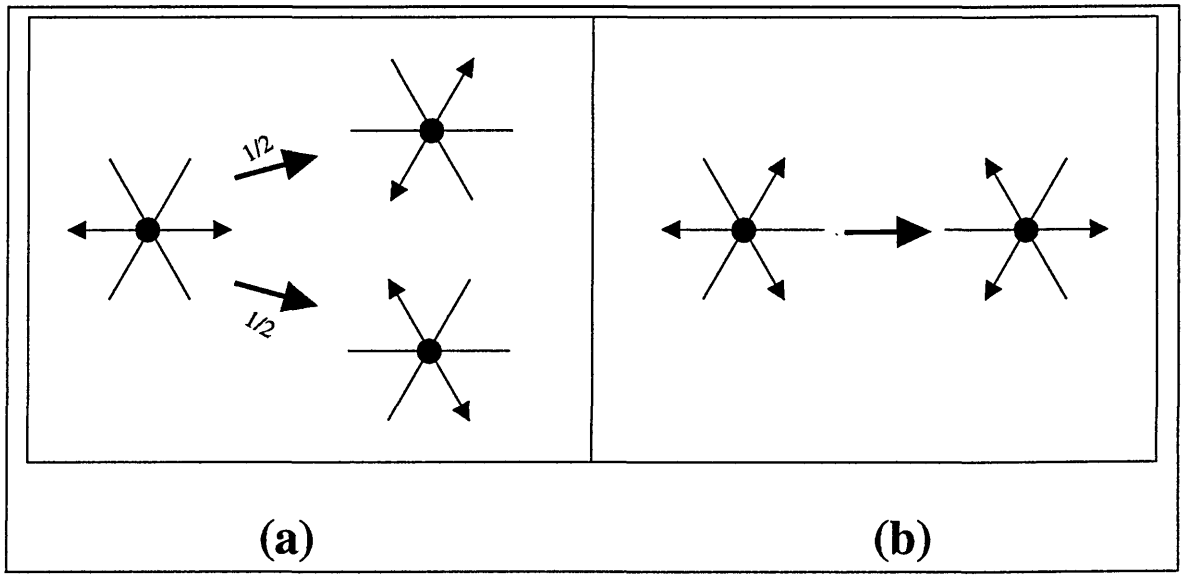

Figure 3.2: a) Two particles collision, two equally possible output states. b) Three particle interaction.

The collision operator, $\Delta_i(n)$, will take the possible values of -1, 0 or $+1$, describing the effect of collision on link i as either losing a particle, having no effect or gaining a particle. For speed, the collision operator relies on lookup tables which contain the probability, A, that an input state $s = \{s_i,\ i = 1 \ldots 7\}$ will be *collided* into an output state $s' = \{s'_i,\ i = 1 \ldots 7\}$, and,

$$A\left(s \rightarrow s'\right) \geq 0\,, \tag{3.3}$$

$$\sum_{\forall s'} A\left(s \rightarrow s'\right) = 1\,. \tag{3.4}$$

Importantly, for lattice gases it is necessary, in order to capture macroscopic hydrodynamic behaviour, that collisions between more than two fluid particles be incorporated [10].

The full collision operator can be shown to have the form [2],

$$\Delta_i(n) = \sum_{s,\ s'} \left(s'_i - s_i\right) \xi_{ss'} \prod_j n_j^{s'_j} \left(1 - n_j\right)^{(1-s_j)}\,, \tag{3.5}$$

where $\xi_{ss'}$ is a boolean scattering matrix, the elements of which take values of 1 or 0, denoting whether a transition $s \rightarrow s'$ is allowed. It is defined as,

$$\langle \xi_{ss'} \rangle = A\left(s \rightarrow s'\right) \ . \tag{3.6}$$

Simulation observables are calculated from ensemble averages over both time and space, the mean population $N_i(\mathbf{r}, t)$ being given by,

$$N_i(\mathbf{r}, t) = \langle n_i \rangle \ .$$

Density and momentum are respectively defined as,

$$\rho(\mathbf{r}, t) = \sum_i N_i(\mathbf{r}, t) \ , \tag{3.7}$$

$$\rho(\mathbf{r}, t)\mathbf{u} = \sum_i N_i(\mathbf{r}, t)\mathbf{c}_i \ . \tag{3.8}$$

These macroscopic observables can be shown to obey hydrodynamic type behaviour, ie. to be governed by 'macroscopic' equations similar to Navier Stokes and continuity, (3.9) and (3.10) respectively.

$$\partial_t \rho + \partial_\beta \left(\rho u_\beta\right) = 0 \ , \tag{3.9}$$

$$\begin{aligned} \partial_t \left(\rho u_\alpha\right) + \partial_\beta \left(g(\rho)\rho u_\alpha u_\beta\right) &= -\partial_\alpha \left(c_s^2 \rho \left(1 + g(\rho)\frac{u^2}{c^2}\right)\right) \\ &\quad + \nu(\rho)\partial_\beta^2 \left(\rho u_\alpha\right) \\ &\quad + \left(\nu(\rho) - \frac{2}{D}\right)\partial_\alpha \partial_\beta \left(\rho u_\beta\right) \ . \end{aligned} \tag{3.10}$$

Derivations are not presented here, as it is beyond the scope of this thesis (see [2] and [11]), although reference to these ideas will be made in section 4.1. The 'FHP' models have an unphysical density dependent factor $g(\rho)$ in front of the inertial term in the *lattice* Navier-Stokes equations (3.10), which makes the model non-Galilean

invariant [2]. Moreover, the pressure, first term on the lhs of (3.10), is unphysically velocity dependent. In (3.10) c_s^2 is the speed of sound, ν is kinematic viscosity function (dependent on ρ) and D the number of dimensions.

The Navier-Stokes equations are obeyed by fluids, so why is it that particles colliding and propagating on a regular lattice should also obey the same set of macroscopic governing equations? Different fluids have different intermolecular force laws, but the collisions undergone by these dissimilar fluid particles all conserve both mass and momentum. Physically LGCA's seem to tell us that it is the conservation of these quantities which allow LGCA models to recover hydrodynamic behaviour. If internal energy is also conserved during collision equations similar to the heat equation are also recovered [12].

Lattice gases have many attractive properties. Due to their integer arithmetic they have no round off error, are unconditionally stable, are ideal for parallel processing and complex boundary conditions are easily incorporated. They do however also have many unattractive properties - principally statistical noise. It is necessary to average over large regions of the lattice, long times and many initial configurations to extract 'observables' (3.7) and (3.8). This is especially true when calculating quantities such as vorticity, which involve derivatives [13]. Moreover, collision rules can become extremely complex when more links are added, and, regular three dimensional lattices with enough symmetry to ensure isotropy do not exist. (However, a four dimensional model known as FCHC - face-centred hypercubic unit cell with unit periodicity in the fourth dimension, consequently only pseudo 3D - with 24

links exists, but collisions can only be dealt with by special computer hardware or extremely large lookup tables.) The complexity of LGCA models roughly double with each link added [14]. The requirement for the governing equations to be Galilean invariant is also not easily satisfied.

In subsequent sections we discuss how taking a lattice Boltzmann Equation approach has helped to overcome these disadvantages of LGCA schemes, *whilst retaining most of the advantages.*

3.3 Lattice Boltzmann Approaches

McNamara *et al* [15] used the Boltzmann *molecular chaos* assumption, which neglects the correlations between particles entering a collision (colliding particles have no prior effect on each other). This assumption is applied to ordinary gases of low density, where the mean-free path is very large (so that most particles come from distant uncorrelated regions). Particles which have collided will undergo many other collisions with different particles before they meet again and any correlation from the first collision will have been lost before a second. Frisch *et al* [2] in their work on lattice gases noted this approach appeared to have *a very broad validity* and may not be restricted to low densities. Assuming molecular chaos allows the n_i's to be replaced by single-particle distribution functions, which represent real ensemble averages over a conceptually infinite number of equivalent systems. These averages are denoted by N_i.

The evolution equation which describes propagation and collision can be written as,

$$N_i(\mathbf{r}+\mathbf{c}_i, t+1) = N_i(\mathbf{r}, t) + \Delta_i(N) \ , \tag{3.11}$$

where $\Delta_i(N)$ is calculated by simply replacing the n_i's in the LGCA form with the ensemble averaged N_i's. Equation (3.11) is used directly, without averaging, since the N_i's *are* the ensemble averages, and hence free from statistical fluctuations. Equation (3.11) is the *lattice Boltzmann equation*, so called because a first order Taylor expansion of what is essentially a finite difference equation yields an equation similar in overall form to the continuum Boltzmann equation of kinetic theory [16],

$$\partial_t N_i + \mathbf{c}_i.\nabla N_i = \Delta_i(N) \ . \tag{3.12}$$

There are two key differences between the continuum Boltzmann equation and its lattice variant. Obviously the latter is defined on discrete spaces, but it also considers collisions between more than two particles.

A lattice Boltzmann approach eliminates statistical noise but retains the complex collision operator used in the equivalent LGCA models, rendering it inefficient for true 3D simulation, nevertheless, in [15] it is shown that this approach accurately (within 5%) predicts the decay of shear and sound waves.

In 1989 Higuera *et al* [17] added the assumption that the distribution function is close to the equilibrium state, which allows the collision operator to be *linearised* and hence simplified. N_i is expanded as,

$$N_i = N_i^{eq}(\rho, \mathbf{v}) + N_i^{neq}(\nabla\rho, \nabla\mathbf{v}) \ , \qquad N^{eq} \gg N^{neq} \ , \tag{3.13}$$

where N_i^{eq} is the equilibrium distribution function (for a uniformly translating fluid), which is discussed in more detail in section 4.1, and is dependent on the local values of ρ and $\mathbf{v}$. N_i^{neq} is the non-equilibrium contribution and can be expanded in powers of the velocity components,

$$N_i^{neq} = N_i^{(1)} + N_i^{(2)} + O(v^3) \ , \tag{3.14}$$

where the superscripts on the N_i's refer to the order of $\nabla \mathbf{v}$. Non-equilibrium contributions are at most $O\left(N^{(2)}\right)$ for non-linear hydrodynamic regime [17]. The collision operator is Taylor expanded about equilibrium to give,

$$\Delta_i(N) = \Delta_i\left(N_i^{eq}\right) + \sum_j \frac{\partial \Delta_i}{\partial N_j}\left(N_j^{(1)} + N_j^{(2)}\right) + \frac{1}{2}\sum_{j,\,k} \frac{\partial^2 \Delta_i}{\partial N_j N_k}\left(N_j^{(1)} N_j^{(1)} + ...\right) \ , \tag{3.15}$$

where all derivatives are evaluated at $N_j = N_j^{eq}$.

Using the requirement that,

$$\Delta_i\left(N_i^{eq}\right) = 0 \ , \tag{3.16}$$

(3.15) reduces to,

$$\Delta_i(N) \approx \sum_j \frac{\partial \Delta_i}{\partial N_j}\left(N_j^{neq}\right) \ , \tag{3.17}$$

$$\approx \sum_j \frac{\partial \Delta_i}{\partial N_j}\left(N_j - N_j^{eq}\right) \ , \tag{3.18}$$

$$\approx \sum_j \Delta_{ij}\left(N_j - N_j^{eq}\right) \ . \tag{3.19}$$

The *scattering* matrix Δ_{ij} is defined by the transition probabilities $A\left(s \rightarrow s'\right)$, and is given by [17],

$$\Delta_{ij} = -\frac{1}{2}\sum_{s,s'}\left(s_i - s_i'\right) A\left(s \rightarrow s'\right)\left(\frac{\rho}{b}\right)^{p-1}(1-d)^{b-p-1}\left(s_j - s_j'\right) \ , \tag{3.20}$$

where $p = \sum_i s_i$, and b is the number of lattice link vectors. Equation (3.20) is a reduced expression when compared to (3.5).

The complete evolution equation becomes,

$$N_i(\mathbf{r} + \mathbf{c}_i, t+1) = N_i(\mathbf{r}, t) + \sum_j \Delta_{ij} \left(N_j - N_j^{eq} \right) \ . \tag{3.21}$$

The scheme encapsulated in (3.21) allowed more practical 3D simulations, as the complexity of the collision rules are reduced from 2^b to b^2. This model does, however, still suffer from the same constraints as the LGCA models since it is dependent upon the explicit underlying boolean microdynamics through $A\left(s \rightarrow s'\right)$ in (3.20), and the resulting macrodynamic equations are the same.

In 1989 Higuera *et al* [18] took a different point of view towards the collision operator. They let the form of the collision operator be dictated by the *target* macroscopic equations, *not by any underlying LGCA rules.* The effect of collision depended only upon the angle of the collision and could be tuned at will to ensure positive viscosity, and to remove the constraints imposed by LGCA microdynamics.

Consider a simple model with no rest particles, so that now $i = 1 \ldots 6$. An element of the collision matrix A_{ij}, denoted by a_θ, depends only on the angle, θ, between the link vectors $\mathbf{c}_i$ and $\mathbf{c}_j$. A_{ij} is rotationally invariant and for a FHP lattice θ can only take the possible values of 0°, 60°, 120° or 180°. Mass and momentum must of

course still be conserved hence the following constraints on A_{ij},

$$\sum_{i=1}^{6} A_{ij} = 0 , \tag{3.22}$$

$$\sum_{i=1}^{6} A_{ij} c_{\sigma i \alpha} = 0 , \tag{3.23}$$

which lead to the following relationships respectively,

$$a_0 + 2a_{60} + 2a_{120} + a_{180} = 0 , \tag{3.24}$$

$$a_0 + a_{60} - a_{120} - a_{180} = 0 . \tag{3.25}$$

The non-zero eigenvalues of the resulting symmetric and cyclic matrix can be written in terms of just a_0 and a_{60} [18],

$$\lambda = 6\,(a_0 + a_{60}) , \tag{3.26}$$

$$\sigma = 6\,(a_0 + 2a_{60}) , \tag{3.27}$$

where (3.26) is twofold degenerate. The value of λ can be shown [18] to be related to the kinematic viscosity, ν, and its value chosen to ensure this quantity to be positive,

$$\nu = -\frac{1}{4}\left(\frac{1}{\lambda} + \frac{1}{2}\right) . \tag{3.28}$$

By lowering λ close to -2, ν can approach zero [20]. Also, σ is usually chosen to be -1 so that N_i^{neq} decays as quickly as possible to zero [20]. It should be noted that numerical instability can occur (especially as ν approaches close to zero), since departing from a scheme based on LGCA collisions removes the unconditional stability present in such models.

For this *enhanced collision* LB model, the full evolution equation is,

$$N_i(\mathbf{r} + \mathbf{c}_i, t+1) = N_i(\mathbf{r}, t) + \sum_j A_{ij} \left(N_j - N_j^{eq}\right) , \tag{3.29}$$

where the scattering matrix is pre-calculated and has a limited set of values according to the proceeding analysis. The lattice Boltzmann model of [18], as presented, suppresses the statistical fluctuations which are present in lattice gases, but Galilean invariance is not restored and the pressure still retains a velocity dependence which is unphysical. Although, by convenient choice of equilibrium distribution function, the $g(\rho)$ factor responsible for non-Galilean invariance can be eliminated [14].

Some of the remaining problems (velocity dependent pressure etc.) were addressed in LB models [19]. However, these efforts were largely over taken when attention turned to LBGK simulations.

3.4 Lattice Bhatnagar-Gross-Krook Models

The major difficulty in dealing with the Boltzmann equation, in either its continuum or discretised form, is the complicated structure of the collision term. Simpler models, known as *collision models*, have been proposed for the collision term. The Bhatnagar Gross and Krook (BGK) model, [21], makes the assumption that much of the detail contained within the collision term is *not* of significant influence during collision, and it is expected that a simplified collision term (which, nevertheless has the average properties of the full collision operator) can replace it [22]. In the BGK model the collision operator is replaced by a scalar relaxation parameter, ω, known as the collision frequency in kinetic theory, and simply assumes the average effect of collisions is proportional to the departure from equilibrium. Importantly there is

now freedom to choose an equilibrium distribution, N_i^{eq}, which leads to the exact Navier-Stokes equations.

The evolution equation now becomes,

$$N_i(\mathbf{r}+\mathbf{c}_i, t+1) = N_i(\mathbf{r}, t) + \omega(N_i^{eq} - N_i) \ . \tag{3.30}$$

The BGK collision model was incorporated into LB models, known as LBGK models, independently, by Qian *et al* [3] and Chen *et al* [19], and was shown to lead to correct hydrodynamic behaviour. The correct continuity equation and second order accurate Navier-Stokes equations are recovered as follows,

$$\partial_t \rho + \partial_\beta (\rho u_\beta) = 0 \ , \tag{3.31}$$

$$\partial_t (\rho u_\alpha) + \partial_\beta (\rho u_\alpha u_\beta) = -\partial_\alpha \left(c_s^2 \rho\right) + \nu \partial_\beta \left[\partial_\beta (\rho u_\alpha) + \partial_\alpha (\rho u_\beta)\right] \ , \tag{3.32}$$

where speed of sound $c_s = \frac{1}{\sqrt{3}}$, and the 0kinematic viscosity $\nu = \frac{1}{6}\left(\frac{2}{\omega} - 1\right)$. This approach, using a simple relaxation parameter instead of more complex collision rules, is computationally much more efficient and provides flexibility in manipulating transport coefficients. Also the advective terms now satisfy the condition of Galilean invariance and the pressure is not velocity-dependent.

One advantage of LGCA is they are inherently stable, whereas models using a Boltzmann equation (including LBGK models), without their foundation in cellular automata microdynamics, are subject to numerical instabilities, (although relaxation schemes *are* known to have good stability properties). Analysis of the stability of LBGK models has been carried out by various authors. Sterling *et al* [23] found

that stability depends on the distribution of mass on a node between lattice links of different lengths, the relaxation parameter ω and mean velocity. Viscosity must always be positive, and, there is a maximum stable velocity for fixed values of the other parameters, the value of which increases with increase in ω until a certain value of ω when no increase is observed. This work was extended by Worthing *et al* [24] who report that $\omega = 1$ provides the optimal accuracy in time.

Since their inception in 1992 LBGK schemes have been the subject of much study. In the subsequent sections of this chapter we review applications and extensions to the standard LBGK scheme as introduced in [3, 19].

3.4.1 Boundary Conditions

Imposing a wall boundary condition was achieved in LGCA schemes using *bounce-back* lattice closure rules, where at a node denoted 'wall', during a wall collision the particles have their direction reversed and are sent back toward the node from which they came. Wolfram [11] stated that this would be sufficient to ensure no-slip conditions at solid surfaces, and the ease with which bounce-back can be implemented allows for the simulation of complex geometries such as flow through porous media.

This approach was found only to be first order accurate [25]. Whilst bounce-back conditions are 'good' in so far as they suppress Knudsen layers [25] the effective zero in macroscopic velocity is located slightly off node. He *et al* [26] analysed the velocity near the wall and confirmed this for Poiseuille flow. Attempts have

been made to improve adherence to the no-slip condition of the fluid medium as the LBGK scheme is second order accurate and a second order accurate boundary condition would obviously be preferable.

The problem at simulation lattice edge "wall" nodes is that some of the lattice links are outside of the system and as such have undefined behaviour. So schemes have been developed to obtain these unknown distributions to second order.

In 1993 Skordos [27] included velocity gradient terms in the equilibrium distribution at the 'wall' nodes from known values. This resulted in more accurate boundaries but the scheme was not as stable. A hydrodynamic no-slip condition on walls by applying a pressure constraint was proposed by Noble *et al* [28] with increased second order accuracy. Another second order accurate boundary scheme was proposed by Inamuro *et al* [29] who use a counter slip velocity to counteract the slip velocity which can occur using ordinary bounce-back. These schemes have been studied analytically by Zou *et al* [30].

3.5 Applications of the LBGK Scheme

3.5.1 Flow Around a Cylinder

The lattice Boltzmann approach using a linearised collision matrix was validated by Higuera *et al* [17]. They simulated flow around a cylinder at moderate Reynolds number, $Re \leq 80$. Time dependent behaviour was observed, and at $Re = 77.8$

periodic eddy shedding occured. The flow properties, for example lift and drag coefficients, agreed reasonably well with experiment. As these types of LB models are restricted to uniform lattices the circular geometry is only approximate, no-slip boundary conditions are applied on a 'jagged' edge not necessarily lying on the cylinder.

In 1997 He *et al* [40] returned to this geometry, and constructed a polar co-ordinate based lattice using an interpolation-supplemented LBGK model. The circular geometry of the cylinder was now accurately resolved and the accuracy of the LB simulation was within experimental accuracy.

3.5.2 Cavity Flow

Lattice Boltzmann models have been applied to many simple flow geometries. Hou *et al* [41] simulate two-dimensional cavity flow with good results using a LBGK scheme. In cavity flow there is a major central recirculation and secondary recirculations in the corners, the position and stream function of which vary with Re. Hou *et al* use a 256^2 lattice with Reynolds numbers in the range $10 \rightarrow 10,000$. On comparison with the results of other techniques already in the literature, the values of the streamlines and the positions of recirculations agree to within 1%. In [41] compressibility effects are also quantified for different maximum velocities and found to be small. Miller [42] has also applied the LBGK model to cavity flow and made comparisons for the velocity and pressure fields with analytical solutions with excellent agreement.

3.5.3 Backward Facing Step

Channel flow in which there is a sudden symmetric expansion has been studied by Luo *et al* [43] using a LBGK model. As the Reynolds number is increased the symmetry of the bifurcating flow breaks down. In [43] this was observed to occur at $Re = 46.19$ in comparison to the experimentally observed value of $Re = 47.3$.

Qian *et al* [44] have studied flow over an asymmetric expansion, or backward-facing step, using a standard LBGK scheme. The length of recirculation behind the step is measured as a function of step height and Reynolds number. The results compare well with experimental data and other numerical methods. The work of [44] helps to highlight some important issues surrounding LBGK models, the significance of which will become apparent later in this report.

3.6 Extensions of the Standard LBGK Scheme

3.6.1 Higher Order Schemes

The macroscopic equations are predicted using a Chapman-Enskog type analysis from which the basic result is that the Navier-Stokes equations are recovered as the governing equations of the lattice flow. Application of this method also reveals the presence of higher order terms [22] which depart from Navier-Stokes type behaviour. Qian *et al* [31] found these non-linear deviations from the Navier-Stokes equations are of the form $\partial_\beta \partial_\gamma u_\alpha u_\beta u_\gamma$. The effect of these "hidden" terms is that the behaviour

of the modelled fluid may differ significantly from that of the target real fluid when the flow enters the compressible regime. Chen *et al* [32] attempted to remove these deviations by inserting terms of higher-order in velocity in the equilibrium distribution. The complexity of the lattice-link geometry was also increased to ensure the isotropy of the sixth-rank velocity-moment tensor, whereas previous models only required isotropy of velocity-moment tensors up to fourth order. Another recent publication by Qian *et al* [33] has suggested that these non-linear deviations do not satisfy Galilean invariance and that this leads to a frame-velocity-dependent viscosity. To eliminate these errors Qian *et al* have included a cubic term in the equilibrium distribution along with a tunable parameter, which can be set to eliminate the undesired higher-order terms. However, the study reported in this thesis is only concerned with incompressible flows and hence the effect of such deviations are deliberately restricted.

3.6.2 Exactly-Incompressible Schemes

The study of incompressible flows can be somewhat restricted by the standard LBGK scheme. The incompressible form of the Navier-Stokes equations is recovered only if spatial gradients in lattice density may be neglected, and since density maps directly onto pressure this limits the range of pressure gradients which can be used accurately to force the flow. In consequence, the maximum achievable Reynolds number is restricted in flow geometries where there are significant non-uniform pressure drops. Frisch *et al* [2] in their work on LGCA first noted that if velocity was defined in

terms of a mass current then equations closer to the *incompressible* Navier-Stokes equations would result. This approach was applied to LBGK models independently by both Zou *et al* and Lin *et al* [30,34], who recover the correct time-independent incompressible equations; the correct form of the time derivatives is lost. These models are explained in more depth in section 4.2, and results of simulation of Poiseuille and cavity flows are reported to be in good agreement with analytical solutions, with greatly reduced compressibility errors.

3.6.3 Thermal Models

LBGK models which incorporate heat transfer have been developed by various research groups, and it is appropriate here briefly to summarise key contributors to the evolution of such models.

Pioneering work on LBGK thermohydrodynamics was presented by Alexander *et al* [35] who used a hexagonal lattice with 13 links and defined an internal energy, ε, through a second moment of N_i,

$$\rho\varepsilon = \sum_i \frac{N_i \left(c_{i\alpha} - u_\alpha\right)^2}{2} \,. \tag{3.33}$$

Third order velocity-dependent terms were included in the equilibrium distribution. This is sufficient to recover the energy equation in its standard form with viscous dissipation terms. When applied to the problem of simulating Couette flow, where there is a temperature gradient between two parallel plates, results are obtained which agree very well with theory for small temperature differences.

Chen *et al* [32] extended the above work of Alexander *et al* [35] by including higher-order terms in the equilibrium distribution in order to eliminate non-physical higher-order deviations, similar in form to those reported by Qian and Orzag [31] for isothermal LBGK models. This type of model is constrained to a fixed Prandtl number of unity [36] essentially because link energies and momentum densities are forced to relax at the same rate.

Chen *et al* [36] compared results of Couette flow simulations using the lower-order model of Alexander *et al* [35] and the higher-order models of Chen *et al* [32]. This work highlights the need to use the higher-order model for flows which are dominated by viscous heating effects. As heating due to friction increases, error in the lower order model rapidly increases although the scheme is much more efficient. In this work we will be interested only in flow geometries in which viscous heating can be considered negligible.

It was noted by McNamara *et al* [37] that the similarity between the Navier-Stokes and temperature equations could be exploited in order to develop LB models which treat temperature as an additional velocity component. Such models have improved stability properties in comparison with previous thermal models which are notoriously unstable, especially in three dimensions. This approach has the added benefit that it also allows for the development of models with variable Prandtl number. The correct form of the viscous dissipation terms in the temperature equation are not recovered. However in the majority of engineering flow geometries such terms are usually ignored. Different Prandtl numbers are achieved by allowing for two differ-

ent relaxation parameters, one to control viscosity as in the isothermal scheme and the other to control thermal diffusion, and the results of McNamara *et al* [37] show close agreement with more traditional CFD methods when applied to the problem of simulating Rayleigh-Bérnard convection.

Shan [38] also adopts the view taken by McNamara *et al* [37] and treats the energy as a passively-advected scalar quantity and employs the Boussinesq approximation. He exploits the multi-component flow model of Shan *et al* [39] and treats the temperature as an extra component. Again Shan [38] considers Rayleigh-Bénard convection, and results are seen to be in good agreement with other numerical methods.

3.6.4 Other Applications of LBGK Schemes

Lattice gases and lattice Boltzmann/BGK techniques have been applied to many different types of flow problems, which may not be directly relevant to this report but which are noteworthy. We will list some of them as it will serve to underline the usefulness of the techniques and show that the method is another numerical scheme worthy of careful consideration in its own right.

The modelling of multi-component flow is difficult because of the complex interface dynamics. These types of flows are important in many engineering applications, and LB techniques have been shown to be an alternative method of investigating such flows. The first immiscible lattice gas model was introduced by Rothman and Keller [45]. Gunstensen *et al* [20] then extended this work to be based upon a linearised LB

scheme, and subsequently LBGK-based immiscible models have emerged. Surface tension measurements have been shown to be in good agreement with Laplace's formula, and droplet breakup has been studied [46].

Boundary conditions are easily and efficiently implemented in LBGK models (see chapters 5, 6 and 7) which allows the scheme to be used for the simulation of porous media. Indeed the usefulness of the approach can be seen when considering multi-component flow through porous media [20], and can for example help understand the physics of oil reclamation and how to improve it. A LBGK model suitable for the simulation of granular flow has been reported by Tan *et al* [47], and a model for diffusion-driven reactions has been presented by Qian *et al* [48].

Chapter 4

Lattice BGK Theory

In this chapter we derive the standard LBGK scheme as introduced by Qian *et al* [3] and Chen *et al* [19], and obtain its governing macroscopic equations (the LBGK continuity equation and momentum equations) up to second order in velocity. Extensions to the standard scheme are then presented; firstly a scheme leading to the exact incompressible *steady-state* Navier-Stokes equations is described, followed by a novel scheme allowing the direct simulation of depth-averaged flow observables. All our analysis is based upon a two-speed square lattice with nearest and next-nearest neighbour links, commonly written in the literature as D2Q9, after the notation adopted by Qian *et al* [3].

Thermal LBGK models have been developed by various groups (see section 3.6.3), with varying degrees of success. We introduce in this chapter our own novel thermal scheme for Boussinesq-Oberbeck flow, in which energy is treated as a passively-

advected scalar quantity, allowing the LBGK simulation of forced convection flows in the Boussinesq-Oberbeck regime, with thermohydrodynamics which, we trust, are more robust than that of other thermal LBGK schemes.

4.1 Standard D2Q9 LBGK Scheme

4.1.1 Introduction

The evolution equation describing propagation and the collisions undergone by the momentum densities, $N_{\sigma i}$'s, is as discussed in section 3.4 for a LBGK model,

$$N_{\sigma i}(\mathbf{R}+\mathbf{c}_{\sigma i}, T+1) = N_{\sigma i}(\mathbf{R}, T) + \omega(N^{eq}_{\sigma i}(\mathbf{u}) - N_{\sigma i}(\mathbf{R}, T)) \ , \tag{4.1}$$

where the subscript σ denotes the speed of the link.

Position and time may be approximated by continuous variables, for sufficiently large lattices and long time intervals [2,11]. It is possible to define scaled variables like $t = \delta T$ where $\delta \ll 1$ and is the small lattice time step, t being physical time. The LBGK evolution equation in physical units then becomes,

$$N_{\sigma i}(\mathbf{r}+\delta\mathbf{c}_{\sigma i}, t+\delta) = N_{\sigma i}(\mathbf{r}, t) + \omega(N^{eq}_{\sigma i}(\mathbf{u}) - N_{\sigma i}(\mathbf{r}, t)) \ , \tag{4.2}$$

where $\mathbf{r}$ is a vector to any node, and $\mathbf{c}_{\sigma i}$ is a velocity vector associated with a lattice link, as defined in figure 4.1. In (4.2) collisions are mimicked in a relaxation process during which the particle distributions are allowed to relax to an equilibrium value with a time constant $\frac{1}{\omega}$. A Chapman-Enskog type expansion is applied in

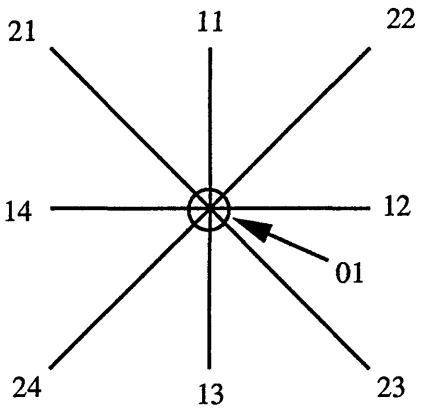

σi	$c_{\sigma ix}$	$c_{\sigma iy}$	c_σ^2
11	0	1	1
12	1	0	1
13	0	-1	1
14	-1	0	1
21	-1	1	2
22	1	1	2
23	1	-1	2
24	-1	-1	2
01	0	0	0

Figure 4.1: D2Q9 Lattice Unit Cell.

order to derive a set of partial differential equations which describe the behaviour of the macroscopic observable quantities in our LBGK fluid. The Chapman-Enskog expansion is used in kinetic theory for solving the continuum Boltzmann equation in the limit of small Knudsen number, K_n, which is defined as the ratio of the real particle mean-free path to a characteristic length scale of the flow. From its definition it is clear that K_n can vary from $0 \rightarrow \infty$, where $K_n \rightarrow 0$ corresponds to a fairly dense system and $K_n \rightarrow \infty$ implies a (gas dynamic) flow where there is negligible interaction between molecules.

Lattice densities effectively propagate a distance of $\delta \mathbf{c}_i$ between collision steps. Moreover, the computational lattice assembled from vectors $\mathbf{c}_i$ can characterise a simulation's macroscopic length scale. Thus, under these assumptions the lattice K_n can be defined as $|\delta \mathbf{c}_i| \,/\, |\mathbf{c}_i| \sim \delta$.

The Chapman-Enskog method is a multiscale technique, and we expect different physics to manifest on differing length and time scales in the lattice. On the shortest scale (δ^0) we expect to observe relaxation to *local* equilibrium. On longer length-

scales (δ^n) one expects, for example, viscous transport effects to manifest themselves.

For isothermal flows the macroscopically observable quantities, density and momentum, are defined respectively as,

$$\rho = \sum_{\sigma,i} N_{\sigma i} \ , \tag{4.3}$$

$$\rho \mathbf{u} = \sum_{\sigma,i} N_{\sigma i} \mathbf{c}_{\sigma i} \ . \tag{4.4}$$

A local equilibrium should only depend upon the macroscopic observables ρ and $\mathbf{u}$. For hydrodynamic behaviour, and under the assumption that density and velocity slowly vary with both time and position, a sufficiently general form for the equilibrium distribution will be [3],

$$N^{eq}_{\sigma i}(\mathbf{u}) = A_\sigma + B_\sigma(\mathbf{u}.\mathbf{c}_{\sigma i}) + C_\sigma(\mathbf{u}.\mathbf{c}_{\sigma i})^2 + D_\sigma u^2 \ , \tag{4.5}$$

where A_σ, B_σ, C_σ and D_σ are lattice-dependent variables yet to be defined. Essentially (4.5) is the simplest form capable of recovering the desired macrodynamics.

A Taylor expansion is now performed on the evolution equation (4.2) up to second order, which after some algebra, yields

$$\delta \left[\frac{\partial}{\partial t} + (c_{\sigma i\alpha}\partial_\alpha)\right] N_{\sigma i} + \frac{\delta^2}{2}\left[\frac{\partial}{\partial t} + (c_{\sigma i\alpha}\partial_\alpha)\right]^2 N_{\sigma i} = \omega(N^{eq}_{\sigma i} - N_{\sigma i}) \ . \tag{4.6}$$

The value of $N_{\sigma i}$ will be near its equilibrium value of $N^{eq}_{\sigma i}$, so $N_{\sigma i}$ may be expanded in powers of δ following the Chapman-Enskog type procedure,

$$N_{\sigma i} = N^{eq}_{\sigma i} + \delta N^{(1)}_{\sigma i} + \delta^2 N^{(2)}_{\sigma i} + \dots \ . \tag{4.7}$$

Macroscopic observables are determined by moments of the equilibrium distribution,

$$\sum_{\sigma,i} N_{\sigma i}^{eq} = \rho \,, \tag{4.8}$$

and,

$$\sum_{\sigma,i} N_{\sigma i}^{eq} c_{\sigma i\alpha} = \rho u_\alpha \,, \tag{4.9}$$

which requires that non-equilibrium densities, $N_{\sigma i}^{n}$ $(n \geq 1)$, do not contribute to either the local density or momentum,

$$\sum_{\sigma,i} N_{\sigma i}^{(n)} = 0 \,, \tag{4.10}$$

$$\sum_{\sigma,i} N_{\sigma i}^{(n)} c_{\sigma i\alpha} = 0 \,, \tag{4.11}$$

where $n \geq 1$. The time derivatives are expanded in an Enskog fashion,

$$\frac{\partial}{\partial t} = \frac{\partial}{\partial t_0} + \delta \frac{\partial}{\partial t_1} + \dots \,, \tag{4.12}$$

so that from the Taylor-expanded evolution equation (4.6), we obtain at $O(\delta)$,

$$(\partial_{t_0} + c_{\sigma i\alpha}\partial_\alpha) N_{\sigma i}^{eq} = -\omega N_{\sigma i}^{(1)} \,, \tag{4.13}$$

and at $O(\delta^2)$,

$$\partial_{t_1} N_{\sigma i}^{eq} + \left(1 - \frac{\omega}{2}\right)(\partial_{t_0} + c_{\sigma i\alpha}\partial_\alpha) N_{\sigma i}^{(1)} = -\omega N_{\sigma i}^{(2)} \,. \tag{4.14}$$

Now, tensors (moments of lattice velocity vectors) of the form $\sum_i (c_{\sigma i\alpha} c_{\sigma i\beta} \dots)$ occur in the derivation of the governing macroscopic equations. These tensors must be isotropic so that any rotation of the coordinate frame is not communicated onto the

desired form of the macroscopic equations. Sufficient isotropy is guaranteed by the following definitions [49],

$$\sum_i c_{\sigma i\alpha} c_{\sigma i\beta} = 2c_\sigma^2 \delta_{\alpha\beta} , \qquad \sigma = 1, 2 , \tag{4.15}$$

$$\sum_i c_{\sigma i\alpha} c_{\sigma i\beta} c_{\sigma i\gamma} c_{\sigma i\delta} = \begin{cases} 2\delta_{\alpha\beta\gamma\delta} , & \sigma = 1 , \\ 4\Delta_{\alpha\beta\gamma\delta} - 8\delta_{\alpha\beta\gamma\delta} , & \sigma = 2 , \end{cases} \tag{4.16}$$

where $\Delta_{\alpha\beta\gamma\delta} = \delta_{\alpha\beta}\delta_{\gamma\delta} + \delta_{\alpha\gamma}\delta_{\beta\delta} + \delta_{\alpha\delta}\delta_{\beta\gamma}$.

4.1.2 Lattice Continuity Equation

On summing (4.13) over σ and i, then applying the relevant constraints we obtain the first order mass conservation equation,

$$\partial_{t_0}\rho + \partial_\alpha(\rho u_\alpha) = 0 . \tag{4.17}$$

Now consider the second order equation (4.14) and sum over σ and i,

$$\partial_{t_1}\rho = 0 . \tag{4.18}$$

The correct form of the continuity equation is recovered if we add (4.17) to $\delta\times$(4.18) and recombine the time derivatives using (4.12), to give, correct to $O(\delta^2)$,

$$\partial_t\rho + \partial_\alpha(\rho u_\alpha) = 0 . \tag{4.19}$$

4.1.3 Lattice Euler Equation

We obtain the lattice Euler equation, through a first moment of $N_{\sigma i}$, by first multiplying (4.13) by $c_{\sigma i\alpha}$ before summing over σ and i, yielding the following conservation

of momentum equation correct to $O(\delta)$,

$$\partial_{t_0}(\rho u_\alpha) + \partial_\alpha \Pi^{eq}_{\alpha\beta} = 0 \ , \tag{4.20}$$

where,

$$\Pi^{eq}_{\alpha\beta} = \sum_{\sigma,i} N^{eq}_{\sigma i} c_{\sigma i\alpha} c_{\sigma i\beta} \ ,$$

and is the LBGK *momentum flux tensor*, see section 2.3.

A form for $\Pi^{eq}_{\alpha\beta}$ can be found by substituting into its definition the general form for the equilibrium distribution (4.5) (for the full derivation see Appendix A),

$$\Pi^{eq}_{\alpha\beta} = c_s^2 \rho \delta_{\alpha\beta} + \rho u_\alpha u_\beta \ , \tag{4.21}$$

where c_s is the speed of sound. If (4.21) is substituted back into (4.20) the Euler equation is recovered to $O(\delta)$,

$$\partial_{t_0} \rho u_\alpha + \partial_\beta \rho u_\alpha u_\beta = -\partial_\alpha p \ , \tag{4.22}$$

where the pressure, p, is given by $p = c_s^2 \rho$.

4.1.4 Lattice Momentum Equation

In order to obtain the governing momentum equation with dissipation it is necessary to proceed to $O(\delta^2)$. Multiply (4.14) through by $c_{\sigma i\alpha}$ and perform the usual summation to yield, to $O(\delta^2)$,

$$\partial_{t_1}(\rho u_\alpha) + \partial_\beta \left(1 - \frac{\omega}{2}\right) \Pi^{(1)}_{\alpha\beta} = 0 \ , \tag{4.23}$$

where,

$$\Pi^{(1)}_{\alpha\beta} = \sum_{\sigma,\, i} N^{(1)}_{\sigma i} c_{\sigma i\alpha} c_{\sigma i\beta} \ .$$

$\Pi^{(1)}_{\alpha\beta}$ can be evaluated by substituting for $N^{(1)}_{\sigma i}$ its definition which is found by re-arranging equation (4.13), and in turn substituting the definition of the equilibrium distribution function for $N^{eq}_{\sigma i}$ (see Appendix A for a fuller account of this). The result is,

$$\begin{aligned}\Pi^{(1)}_{\alpha\beta} \;=\; -\frac{1}{w}\Big[&\left(\frac{1}{3}-c_s^2\right)\partial_\gamma(\rho u_\gamma)\delta_{\alpha\beta} + \frac{1}{3}\partial_\alpha(\rho u_\beta) + \frac{1}{3}\partial_\alpha(\rho u_\beta) \\ &- u_\alpha\partial_\beta(c_s^2\rho) - u_\beta\partial_\alpha(c_s^2\rho) - \partial_\gamma(\rho u_\alpha u_\beta u_\gamma)\Big] \ . \end{aligned} \tag{4.24}$$

Next, combine (4.22) with $\delta\times$(4.23) and substitute $\Pi^{(1)}_{\alpha\beta}$ from (4.24) to give the following momentum equation, correct to $O(\delta^2)$

$$\begin{aligned}\partial_t(\rho u_\alpha) + \partial_\beta(\rho u_\alpha u_\beta) \;=\; &-\partial_\alpha(c_s^2\rho) \\ &+\delta\left[\partial_\alpha\left\{\left(\frac{1}{w}-\frac{1}{2}\right)\left(\frac{1}{3}-c_s^2\right)\partial_\gamma(\rho u_\gamma)\right\}\right. \\ &+\partial_\beta\left(\frac{1}{w}-\frac{1}{2}\right)\left[\frac{1}{3}\left(\partial_\alpha\rho u_\beta + \partial_\beta\rho u_\alpha\right)\right. \\ &\left.\left.+\left(\frac{1}{3}-c_s^2\right)\left(u_\alpha\partial_\beta\rho + u_\beta\partial_\alpha\rho\right) - \partial_\gamma(\rho u_\alpha u_\beta u_\gamma)\right]\right] + O(\delta^2) \ . \end{aligned} \tag{4.25}$$

The speed of sound is taken to be,

$$c_s^2 = \frac{1}{3} \ , \tag{4.26}$$

which allows (4.25) to be simplified to give the following,

$$\begin{aligned}\partial_t(\rho u_\alpha) + \partial_\beta(\rho u_\alpha u_\beta) \;=\; &-\frac{1}{3}\partial_\alpha(\rho) + \frac{\delta}{6}\left(\frac{2}{\omega}-1\right)\partial_\beta(\partial_\alpha\rho u_\beta + \partial_\beta\rho u_\alpha) \\ &-\delta\partial_\beta\left(\frac{1}{\omega}-\frac{1}{2}\right)\partial_\gamma(\rho u_\alpha u_\beta u_\gamma) + O(\delta^2) \ . \end{aligned} \tag{4.27}$$

We can now identify a lattice kinematic viscosity (in physical units) as,

$$\nu = \frac{\delta}{6}\left(\frac{2}{\omega} - 1\right) , \tag{4.28}$$

and identify the pressure (lattice fluid equation of state) as,

$$p = \frac{\rho}{3} . \tag{4.29}$$

Ignoring the third term on the right-hand side of (4.27), which is the leading non-linear error term [31], and writing in lattice units so that δ's do not appear, we have the following governing macroscopic momentum equation,

$$\partial_t(\rho u_\alpha) + \partial_\beta(\rho u_\alpha u_\beta) = -\partial_\alpha p + \nu\partial_\beta(\partial_\alpha \rho u_\beta + \partial_\beta \rho u_\alpha) , \tag{4.30}$$

which is obviously of similar form to the Navier-Stokes equations as defined in chapter 2 (see equations (2.24) and (2.26)).

LBGK schemes can be derived for other lattice geometries using the preceeding analysis. For example, the FHP 7-speed model's triangular (hexagonal) lattice. Figure 4.2 contains the coefficients that should be used in the equilibrium distribution function (4.5) when using a D2Q9 model; Appendix A contains a full account of the derivation. If another suitable geometry is to be used the same governing macroscopic equations would result, the only difference being the values of the equilibrium distribution coefficients, see for example [3].

	$\sigma = 0$	$\sigma = 1$	$\sigma = 2$
A_σ	$\frac{4}{9}\rho$	$\frac{1}{9}\rho$	$\frac{1}{36}\rho$
B_σ	0	$\frac{1}{3}\rho$	$\frac{1}{12}\rho$
C_σ	0	$\frac{1}{2}\rho$	$\frac{1}{8}\rho$
D_σ	$-\frac{2}{3}\rho$	$-\frac{1}{6}\rho$	$-\frac{1}{24}\rho$

Figure 4.2: D2Q9 equilibrium distribution coefficients.

4.1.5 Mapping onto Viscous, Incompressible Hydrodynamics

In order to develop a correspondence between the LBGK scheme and viscous incompressible hydrodynamics it is necessary to establish a mapping of the governing equations, (4.19) and (4.30), onto the continuity and incompressible Navier-Stokes equations (see chapter 2), which are, we recall

$$\partial_\alpha v_\alpha = 0 \,, \tag{4.31}$$

$$\frac{\partial v_\alpha}{\partial t} + v_\beta \partial_\beta v_\alpha = -\partial_\alpha \left(\frac{p}{d}\right) + \nu \partial_\beta \partial_\beta v_\alpha \,. \tag{4.32}$$

Neglecting variation of ρ in all but the pressure term, (4.30) is seen to be isomorphic with the *incompressible* Navier-Stokes equation (4.32). This process now identifies the following mappings,

$$p \;\rightarrow\; \frac{1}{3}\rho \,, \tag{4.33}$$

$$\underline{v} \;\rightarrow\; \underline{u} \,, \tag{4.34}$$

$$\nu \;\rightarrow\; \frac{1}{6}\left(\frac{2}{\omega} - 1\right) \,. \tag{4.35}$$

In hydrodynamics, liquid density d and pressure p are decoupled from one another by making the assumption $\frac{\partial d}{\partial p} = 0$, which is valid for a large speed of sound c_s

$\left(c_s = \sqrt{\frac{\partial p}{\partial d}}\right)$, and for small Mach number M $\left(M = \frac{V}{c_s}\right)$. Therefore, with a large value for c_s significant pressure changes can occur with negligible density changes (and indeed traditional CFD successfully computes pressure-driven athermal flows up to intermediate Re, in the incompressible limit). Mappings (4.33), (4.34) and (4.35) imply an equation of state $p = \rho/3$ for the lattice fluid, and a small speed of sound $c_s = \sqrt{\frac{\partial p}{\partial d}} = \frac{1}{\sqrt{3}}$ for the standard D2Q9 lattice fluid. As we shall see in subsequent chapters, the result of this is that the range of Re accessible to a LBGK scheme applied to internal pressure-driven flows, is constrained.

The lattice continuity equation gives divergence-free flow only if $\partial_\alpha \rho$ may be assumed small, which is easily seen from considering (4.19),

$$\partial_\alpha u_\alpha = -\frac{u_\alpha}{\rho}\partial_\alpha \rho \ . \tag{4.36}$$

The consequences of this are important for our anticipated applications : a requirement of negligible density gradient necessitates a restriction on any pressure gradient (essentially because c_s is $O(1)$ and that $p = \rho/3$), which allows only low velocity and low Re.

4.2 Exactly Incompressible LBGK Scheme

As noted at the end of the last section, for pressure-driven flows, what inhibits application of standard LBGK is that a pressure gradient must exist on the lattice by a gradient in ρ, the magnitude of which, when restricted to limit compressibility effects, constrains the Re obtainable with a given size of lattice. This section

describes an extension to the standard LBGK scheme which eliminates any need to restrict gradients in lattice density as it overcomes the constraint posed by the density/pressure relationship.

For lattice gas cellular automata it was stated by Frisch *et al* , in [2], that working in terms of a mass current to represent velocity would recover macroscopic equations which approximate more closely to the incompressible Navier-Stokes equations. This idea was applied to LBGK schemes by Zou *et al* [30] and independently Lin *et al* [34] who used revised macroscopic identifications for density and velocity respectively,

$$\rho = \sum_{\sigma,i} N_{\sigma i} \ , \tag{4.37}$$

$$\mathbf{u} = \sum_{\sigma,i} N_{\sigma i} \mathbf{c}_{\sigma i} \ . \tag{4.38}$$

The EILBGK scheme uses the same evolution equation as the standard scheme (4.2), however, to ensure that the correct form of the macroscopic governing equations are obtained, the equilibrium distribution is subtly modified:

$$N^{eq}_{\sigma i}(\mathbf{u}) = A_\sigma \rho + B_\sigma (\mathbf{u}.\mathbf{c}_{\sigma i}) + C_\sigma (\mathbf{u}.\mathbf{c}_{\sigma i})^2 + D_\sigma u^2 \ . \tag{4.39}$$

The derivation of the governing equations is suppressed here, as it is a straightforward extension to the procedure considered in section 4.1 for the standard scheme. These governing equations are shown to be [30,34],

$$\partial_\alpha u_\alpha = 0 \ , \tag{4.40}$$

$$\partial_\beta u_\alpha u_\beta = -\frac{1}{3}\partial_\alpha \rho + \delta \left(\frac{1}{\omega} - \frac{1}{2}\right) \partial_\beta \left(\frac{1}{3}\left(\partial_\beta u_\alpha + \partial_\alpha u_\beta\right)\right) \ . \tag{4.41}$$

We consider only the steady-state solutions of (4.40) and (4.41), since incorrect time derivatives emerge in (4.40), and written in lattice units (so that δ's do not explicitly appear), the equations become,

$$\partial_\alpha u_\alpha = 0 \,, \tag{4.42}$$

$$\partial_\beta u_\alpha u_\beta = -\frac{1}{3}\partial_\alpha \rho + \nu(\omega)\partial_\beta \partial_\beta u_\alpha \,, \tag{4.43}$$

where, as in the standard scheme, the kinematic viscosity ν of the lattice fluid is,

$$\nu = \frac{1}{6}\left(\frac{2}{\omega} - 1\right) \,. \tag{4.44}$$

Note that both the continuity equation and the advective term in the lattice momentum equation (4.43) now become *exactly incompressible* whilst the form for the diffusive term is preserved. Within the steady-state, it is now unnecessary to make any approximations to obtain viscous incompressible hydrodynamics, as is seen from the following revised mappings, (here d denotes the real fluid density)

$$\frac{p}{d} \;\rightarrow\; \rho \,, \tag{4.45}$$

$$\underline{v} \;\rightarrow\; \underline{u} \,, \tag{4.46}$$

and (4.35) again, the same form being recovered for kinematic viscosity. LBGK ρ maps directly onto hydrodynamic p/d without any association between ρ and d.

The equilibrium distribution coefficients for the D2Q9 geometry EILBGK scheme are as stated in figure 4.3.

	$\sigma = 0$	$\sigma = 1$	$\sigma = 2$
A_σ	$\frac{4}{9}$	$\frac{1}{9}$	$\frac{1}{36}$
B_σ	0	$\frac{1}{3}$	$\frac{1}{12}$
C_σ	0	$\frac{1}{2}$	$\frac{1}{8}$
D_σ	$-\frac{2}{3}$	$-\frac{1}{6}$	$-\frac{1}{24}$

Figure 4.3: D2Q9 equilibrium distribution coefficients for an EILBGK scheme.

4.3 Depth-Averaged Flow LBGK Scheme

In this section we modify a 2-dimensional EILBGK scheme in order to generate the required pseudo-body force terms in the macrodynamic momentum equation (4.43), governing the depth-averaged velocity. This enables the LBGK scheme to be yet further adapted and simulate depth-averaged flow (see chapter 2).

It is known that the addition of a constant term in the LBGK evolution equation has the effect of adding a constant body force term to the macroscopic momentum equation. (Zou *et al* [30] utilise this method to simulate Poiseuille flow, by considering a constant pressure gradient to be a constant body force.) So, we write a forcing-enhanced evolution equation as,

$$N_{\sigma i}(\mathbf{r} + \delta \mathbf{c}_{\sigma i}, t + \delta) = N_{\sigma i}(\mathbf{r}, t) + \omega(N^{eq}_{\sigma i}(\mathbf{u}) - N_{\sigma i}(\mathbf{r}, t)) + \delta f_{\sigma i} \ . \tag{4.47}$$

By choosing the form for $f_{\sigma i}$ to be,

$$f_{\sigma i} = \frac{k}{\rho} N^{eq}_{\sigma i}(0) c_{\sigma i \alpha} \sum_{\sigma, j} N_{\sigma j} c_{\sigma j \alpha} \ , \tag{4.48}$$

its moments should have the following properties,

$$\sum_{\forall\sigma,i} f_{\sigma i} = 0 , \tag{4.49}$$

$$\sum_{\forall\sigma,i} f_{\sigma i} c_{\sigma i\alpha} c_{\sigma i\beta} = 0 , \quad k_{\alpha\beta} u_\beta = \frac{1}{3} k u_\alpha , \tag{4.50}$$

$$\sum_{\forall\sigma,i} f_{\sigma i} c_{\sigma i\alpha} c_{\sigma i\beta} = 0 , \tag{4.51}$$

so that using the usual multiscale Chapman-Enskog analysis applied to LBGK models, we can easily show that the additional term in (4.47) will only affect $O(\delta)$ momentum equations. Considering the properties of the moments of $f_{\sigma i}$ it is easy to show that a modified steady-state Euler equation results, which, since the EILBGK scheme fails to recapture the correct time development, we state in time-independent form

$$\partial_\beta u_\beta u_\alpha = -\partial_\alpha \frac{\rho}{3} + \frac{k}{3} u_\alpha . \tag{4.52}$$

And with the $f_{\sigma i}$'s contributing no further to $O(\delta^2)$ equations, the derivation of the final macroscopic governing equations of our depth-averaged EILBGK scheme in the steady-state is straightforward. After section 4.1, the final macroscopic equations are,

$$\partial_\beta u_\beta = 0 , \tag{4.53}$$

$$u_\beta \partial_\beta u_\alpha = -\frac{1}{3}\partial_\alpha \rho + \nu(\omega)\partial_\beta \partial_\beta u_\alpha + \frac{k}{3} u_\alpha , \tag{4.54}$$

in which $\nu(\omega)$ is again given by (4.44). Our depth-averaged EILBGK scheme preserves the exact form of the incompressible continuity equation, and its momentum equation is seen to be isomorphic with the depth-averaged flow governing momentum

equation (2.64) with the following mapping,

$$\frac{k}{3} \rightarrow \frac{12\nu}{L_z^2} \,. \tag{4.55}$$

Therefore, the *depth* parameter k, introduced into (4.47) through (4.48), provides the mechanism by which the unmodelled depth of the duct can be controlled in simulation. Substituting the EILBGK's expression for ν we obtain, in lattice units,

$$L_z = 6\sqrt{\frac{\nu(\omega)}{k}}, \quad \nu(\omega) = \frac{1}{6}\left(\frac{2}{\omega} - 1\right) \,. \tag{4.56}$$

4.4 Thermal LBGK Model

As we have seen with the standard and Exactly-Incompressible LBGK schemes for momentum, the densities are relaxed towards an equilibrium value during the collision step. We introduce the notion that thermalisation of the internal energy associated with a particular momentum density $N_{\sigma i}$ occurs on a separate time scale, characterised by ω'. Because the parent momentum densities, $N_{\sigma i}$'s, and their associated internal energy variable, the $\varepsilon_{\sigma i}$'s, may relax on different time scales, one may write for the internal energies a separate evolution equation similar in form to that which describes the behaviour of the momentum densities,

$$\varepsilon_{\sigma i}(\mathbf{r} + \mathbf{c}_i, t+1) = \varepsilon_{\sigma i}(\mathbf{r}, t) - \omega'((\varepsilon_{\sigma i}(\mathbf{r}, t) - \varepsilon_{\sigma i}^{eq}(\mathbf{r}, t)) \,, \tag{4.57}$$

the local internal energy equilibrium distribution, $\varepsilon_{\sigma i}^{eq}$, being given we propose by,

$$\varepsilon_{\sigma i}^{eq} \equiv \frac{\varepsilon\emptyset}{\rho} N_{\sigma i}^{\dagger} \,, \tag{4.58}$$

where $N^{\dagger}_{\sigma i}$ is the post-collision value of momentum density.

The macroscopic observable quantity $\varepsilon\emptyset$, which will eventually map onto temperature, is the total node internal energy defined as,

$$\varepsilon\emptyset = \sum_{\sigma,i} \varepsilon_{\sigma i} \ . \tag{4.59}$$

In order to determine the macroscopic heat equation obeyed by the internal energies it is again appropriate to use a Chapman-Enskog type expansion,

$$\varepsilon_{\sigma i} = \varepsilon^{eq}_{\sigma i} + \delta\varepsilon^{(1)}_{\sigma i} + \delta^2\varepsilon^{(2)}_{\sigma i} + \ldots \ . \tag{4.60}$$

To ensure that energy is always locally conserved, the $\varepsilon^{(n)}_{\sigma i}$'s for $n \geq 1$, should not be allowed to contribute to the internal energy, so we fix their neutrality in this respect by requiring,

$$\sum_{\sigma,i} \varepsilon^{(n)}_{\sigma i} = 0 \ , \qquad n \geq 1 \ . \tag{4.61}$$

Therefore,

$$\begin{aligned} \sum_{\sigma,i} \varepsilon^{eq}_{\sigma i} &= \sum_{\sigma,i} \varepsilon_{\sigma i} \ , \\ &= \frac{\varepsilon\emptyset}{\rho} \sum_{\sigma,i} N_{\sigma i} \ , \\ &= \varepsilon\emptyset \ . \end{aligned} \tag{4.62}$$

To avoid spurious thermal modes we avoid defining any vector modes associated with the $\varepsilon_{\sigma i}$'s, and simply write,

$$\begin{aligned} \sum_{\sigma,i} \varepsilon^{eq}_{\sigma i} c_{\sigma i\alpha} &= \frac{\varepsilon\emptyset}{\rho} \sum_{\sigma,i} N_{\sigma i} c_{\sigma i\alpha} \ , \\ &= \varepsilon\emptyset \, v_{\alpha} \ , \end{aligned} \tag{4.63}$$

and, as a consequence of this lack of a vector thermal mode we do *not* fix the neutrality of the first moment of the $\varepsilon_{\sigma i}^{(n)}$, for $n \geq 1$ note,

$$\sum_{\sigma,i} \varepsilon_{\sigma i}^{(n)} c_{\sigma i \alpha} \neq 0 \ , \qquad n \geq 1 \ . \tag{4.64}$$

Now following the usual lattice evolution, evolution equation (4.57) is Taylor expanded to second order,

$$\delta \left[\frac{\partial}{\partial t} + (c_{\sigma i \alpha} \partial_\alpha) \right] \varepsilon_{\sigma i} + \frac{\delta^2}{2} \left[\frac{\partial}{\partial t} + (c_{\sigma i \alpha} \partial_\alpha) \right]^2 \varepsilon_{\sigma i} = \omega' (\varepsilon_{\sigma i}^{eq} - \varepsilon_{\sigma i}) \ . \tag{4.65}$$

Note that δ is the same explicit time-step as used in the evolution of momentum densities $N_{\sigma i}$'s.

The time derivatives are treated in exactly the same manner, and thus expanded as in (4.12). If expansions (4.60) and (4.12) are substituted in (4.65) and terms to $O(\delta)$ collected, the following $O(\delta)$ equation results,

$$(\partial_{t_0} + c_{\sigma i \alpha} \partial_\alpha) \, \varepsilon_{\sigma i}^{eq} = -\omega \varepsilon_{\sigma i}^{(1)} \ . \tag{4.66}$$

Summing (4.66) over σ and i, and applying the relevant constraints, we are left with the following first order ($O(\delta)$) energy equation,

$$\partial_{t_0} \varepsilon \phi + \partial_\alpha \varepsilon \phi u_\alpha = 0 \ . \tag{4.67}$$

On extracting $O(\delta^2)$ terms from (4.65) we obtain,

$$\partial_{t_1} \varepsilon_{\sigma i}^{eq} + \left(1 - \frac{\omega'}{2} \right) (\partial_{t_0} + c_{\sigma i \alpha} \partial_\alpha) \varepsilon_{\sigma i}^{(1)} = -\omega' \varepsilon_{\sigma i}^{(2)} \ . \tag{4.68}$$

We now sum (4.68) over i and σ to yield,

$$\partial_{t_1} \varepsilon \phi + \left(1 - \frac{\omega'}{2} \right) \partial_\alpha \left(\sum_{i,\sigma} \varepsilon_{\sigma i}^{(1)} c_{\sigma i \alpha} \right) = 0 \ . \tag{4.69}$$

To obtain a form for $\partial_\alpha \left(\sum_{i,\sigma} \varepsilon_{\sigma i}^{(1)} c_{\sigma i \alpha} \right)$ in (4.69) we multiply (4.66) by $c_{\sigma i \alpha}$ and ∂_α before performing the usual summation (see appendix B for suppressed algebra),

$$\partial_\alpha \left(\sum_{i,\sigma} \varepsilon_{\sigma i}^{(1)} c_{\sigma i \alpha} \right) = -\frac{1}{\omega'} \partial_{t_0} \partial_\alpha \left(\varepsilon \emptyset u_\alpha \right) - \frac{1}{\omega'} \left(\frac{1}{c_s^2} \partial_\alpha^2 \varepsilon \emptyset + \partial_\alpha \partial_\beta \varepsilon \emptyset u_\alpha u_\beta \right) . \tag{4.70}$$

The resulting second order equation becomes,

$$\begin{aligned} \partial_{t_1} \varepsilon \emptyset + \left(\frac{1}{2} - \frac{1}{\omega'} \right) \partial_{t_0} \partial_\alpha \left(\varepsilon \emptyset u_\alpha \right) + \left(\frac{1}{2} - \frac{1}{\omega'} \right) \frac{1}{c_s^2} \partial_\alpha^2 \varepsilon \emptyset \\ + \left(\frac{1}{2} - \frac{1}{\omega'} \right) \partial_\alpha \partial_\beta \left(\varepsilon \emptyset u_\alpha u_\beta \right) = 0 . \end{aligned} \tag{4.71}$$

To obtain our models governing heat equation we add the $O(\delta)$ equation (4.67) to $\delta \times O(\delta^2)$ equation (4.71), recombine the time derivatives (where appropriate), and apply the product rule to the spatial derivative in the $O(\delta)$ equation (4.67) in order to yield,

$$\begin{aligned} \partial_t \varepsilon \emptyset + u_\alpha \partial_\alpha \varepsilon \emptyset = \delta \chi \partial_\alpha^2 \varepsilon \emptyset \\ - \varepsilon \emptyset \partial_\alpha u_\alpha \\ - \delta c_s^2 \chi \partial_{t0} \partial_\alpha \varepsilon \emptyset u_\alpha \\ - \delta c_s^2 \chi \partial_\alpha \partial_\beta \varepsilon \emptyset u_\alpha u_\beta . \end{aligned} \tag{4.72}$$

The isomorphism between (4.72) and the heat equation for Boussinesq-Oberbeck flow (2.45) is obvious and we can immediately identify our our model's *thermal diffusivity*, χ, given by,

$$\chi = \frac{\delta}{c_s^2} \left(\frac{1}{\omega'} - \frac{1}{2} \right) . \tag{4.73}$$

Note, when written in terms of lattice units δ does not appear in the previous equation.

As we have already seen, for incompressible flow the LBGK velocity field becomes divergence-free if gradients in lattice density are negligible. It is easily shown with some simple algebra that the last three terms in (4.72) reduce to zero if the assumption of incompressible flow is invoked, which leaves the following LBGK thermal governing equation,

$$\partial_t \varepsilon\phi + u_\alpha \partial_\alpha \varepsilon\phi = \chi \partial_\alpha^2 \varepsilon\phi \ ,$$
$$\chi = \frac{1}{c_s^2}\left(\frac{1}{\omega'} - \frac{1}{2}\right) \ . \tag{4.74}$$

Equations (4.74) clearly have, for divergence-free flow, a marked resemblance to the Boussinesq-Oberbeck equations.

4.4.1 Mapping onto Boussinesq Equations

From section 2.7, equation (2.45) we know that under the Boussinesq approximations the macrodynamic energy equation for an incompressible flow is,

$$\partial_t T + \mathbf{v}.\nabla T = \chi \nabla^2 T \ . \tag{4.75}$$

We now make the following interpretation of our energy variable $\varepsilon\phi$,

$$\varepsilon\phi \rightarrow \rho c_p T \ , \tag{4.76}$$

which will in consequence have physical units of energy. The reason for this interpretation will become clear as we consider appropriate thermal boundary conditions.

On making this replacement, our thermal LBGK governing equation (4.74) is seen to be isomorphic with (4.75) multiplied through by ρc_p (an assumed constant).

We now consider the definition of the lattice Nusselt number. From (2.47), we know,

$$Nu \equiv \frac{hl}{k} = \frac{q}{(T_w - T_b)} \times \frac{l}{k} \,, \tag{4.77}$$

remembering that $\chi = k/\rho c_p$. We now cast (4.77) in terms of our internal energy variable $\varepsilon\phi$, to obtain a lattice Nusselt number,

$$\begin{aligned} Nu &= \frac{q}{(T_w - T_b)} \times \frac{l}{\rho c_p \chi} \,, \\ &= \frac{q}{(\varepsilon\phi_w - \varepsilon\phi_b)} \times \frac{l}{\chi} \,, \\ &= \frac{hl}{\chi} \,, \end{aligned} \tag{4.78}$$

with the lattice heat transfer coefficient defined through,

$$h^* \equiv \frac{q}{(\varepsilon\phi_w - \varepsilon\phi_b)} \,. \tag{4.79}$$

The last equation may be re-interpreted immediately to obtain an identity for the lattice Nusselt number,

$$Nu^* \equiv \frac{h^* l^*}{\chi(\omega)} \,. \tag{4.80}$$

Note that, to recover Boussinesq-type governing equations from the dynamics of our second distribution, $\varepsilon_{\sigma i}^{eq}$, the parent flow must be divergence-free; that is contain only negligible density gradients, so that if used alongside the standard LBGK scheme to evolve the momentum distribution (the $N_{\sigma i}$'s) the forcing applied to induce flow should be carefully chosen in order to avoid introducing density gradients (see discussion section 5.5).

Chapter 5

Internal Pressure Driven Flow Simulations

5.1 Introduction

As discussed in section 4.1.5, the standard LBGK scheme recovers the incompressible Navier-Stokes equations only if spatial gradients in lattice density, and therefore gradients in pressure, may be neglected. Strictly, this prevents the correct application of standard LBGK to systems which contain significant *non-uniform* pressure gradients. The relationship between lattice density and fluid pressure couples the pressure and velocity fields so that if density/pressure gradients are not small, significant compressibility errors would occur as the velocity field ceases to become divergence-free, and as a consequence of this the maximum attainable Re is re-

stricted.

Spatially-uniform body forces can and have been used to model pressure gradients, but this device is, strictly, only valid for mimicking a uniform pressure gradient and does not allow the representation of non-uniform variation of pressure throughout the system.

The standard LBGK scheme has been reported to achieve, with good accuracy, Reynolds numbers of around a few thousand [41,42] in systems with fairly uniform pressure (where the primary forcing agency is velocity at flow boundaries), but there have been few applications to pressure-driven flows. Hou *et al* [41] calculate the small compressibility effects in a LBGK simulation of two-dimensional lid-driven cavity flow. For our application to pressure driven flow, so limiting are compressibility effects that we are obliged to use an EILBGK scheme.

By careful application of an EILBGK scheme, we show in this chapter how it is possible to overcome the constraint posed by the lattice density/fluid pressure relationship and obtain information about both non-uniform velocity fields *and* pressure fields. In this chapter we also consider no-slip wall behaviour and apply LBGK boundary conditions in closer accord with engineering and CFD practice. Without compressibility error, we proceed to simulate flow over a backward-facing step, up to much higher Re than that at which standard LBGK begins to exhibit prohibitive compressibility error. We consider our results in the context of standard CFD, experiment and some theoretical results.

Throughout this chapter we shall consider results (from experiment, LBGK and CFD etc.) for laminar flow and make no attempt to recover any effect of turbulence.

5.2 Simulation

As shown in section 4.2 the EILBGK scheme fails to capture the correct form of the time derivatives in the lattice Navier-Stokes equation, nevertheless we iterate the evolution equation over the whole lattice to a steady-state. At long-times the pde solved by the EILBGK scheme is correct and indeed many 'null-transient' CFD calculations in schemes which also miss 'physical' time-dependence make the assumption that, if calculable, *a* steady-state is *the* steady state, when using fixed forcing functions and boundary conditions. The detailed effect of the time-dependence of the EILBGK dynamics is not likely to have a significant effect and is a problem with several significant technical difficulties [52] which lies beyond our present scope. For the results we report in this chapter, convergence was checked by testing the the solution's sensitivity to its initial conditions. Numerical instability was observed when viscosity, ν, became too small, but a full comparison of stability in either scheme is an undertaking somewhat beyond the scope of this work.

We also describe the means by which the EILBGK scheme lends itself to the implementation of boundary conditions which allow measurement of both pressure drops *and* flow fields after appropriate calibration using the friction factor.

5.2.1 Boundary Conditions

Lattice-Boltzmann methods do not explicitly set domain boundary velocities. Instead *closure rules* are applied on the simulation lattice edge which act (one hopes) to impose the desired conditions on the lattice fluid.

In the next section, 5.3, we are particularly concerned with zero velocity ("no-slip") closure conditions, and we shall rely especially upon the work of d'Humiéres *et al* [52]. In this section we describe our technique of *equilibrium forcing*, which exploits the decoupled lattice density to *close* boundary-node velocities, $\mathbf{u}$, using the equilibrium densities $N_{\sigma i}^{eq}(\rho, \mathbf{u})$, without undermining momentum conservation. Certain boundary pressures are free to develop to values determined by the equations effectively under solution and the explicitly set lattice closure rules. Such *open* boundaries are easily implemented in the EILBGK scheme where lattice site density influences pressure and not lattice momentum.

We consider as an appropriate test bench problem, flow past a backward-facing step of height H in a channel of outlet height W and length L_0, see figure 5.1. At the inlet parabolic flow is forced as described above, by over-writing with equilibrium densities $N_{\sigma i}^{eq}(\rho, \mathbf{u})$ calculated from a chosen inlet pressure, $\rho = 1.8$, and the chosen inlet velocity profile,

$$u_x = \frac{-4u_0}{W^2 - 2HW + H^2}(y - W)(y - H) \,, \tag{5.1}$$

where u_0 is the maximum velocity. At the outlet (defined at $x = L_0$), a velocity profile consistent with physical mass conservation is applied, inlet and outlet profile

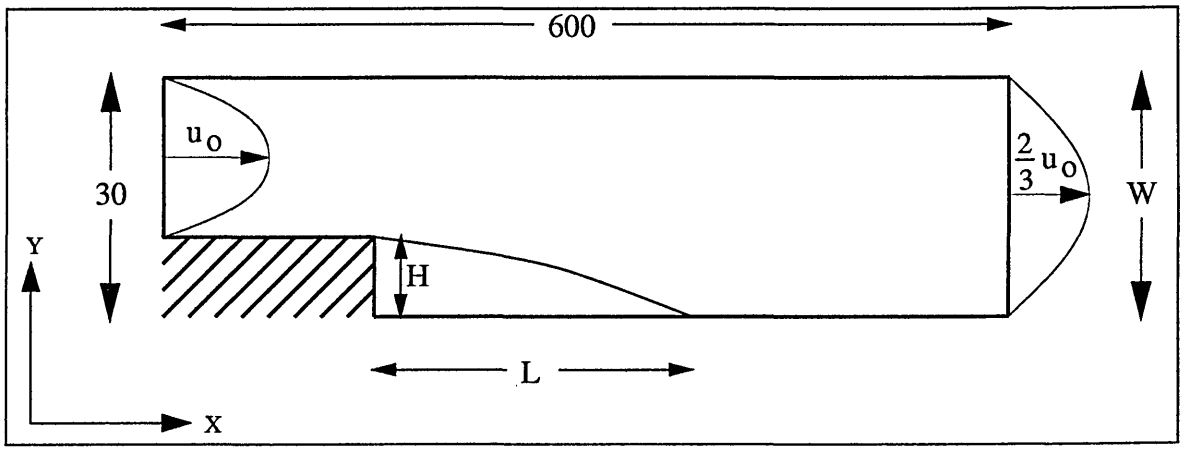

Figure 5.1: The backward-facing step geometry simulated. The step height H is one third of the channel width W. The lattice used to resolve the geometry was 600 × 30 sites.

maxima being related through $u_0 = \frac{3}{2}u_0'$,

$$u_x = \frac{-4u_0'}{W^2} y(y - W) \ . \tag{5.2}$$

Pressure at the outlet was allowed to freely develop, the value of ρ used in $N_{\sigma i}^{eq}(\rho, \mathbf{u})$ was the average value across the y-profile at $x = (L_0 - 1)$. (Note, experiments on this system would typically work in reverse, setting the inlet flux and outlet pressure.) It is also important to note that care must be exercised when extracting information about the pressure and velocity fields. This is due to the fact that forcing occurs via the $N_{\sigma i}^{eq}$'s and not the full $N_{\sigma i}$'s, so data must only be taken downstream of the forced inlet (and upstream of the outlet) where the velocity has become parabolic, based upon the $N_{\sigma i}$'s. For the results reported here a distance of W lattice sites from either end was found to be sufficient and this method of forcing using equilibrium densities, it was observed, drove our system towards a parabolic profile with good spatial efficiency compared with other methods of driving flow. A steady-state density/pressure develops to a measurable value determined by inlet

conditions and the other boundaries in the system and, after appropriate measures, (section 5.3) the non-uniform pressure field resulting from a particular set of inlet driving conditions was obtained.

With an open boundary condition, p decays along the simulation consistent with the expected reduction in hydrostatic pressure, and viewed from an EILBGK scheme, the simulation's total mass must be allowed to *equilibrate* to an asymptotic steady-state value, figure 5.2. Figure 5.4 shows a typical variation in p along a uniform

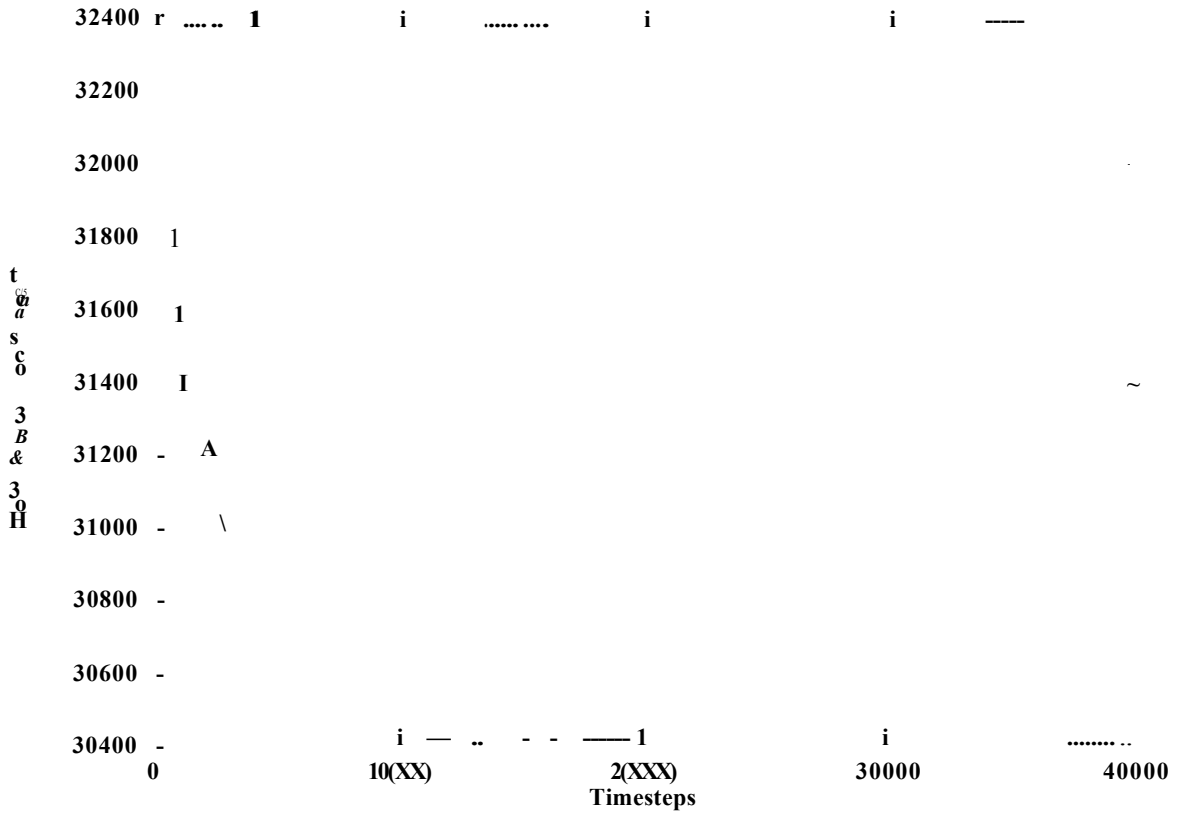

Figure 5.2: Total EILBGK mass as a function of timesteps for the geometry of figure 5.1.

channel of infinite aspect ratio, see figure 5.3, for the EILBGK and standard LBGK

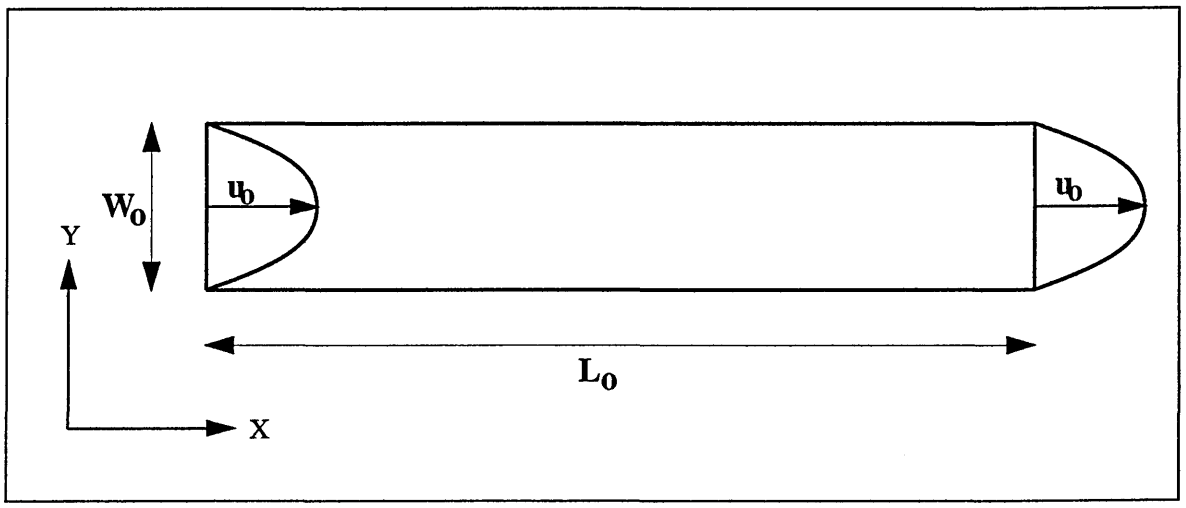

Figure 5.3: The infinite aspect ratio duct used to calibrate boundary conditions and pressure changes along the duct.

scheme at similar values of Re.

In figure 5.5, we see the associated variations, along the channel, of average velocity $\bar{u}$. For the EILBGK scheme $\bar{u}$ is seen to be constant, whereas, in the standard LBGK scheme the continuity equation couples density changes with changes in velocity leading to compressibility effects, even at low Reynolds number, making the acceptable limit on compressibility effects the limiting factor on the accessible Reynolds number in LBGK hydrodynamics applied using the standard LBGK scheme in the present problem.

5.3 Friction Factor

If we consider a straight duct, such as that shown in figure 5.3, along that duct there is a gradient in pressure caused by the friction of the fluid against the wall.

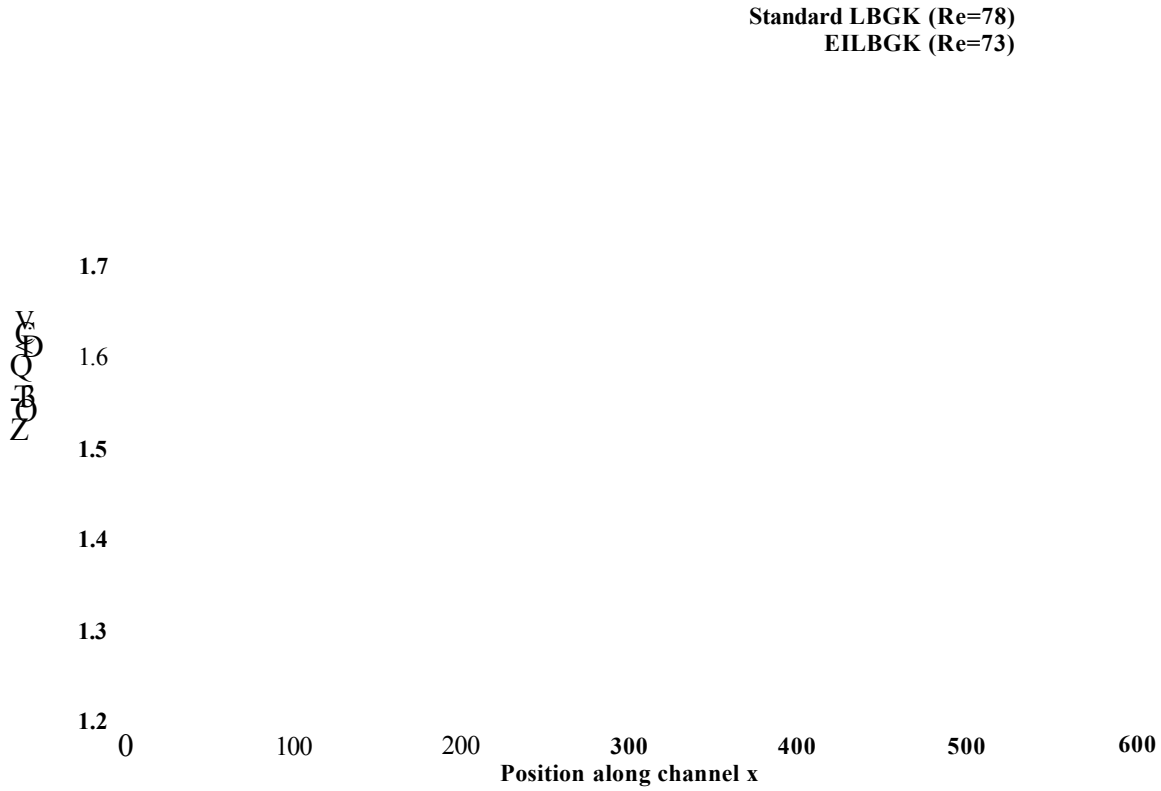

Figure 5.4: Lattice density p plotted as a function of distance, x, along an infinite aspect ratio duct, forced with an open boundary condition outlet. Green (blue) line represents p in the El (standard) LBGK scheme.

Prediction of this loss is a very important problem in fluid mechanics.

The pressure gradient, will be a constant and dependent upon Re. So,

$$£ = /<*>, \tag{5.3}$$

which we integrate to obtain,

$$Ap^* = Ax^* f\{Re) \ . \tag{5.4}$$

The variables are non-dimensionalised by taking a characteristic length scale to be the hydraulic diameter $2Wq$, so $x^* — x/2Wo$, and dimensionless pressure to be

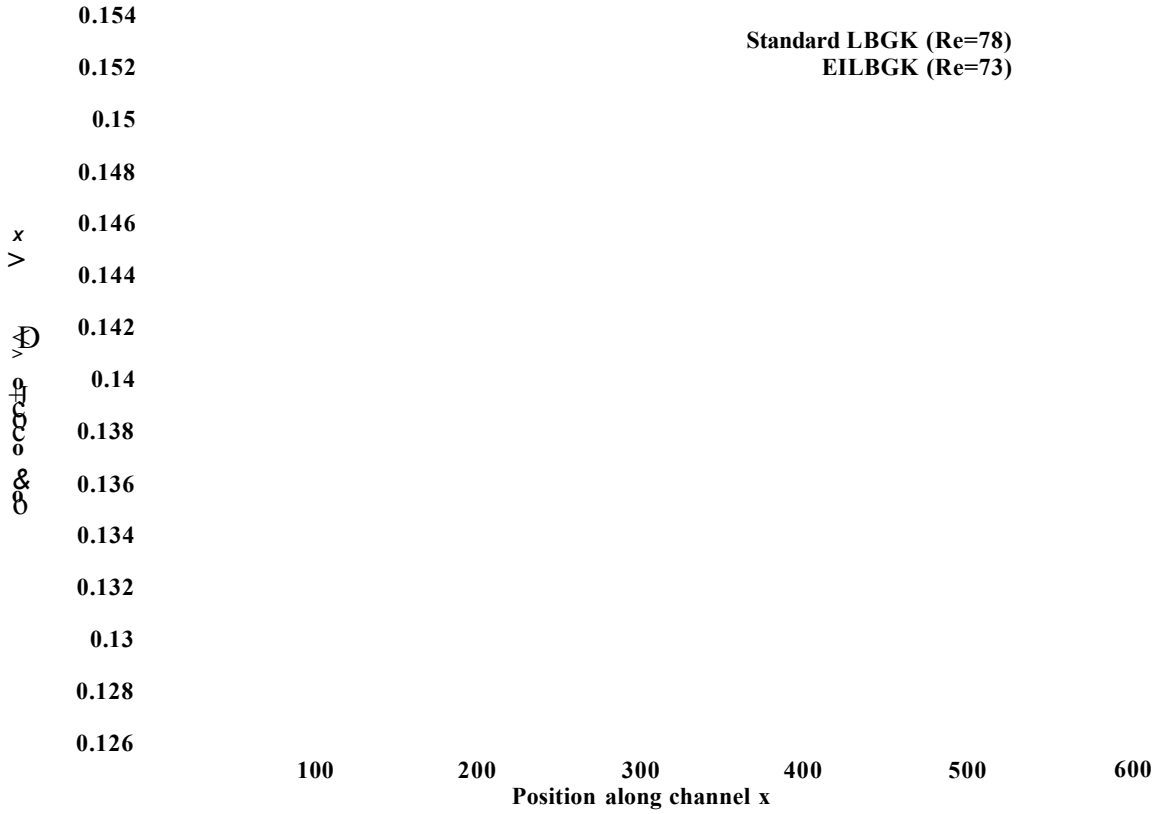

Figure 5.5: Average LBGK velocity «(»). Green (blue) line represents u in the El (standard) LBGK scheme.

$p^* = 2p/pu2$, where u is the average velocity across the duct width.

The pressure drop along a duct of length L_Q is,

$$\mathrm{A}P = \frac{f}{2W_Q} \frac{\rho}{2} f, \tag{5.5}$$

where / is a function known as the *friction factor*.

For the case of laminar flow in a duct, of geometry shown in figure 5.3, velocity is a function of y and has only an ^-component, and p is only a function of x.

Consequently the Navier-Stokes equations and appropriate boundary conditions are,

$$\frac{dp}{dx} = \eta \frac{d^2u}{dy^2}, \quad u = 0 \quad \text{at} \quad y = 0, W_0 . \tag{5.6}$$

The pressure gradient is constant along the channel, therefore (5.6) is integrated and evaluated using the above boundary conditions to give Poiseuille flow,

$$u = -\frac{1}{2\eta}\frac{dp}{dx}\left(W_0 y - y^2\right) . \tag{5.7}$$

The flux of fluid flowing per unit length (duct discharge) is,

$$q = \int_0^{W_0} u\, dy = -\frac{W_0^3}{12\eta}\frac{dp}{dx} , \tag{5.8}$$

and the average velocity is,

$$\bar{u} = \frac{q}{W_0} = -\frac{W_0^2}{12\eta}\frac{dp}{dx} . \tag{5.9}$$

The pressure gradient decreases in the direction of the flow, and can be written as,

$$\Delta p = \frac{12\eta L_0}{W_0^2}\bar{u} , \tag{5.10}$$

which can be re-expressed as,

$$\Delta p = \frac{96}{Re}\frac{L_0}{2W_0}\frac{\rho\bar{u}^2}{2} . \tag{5.11}$$

From a comparison of (5.11) and (5.5) it is readily apparent that for laminar flow in a duct the friction factor is,

$$f = \frac{96}{Re}. \tag{5.12}$$

The *LBGK* friction factor, f^*, provides a means by which we investigated a 'no-slip' closure rule designed to impose a zero-velocity no-slip boundary on the modelled

walls. Lattice friction factor f^* was measured by driving flow in an infinite aspect ratio straight duct using matched parabolic velocity profiles at the inlet and outlet, section 5.2.1. The lattice closure conditions should introduce friction at wall nodes if one hopes to generate no-slip conditions on velocity. The rule applied to define the sides of the duct and step ('wall sites') was a boundary-specific collision in which densities on links with a component perpendicular to the lattice line containing the boundary are *bounced-back* or specularly-reflected.

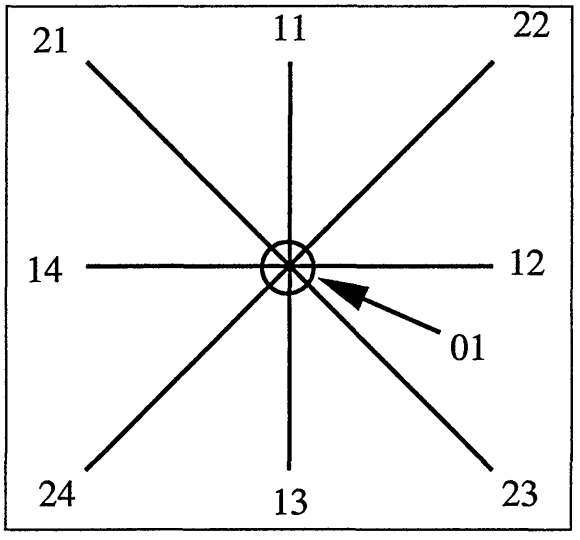

Figure 5.6: D2Q9 unit cell.

Consider a lattice boundary applied in the line $y = y^*$. For our lattice speed 1 links lie perpendicular or parallel to this line, see figure 5.6, and were accordingly reflected or left unadjusted. The densities on speed 2 links were coded partly to reflect specularly (deflect through $\frac{\pi}{2}$ radians) and partly to reverse (reflect through π radians) with probability $(1 - b)$ and b respectively. Thus our wall collision rule

is, at steady-state [50],

$$N_{21}(x, y^*) = bN_{23}(x, y^*) + (1-b)N_{24}(x, y^*) , \tag{5.13}$$

$$N_{22}(x, y^*) = bN_{24}(x, y^*) + (1-b)N_{23}(x, y^*) , \tag{5.14}$$

$$N_{11}(x, y^*) = N_{13}(x, y^*) . \tag{5.15}$$

In [25] it was shown that the above closure rules will not necessarily locate a zero of velocity boundary, or wall, in the line of lattice boundary nodes $y = y^*$. Rather the effective wall should be taken to lie off-lattice by a small distance, fixed by the bounce-back parameter b and the lattice size, which with L_0 and W_0 in lattice units, for a D2Q9 standard LBGK, an infinite aspect ratio duct may be shown to have a diameter D [25, 52],

$$D^2 = \left(W_0 + 6\nu\frac{(1-b)}{b}\right)^2 + 48\nu^2 - 1 + 4\nu\frac{(1-b)}{b} - 36\nu^2\frac{(1-b)^2}{b^2} . \tag{5.16}$$

Further, for fully-developed flow in a straight duct, theory shows $\Delta p/dL_0 = 2\nu V_0/D^2$ [52] and after some analysis to determine a lattice $\overline{v}$ [52] one obtains from (5.11) the *lattice* friction factor in terms of set simulation parameters [52]:

$$f^* = \frac{96}{Re}\left(1 + \frac{(72\nu^2 - 1)}{W_0^2} + 6\nu\frac{(1-b)}{b}\frac{(3W_0+1)}{W_0^2}\right)^{-1} . \tag{5.17}$$

Theoretically then, a finite fraction of *bounce-back*, b, introduces frictional stresses, a parallel rest layer very near to the lattice edge and determines the friction factor. Clearly, for small lattice viscosity ν and large duct width W_0, $f^* \to \frac{96}{Re}$ as $b \to 1$. By ensuring that $72\nu^2 \ll W_0^2$, through the value of ω selected, a value of f^* in correct quantitative relation with Re was obtained by using $b = 1$ throughout, and a zero of velocity (no-slip wall) was located very close to the lattice edge.

Adapting equations (5.5) and (5.12) to EILBGK simulations, in which $\Delta p/\rho$ is determined by $\frac{1}{3}\Delta\rho$, the total density drop along a length L_0 of channel, we obtain lattice versions of the same equations,

$$f^* = \frac{4}{3}\Delta\rho\frac{W_0}{L_0\bar{u}^2}\ , \tag{5.18}$$

$$f^* = \frac{96}{Re^*}\ , \tag{5.19}$$

in which $\bar{u}$ is the y-averaged *lattice* fluid velocity. f^* was obtained for given b and measured Δp, using (5.18), over a range of different Re. From (5.17) one expects a plot of f^* vs. $1/Re^*$ to have a gradient controlled by bounce-back fraction b and plotting this gradient $m(b)$ over a range of b, see figure 5.7, we obtain results in agreement with the theoretical form of (5.17) above. Note that the value of collision scalar ω in use influences the value of b required to give a particular value of f^*.

Whilst to obtain a consistent pressure drop along the system then, requires the use of a particular bounce-back fraction, the velocity field was observed to be less sensitive to b. Considering the pattern of flow generated in the backward-facing step of section 5.4, varying b between 0 and 1 produced, in qualitative terms, little effect on the stream function $\psi(x, y)$, where,

$$\psi(x, y) = \int_{y'=0}^{y'=y} v_x(x, y')\, dy'\ , \tag{5.20}$$

and attempts to measure its influence on the re-attachment length also showed b to have little effect. Variations in the value of parameter b were observed to have a marked effect upon values of the total pressure drop along a given section of the system. The pressure field corresponding to a simulation of flow past the expansion

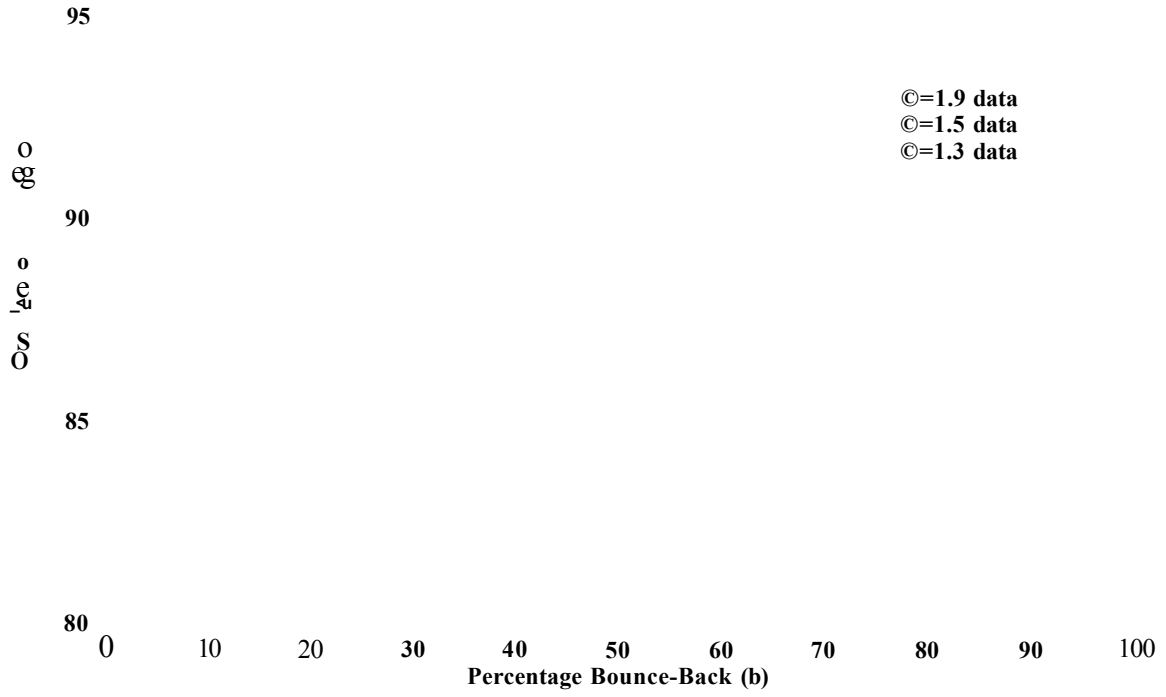

Figure 5.7: The fraction *b* of link densities not reflecting specularly at wall sites and the corresponding gradient m(b) of the plot of *lattice* friction factor /* versus lattice Reynolds Number *Re**.

is shown in figure 5.8a. The non-uniformity of the pressure field is clear, and its qualitative features were stable.

5.4 Comparison with Experiment

We consider as a test-bench problem flow over a backward-facing step. There is a large body of experimental data on this geometry, and for the purpose of this study we have chosen that of Denham *et al* [53]. In order to make comparisons with the

reported experimental data in [53], in this section Reynolds number is defined as follows,

$$Re = \frac{W_0 \bar{v}}{\nu} , \tag{5.21}$$

where W_0 is the width of the channel upstream of the step, and $\bar{v}$ is the average velocity across the narrow channel.

A calibration to assess maximum accessible Reynolds number was carried out by fixing the relaxation parameter ω and increasing $\bar{u}$ through parameter u_0, see section 5.2.1, for a set system size. Compressibility effects were found to be small from an inspection of the velocity field in the form of the contour plot of the stream function $\psi(x, y)$, in the outlet of the channel, well behind the step, as shown in figure 5.8. In the exactly incompressible scheme, the streamlines of $\psi(x, y)$ are parallel in this region and thus it may be inferred that the velocity field shows no evidence of systematic increase in $\bar{u}$, as shown in figure 5.5 using a standard scheme to simulate duct flow. Moreover the pressure field shown in figure 5.8, from which the extent and non-uniformity of the variations is readily apparent, is fully consistent with uniform decay. This was observed to remain the case for all values of inlet profile parameter u_0 up to that which induced instability in the EILBGK simulation. A system of size 600×30 was driven with matched equilibrium forcing at inlet, and outlet, using a value of $\omega = 1.9$ chosen as a compromise between low viscosity and stability. The value of b in use was determined on the basis of the value of f^*, measured for flow in an infinite aspect ratio duct as in figure 5.3, again with $\omega = 1.9$.

For purposes of comparison with experiment, the length of the duct outlet down-

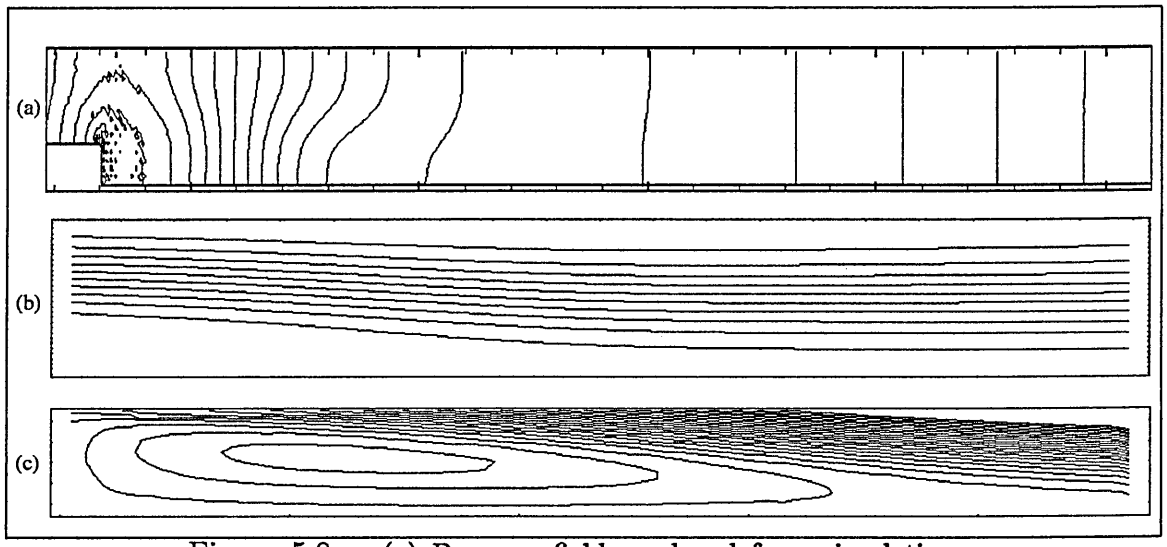

Figure 5.8: (a) Pressure field produced from simulation of back-facing step. (b) Stream function $\psi(x, y)$, evaluated numerically (using a trapezium rule integration). It can be seen that Poiseuille flow redevelops downstream of the step. (c) Detail of recirculating region directly behind the step. Note that in (a) the end of the step is shown, in both (b) & (c) the stream function is shown immediately right of the step.

stream of the step (figure 5.1) was determined by trial and error, to be sufficiently long such that it had no measurable influence upon the re-attachment length L of the recirculating region behind the expansion. L was measured in units of the step height, as the distance downstream of the step to an interpolated zero in u_x.

Figure 5.9 shows dimensionless L/H as a function of Re. These data were obtained from the final steady-state of simulations using $\omega = 1.9$, initialised uniformly to $N_{\sigma i} = \rho_0 N_{\sigma i}^{eq}(0)$, with a node density of $\rho_0 = 1.8$, and allowed to equilibrate over 40,000 time steps (although flows were observed to have reached equilibrium by 25,000 steps). Stability of the scheme was checked for in the manner discussed at the beginning of section 5.2.1. Figure 5.2 shows the time variation of the total lattice

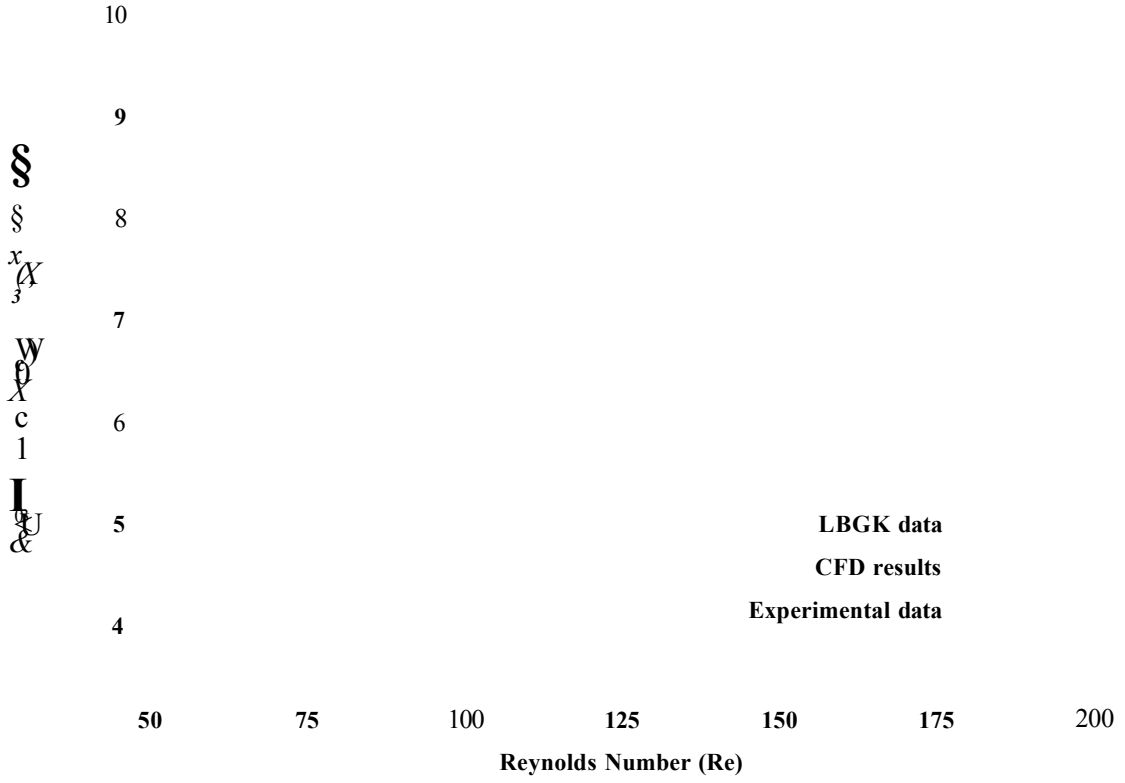

Figure 5.9: Comparison of reattachment length data obtained from LBGK backward-facing step simulations with experimental data of Denham *et al*.

mass M(t), where,

$$M(f) = \pounds \quad \bullet \qquad (5\text{-}22)$$

The simulation results in figure 5.9 are overlaid with experimental data lifted from pseudo two-dimensional experimental measurements made in the central plane of the apparatus represented in figure 2 of reference [53] and with comparable calculations made using standard CFD [54]. Whilst agreement with CFD is good, that with the *experimental* data points (admittedly obtained crudely from enlargements of figure 7a of [53]) shows a less close correspondence, certainly compared with the match

achieved, between the standard scheme and *theory* on lid-driven cell geometries [41, 42]. This disparity possibly originates from the comparatively large pressure gradients present in our simulation, which are significantly less in the confined lid-driven-cell geometries. The latter essentially experience restricted pressure changes because of the confinement of the fluid.

5.5 Discussion and Conclusions

We have applied an EILBGK simulation to internal, pressure-driven flow in which non-uniform pressure gradients are to be expected, demonstrating with this approach a need to adjust the fraction of bounce-back, b, applied to link densities at no-slip boundaries of LBGK simulations to recover correct mechanical stresses at a static wall. Adjusting b in this way has allowed the LBGK method to recover a correct value of friction factor, f^*, for flow in an infinite aspect ratio rectangular duct. This value of b significantly influences the measured pressure drops when applying modified LBGK simulation to internal, pressure driven flow.

Use of forced boundary conditions allows development of stable, parabolic boundary profiles in relatively small regions of lattice and thus introduces an improvement in the efficiency of the method. Forced boundary conditions also have inherent flexibility (being capable of direct application where a boundary velocity profile and pressure are required) and bring LBGK simulation closer to CFD practice. For example, a solenoidal flow field is readily established using a forced boundary

condition, but is tedious to apply using usual traditional LBGK methods. Moreover we have seen that it is possible to simulate open boundary conditions in a modified scheme with ease, making for simple implementation again more consistent with conventional CFD.

Using an EILBGK scheme, by decreasing lattice viscosity and using lattice closure rules which allow a fuller control of the pressure field, we have, without compressibility error, achieved Reynolds numbers up to $Re \approx 250$. Beyond this value of Re there is a loss in stability if the viscosity is too small. By comparison, standard LBGK shows compressibility error by $Re \approx 22$ for the problem. This is illustrated quantitatively in figures 5.10 and 5.11. There are differences in the recirculation length calculated by the standard and EILBGK schemes, figure 5.11 shows this to be about 10% at $Re = 22$. But the two schemes differ most noticeably in terms of velocity divergence as seen in figure 5.10.

Comparisons of LBGK simulation with particular analytical solutions of the lid-driven cavity test bench test problem [42] deal with completely confined fluids so that the pressure fields encountered are more homogeneous. This possibly accounts for the closer agreement between *theory* and CFD that these simulations produce, over that which we report here *with experiment.* Also work by Armaly *et al* [55] has noted that velocity profiles at the step in the data of [53] strongly deviates from the parabolic profile expected for laminar flow, consequently despite the uniformity in its geometry the experimental data of [53] may yet retain three-dimensional behaviour. Notwithstanding, the data developed for comparison, from traditional numerical

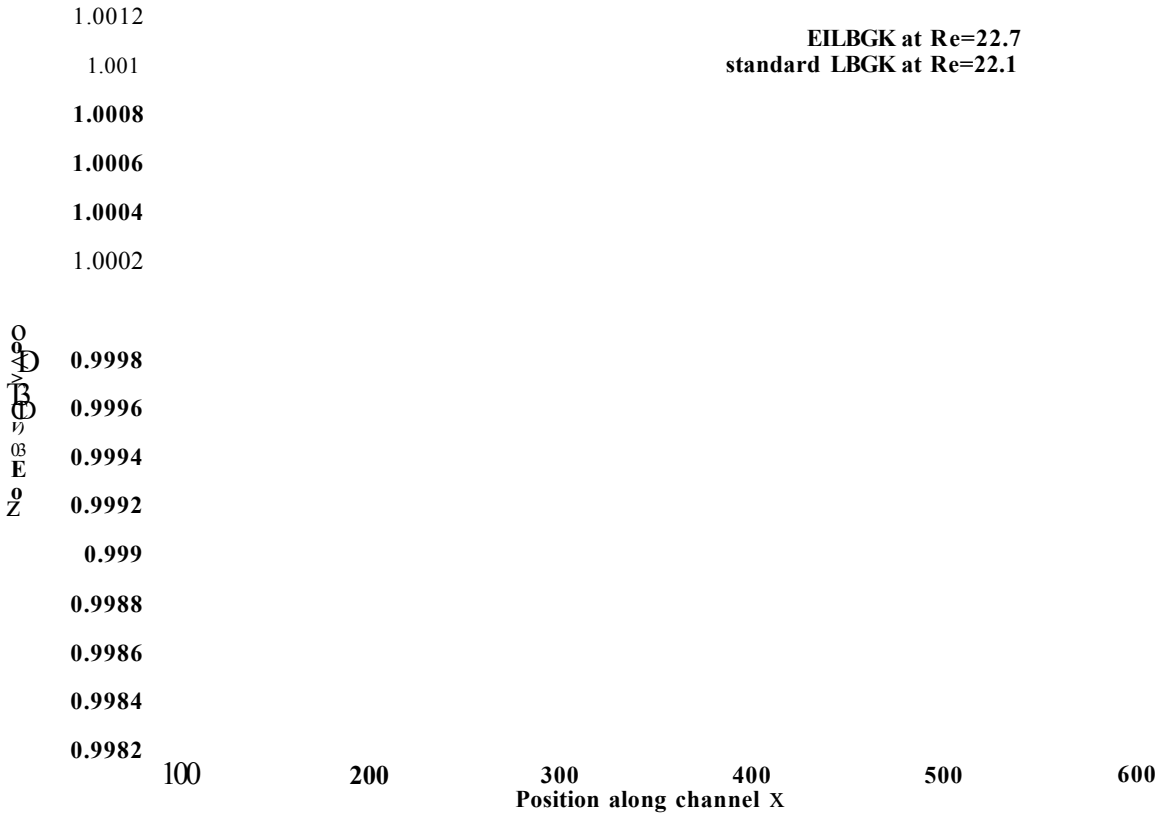

Figure 5.10: Width-averaged velocity *v(x)* plotted as a function of position X, downstream of the step. Standard scheme data corresponds to an outlet velocity of 0.019356. EILBGK scheme to an outlet velocity of 0.019954.

solution of the incompressible Navier-Stokes and continuity equations, is in better agreement with our LBGK results and whilst, for our application, the former offers considerably greater efficiency, it appears not to produce significantly better agreement with experiment.

Where the pressure field is uniform, standard LBGK can achieve still higher *Re* and also capture hydrodynamic time dependence. EILBGK should thus be seen as complementary to the standard approach, a full comparison of the relative accuracy

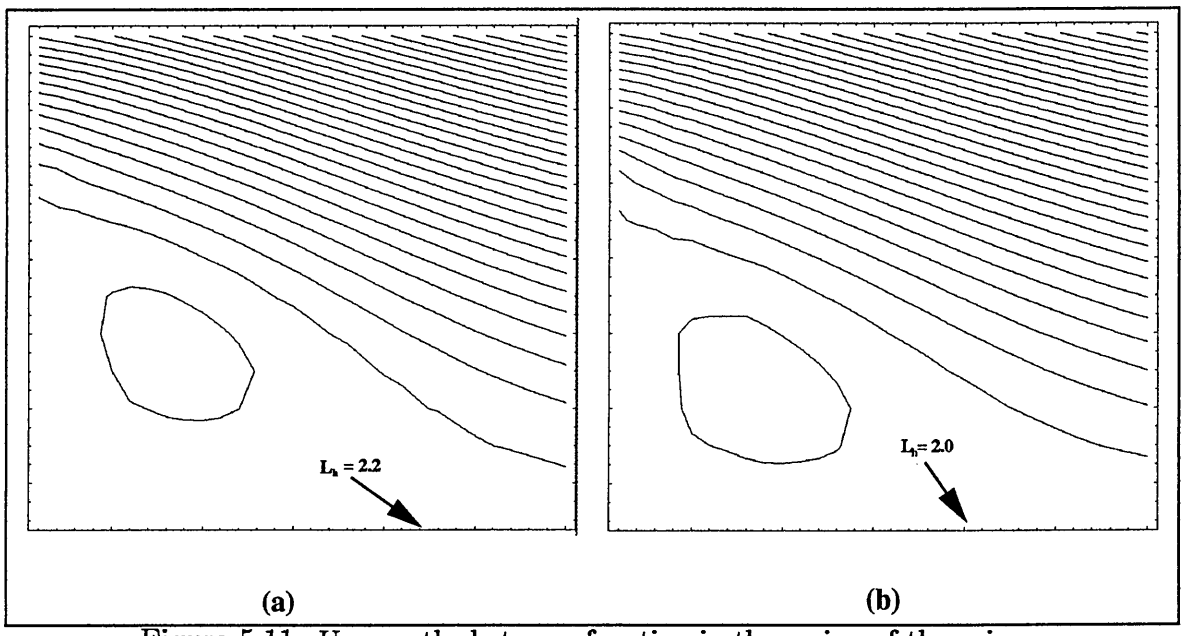

Figure 5.11: Unsmoothed stream function in the region of the primary vortex, for (a) the EILBGK scheme at $Re = 22.7$ with $L_h = 2.2$, and (b) standard LBGK at comparable $Re = 22.1$ with $L_h = 2.0$. The point of re-attachent (arrowed and expressed in units of the step-height) was calculated by locating the zero in velocity close to the horizontal wall.

and stability being primarily of academic interest only. Where boundary conditions permit, the simulator is likely to wish to retain the advantage of hydrodynamic time dependence.

Nevertheless, we have shown that for certain applications, modified and appropriately-bounded EILBGK schemes offer economic access to a fuller control of the pressure field and increased Reynolds number.

Chapter 6

Depth-Averaged Flow Simulations

6.1 Introduction

In this chapter we proceed to validate the assumptions of section 2.8 numerically, particularly the statement that in depth-averaged flow calculations the influence of the unmodelled dimension can be accounted for by the stress term S_α alone (see (2.54) through (2.60)). Then we present results of EILBGK depth-averaged simulations applied to a test simulation of flow in a bifurcating duct, and make comparisons with CFD results. As in chapter 5, we make use of the friction factor for the purposes of calibration, in the present context to ensure the unmodelled walls have the correct influence on the flow field.

6.2 Numerical Scheme for Steady Incompressible Flow in a Uniform Duct

To investigate the assumptions of the section 2.8, we consider in this section direct numerical and analytical calculations of steady-state incompressible flow in a wide, shallow duct.

We consider a long, uniform duct of the geometry shown in figure 6.1, in which

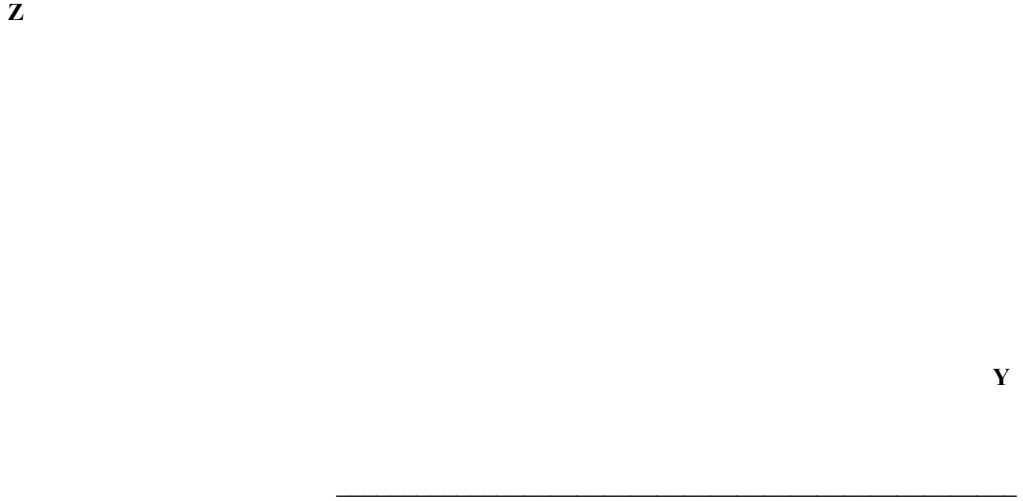

Figure 6.1: Geometry of depth-averaged flow problem.

Lx ^> Ly Lz. The governing equations for an incompressible fluid in an isothermal regime are, as usual,

$$dfiVp = 0 , \tag{6.1}$$

$$dtva + {}_{dpVpVa} = -d\,a + vdpdpVa , \tag{6.2}$$

where, we remind the reader, d is the density of the actual fluid.

General arguments are now applied to the velocity and pressure fields. We are only interested in steady-state, laminar flow which in this geometry, with a uniform cross-section, can have no y or z velocity components, from which it follows that the pressure gradient is unidirectional in the x-direction. Moreover, consider the second term in (6.2),

$$\partial_\beta v_\beta v_\alpha = v_\beta \partial_\beta v_\alpha \ ,$$

which reduces further (due to $v_y = v_z = 0$) to become,

$$\partial_\beta v_\beta v_\alpha = v_x \partial_x v_\alpha \ .$$

There only being a x-direction velocity component the subscript α above becomes x, and due to the uniformity of the duct is a function of y and z only. So, there is still further simplification and the advective term vanishes altogether,

$$\partial_\beta v_\beta v_\alpha = 0 \ . \tag{6.3}$$

The governing equations thus become,

$$\partial_x v_x = 0 \ , \tag{6.4}$$

$$\partial_x \left(\frac{p}{d}\right) = \nu \left(\partial_y^2 + \partial_z^2\right) v_x \ . \tag{6.5}$$

On the grounds of translational symmetry, the pressure is taken to be,

$$p(x) = p_0 - Mx \ , \tag{6.6}$$

where p_0 is a constant, and M is the gradient in pressure along the system.

On appeal to the definition for the pressure gradient, (6.6), the momentum equation reduces, for the problem of flow in a uniform shallow duct, to that of solving Poisson's

equation,

$$\eta \left(\partial_y^2 + \partial_z^2\right) v_x = -M \ , \tag{6.7}$$

note, (6.7) contains the *shear* viscosity, $\eta = \frac{\nu}{d}$. We seek a numerical solution and

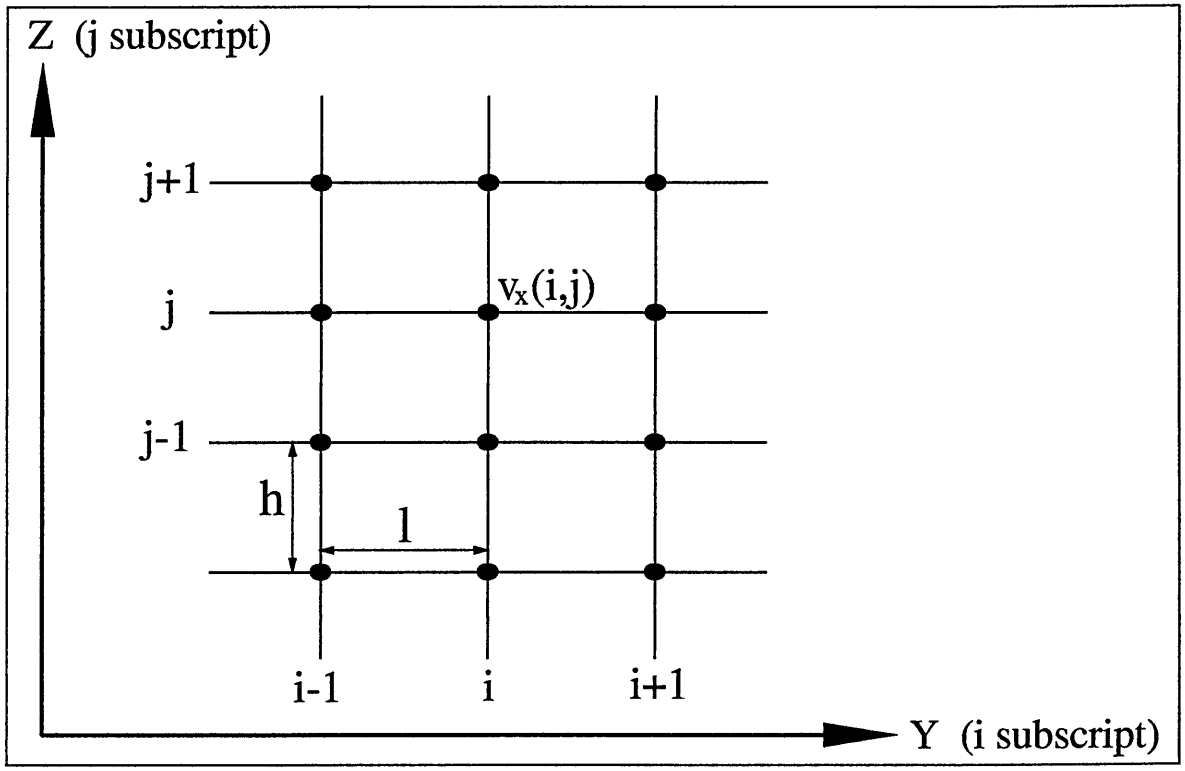

Figure 6.2: Rectangular grid used for numerical solution of depth-averaged flow equations.

discretise the equations on a rectangular mesh, approximating the derivatives in (6.7) using central differences. Such an approximation for a first derivative would be, using a mesh as shown in figure 6.2,

$$\frac{\partial v_x}{\partial y}(i + l/2, j) = \frac{v_x(i+1, j) - v_x(i, j)}{l} \ , \tag{6.8}$$

and similarly,

$$\frac{\partial v_x}{\partial y}(i - l/2, j) = \frac{v_x(i, j) - v_x(i-1, j)}{l} \ . \tag{6.9}$$

A second derivative is simply the rate of change of the first derivatives so,

$$\frac{\partial^2 v_x}{\partial y^2}(i,j) = \frac{\left(\frac{v_x(i+1,j)-v_x(i,j)}{l}\right) - \left(\frac{v_x(i,j)+v_x(i-1,j)}{l}\right)}{l}, \tag{6.10}$$

$$= \frac{v_x(i+1,j) - 2v_x(i,j) + v_x(i-1,j)}{l^2}. \tag{6.11}$$

Applying the same methodology to the z-direction (remembering the vertical step length is now h), we substitute into our governing equation (6.7) to obtain the finite difference form,

$$-\frac{M}{\eta} = \frac{v_x(i+1,j) - 2v_x(i,j) + v_x(i-1,j)}{l^2} + \frac{v_x(i,j+1) - 2v_x(i,j) + v_x(i,j-1)}{h^2}, \tag{6.12}$$

which is simply manipulated to give our final finite difference equation,

$$v_x(i,j) = \frac{1}{2\left(h^2+l^2\right)}\Big\{ h^2 v_x(i+1,j) + h^2 v_x(i-1,j) + l^2 v_x(i,j+1) + l^2 v_x(i,j-1) + h^2 l^2 \frac{M}{\eta} \Big\}. \tag{6.13}$$

Applying the usual no-slip (Dirichlet) boundary condition on v_x at the walls, our finite-difference scheme (6.13) was iterated to steady-state for a range of duct aspects, A (defined as L_y/L_z), and Reynolds number (the latter controlled through the size of the pressure gradient M inducing the flow). Depth-averaged quantities of interest were then calculated from trapezium rule integration, and spatial derivatives were evaluated from mesh differences. In this way values for the cumulant and stress terms, $\frac{S_\alpha}{L_z}$ and $\partial_\beta C_{\alpha\beta}$ in (2.57) were obtained. Figure 6.3 shows the y-averaged value of the ratio $\frac{S_\alpha/L_z}{\partial_\beta C_{\alpha\beta}}$, R, estimated in (2.59) plotted as a function of A/Re. A clear linear trend emerges for the range of $80 \leq A \leq 1400$ and $7 \leq Re \leq 35,000$ used to compile this data. These results support the view that for large values of A/Re the

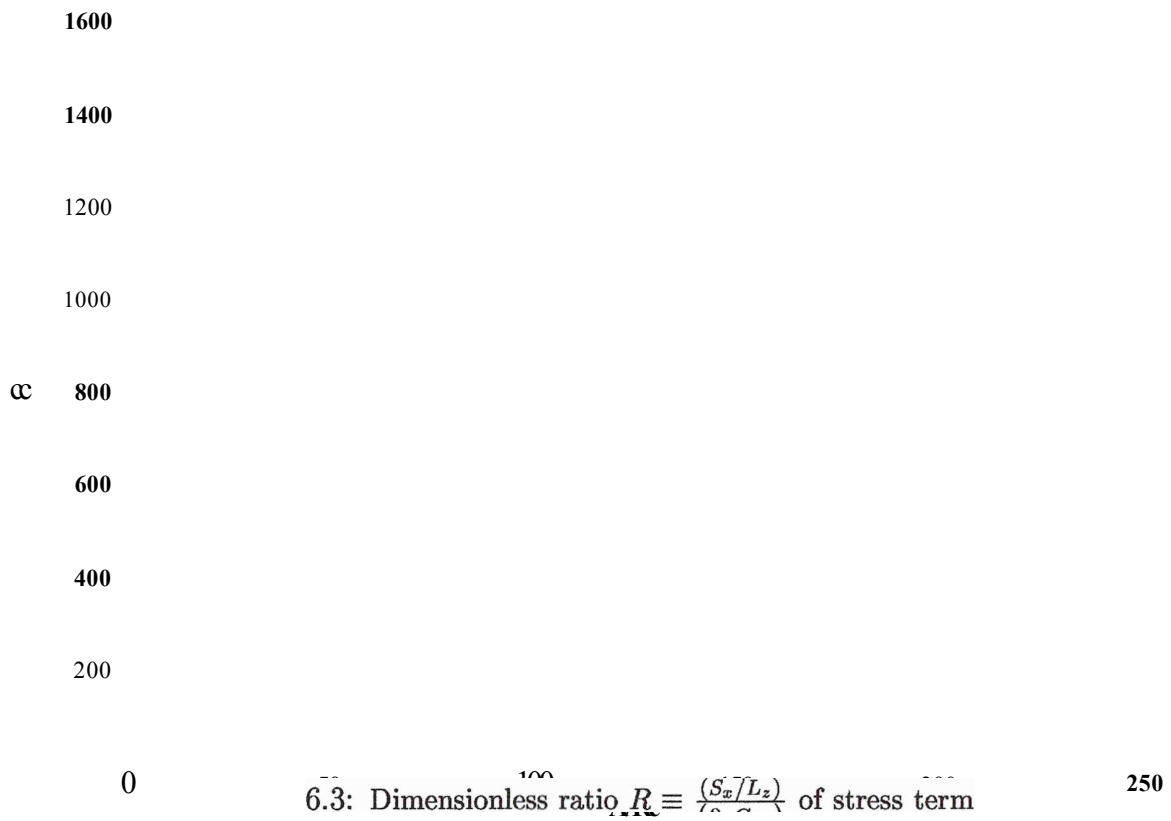

Figure 6.3: Dimensionless ratio $R = /fxLLz\ of$ stress term
to cumulant term obtained by finite-difference calculations of z-averaged flow in the duct of figure 6.1.

artifice of a fictitious body force is sufficient for flow to be treated in two-dimensions, the influence of the formally unmodelled surfaces manifesting itself in an effective body force impressed throughout the 2D fluid and represented by stress term Sa of expression (2.57) alone.

6.3 EILBGK Depth-Averaged Flow Experiments

6.3.1 Boundary Conditions

In this section we describe the forcing and calibration used in our EILBGK simulations of depth-averaged flow introduced in section 4.3 and present results. As with our pressure-driven flow experiments of chapter 5 the forcing applied over 'open boundaries' allows the simulator to gain fuller control of the fluid pressure field and avoids the use of the more usual approach of a uniformly impressed body force, which whilst it is a valid means of forcing flow where the pressure gradient is known to be uniform, cannot correctly represent a spatially variable pressure field.

In section 5.2.1 we introduced *equilibrium forcing*, in which, at an open boundary the pressure is allowed to develop to a value consistent with the other set boundaries (inlet and outlet velocities being continually set, recall, by fixing $N_{\sigma i}^{eq}(\mathbf{u}, \rho)$ to a value determined by a target boundary velocity).

In this chapter we also implement what we term *free profile conditions*, which impose set pressure drops on the system between open boundaries. Again, at the inlet, both a pressure and velocity profile are specified. However, with our *free profile* conditions, a uniform pressure (lattice density) is set at the outlet, by the user, with the velocity $\mathbf{u}$ from the node downstream now used to set all boundary densities to equilibrium value $N_{\sigma i}^{eq}(\mathbf{u}, \rho)$, allowing outlet velocity freely to develop, after the 'upwinding' technique of traditional CFD.

Having dealt with open boundaries, we proceed to relate the means by which the no-slip boundary conditions required for the ducts' static, resolved wall were calibrated with reference to flow friction factor. Indeed, working within an exactly incompressible scheme, the friction factor also provides a useful verification of the influence of the unmodelled walls, ie. of depth parameter k.

6.3.2 Friction Factor

In chapter 5 we have already investigated the no-slip boundary conditions imposed on explicitly modelled walls via the friction factor calculations presented. We may now use the friction factor as a check on the simulation's behaviour in the unmodelled z-direction, and as a check upon our interpretation of the role of parameter k, discussed in section 4.3.

From chapter 5 we know that for physical duct flows, the friction factor f relates average flow profile velocity $\bar{u}$ to the pressure Δp developed along the duct and fluid viscosity. As we have seen (section 2.8), the profile flow sampled in the unmodelled z-direction is parabolic, so,

$$f = \frac{\Delta p}{d} \frac{2L_z}{L_0} \frac{2}{\bar{u}^2} , \tag{6.14}$$

which of course is derived directly from the definition of f for flow along an infinitely deep duct with *width* L_z and length L_0 (see beginning of section 5.3). Also from section 5.3 we know that (6.14) may be reduced to,

$$f = \frac{96}{Re} , \tag{6.15}$$

where the Reynolds number is based upon hydraulic diameter $2L_z$, ie.

$$Re = \frac{2L_z\bar{u}}{\nu} \ . \tag{6.16}$$

Adapting (6.14) and (6.15) to our EILBGK scheme, in which $\Delta p/d$ is determined by $\frac{1}{3}\Delta\rho$, the total lattice density drop along the whole length of channel, we obtain a lattice version of equation (6.14),

$$f^* = \frac{4}{3}\Delta\rho\frac{L_z}{L_0\bar{u}^2} \ , \tag{6.17}$$

$$f^* = \frac{96}{Re} \ , \tag{6.18}$$

where $\bar{u}$ is now average *lattice* fluid velocity and L_0 and L_z are measured in lattice units.

Consider the steady-state of a 2D lattice of length L_0 in the x-direction, infinite in the y-direction, driven with uniform, matched inlet and outlet profiles $\underline{u_0} = u_0\hat{x}$. Let the inlet density be ρ_{in} and consider the outlet sites' densities to have evolved to a steady-state density ρ_{out} using equilibrium forcing described in section 5.2.1. On general arguments of symmetry,

$$u_\alpha(x,y) = u_0\delta_{\alpha x} \ , \tag{6.19}$$

$$\partial_x\rho = \frac{\rho_{in} - \rho_{out}}{L_0} \ . \tag{6.20}$$

For this situation of uniform translation (no gradients) all link densities will be given by their equilibrium form (4.39) so, in modified evolution equation (4.47) we may set $\Delta_i(N) = 0$ and, with (6.19) and (6.20) in mind obtain,

$$N^{eq}_{\sigma i}(\underline{u_0}, \rho(x + c_{\sigma ix})) = N^{eq}_{\sigma i}(\underline{u_0}, \rho(x)) + \frac{k}{\rho}N^{eq}_{\sigma i}(0)c_{\sigma ix}u_x \ , \tag{6.21}$$

in which, recall, k parameterises the effect of the unmodelled walls.

Substituting, from (4.39) for $N_{\sigma i}^{eq}(\underline{u_0}, \rho(x+c_{ix}))$ and $N_{\sigma i}^{eq}(\underline{u_0}, \rho(x))$ we note that, since the velocity field is uniform [see (6.19), and, remember *in the EILBGK scheme, variations in the lattice density are not communicated into site velocities*] all terms involving $\underline{u_0}$ cancel from (6.21). After a Taylor expansion and some algebra (6.21) yields,

$$c_{\sigma i\alpha}\partial_\alpha \rho = k c_{\sigma i\alpha} u_\alpha \ , \tag{6.22}$$

which, for the present geometry, reduces to the exact result,

$$\frac{\rho_{in} - \rho_{out}}{L_0} = \frac{\Delta\rho}{L_0} = k u_0 \ . \tag{6.23}$$

Equations (6.23) and (4.56) may be substituted into (6.17) to obtain reassurance of the result required by hydrodynamics,

$$f^* = \frac{96}{Re^*}, \tag{6.24}$$

here, $Re^* = 2u_0 L_z/\nu(\omega)$ is based upon the unmodelled depth of the parent 3D duct.

Using periodic boundary conditions it is straightforward to simulate this semi-infinite lattice and, measuring the gradient in lattice density ρ along the flow direction, to calculate f^* from (6.17) with L_z obtained from the set value of k through (4.56). Simulations were performed for values of unmodelled depth parameter k in the range $0.0008 \leq k \leq 0.01$, each being driven with a uniform velocity profile ranging in $0.023 \leq v_0 \leq 0.271$ in lattice units. The average velocity $\bar{v}$ was confirmed to be of constant value throughout each simulation, 40,000 time steps being sufficient

easily to ensure a final steady-state. Across all tests performed, u, was set to 1.9 and pressure drops of the order 3.7 x 1CT1 were recorded. For a particular k value the lattice friction factor, /*, and Re were calculated for each velocity profile and the values plotted against each other. Over the range of parameters considered the gradient $m(b)$ was measured to be extremely close to 96.

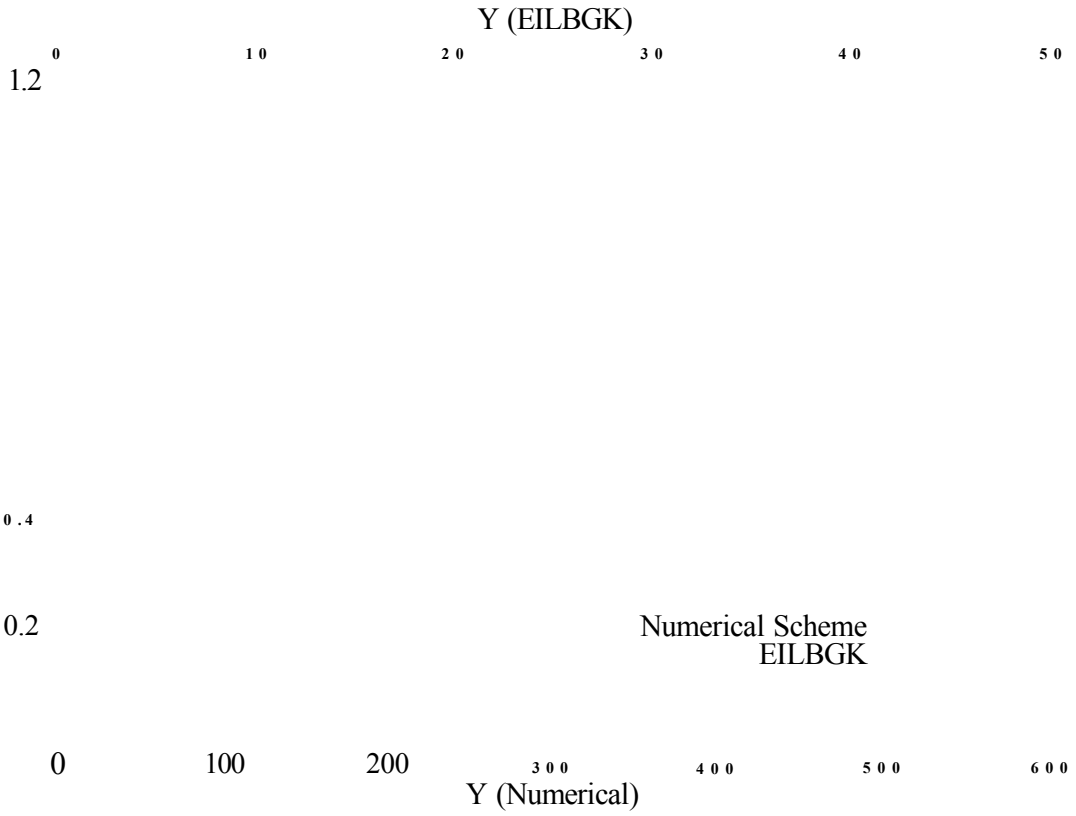

Figure 6.4: Z-averaged velocity profiles across the duct of figure 6.1 for equivalent Reynolds Number and effective Lz (k parameter).

Figure 6.4 shows the depth-averaged velocity sampled across a long, uniform duct calculated using modified EILBGK simulation compared with that calculated numerically after section 6.2 for the system of figure 6.1. The close correspondence

between these two sets of results further underlines the validity of the EILBGK model.

6.3.3 Bifurcating Duct

We choose as an illustrative example flow near a bifurcation in a shallow duct, concentrating on the qualitative dependence upon pressure driving of the deflection of the principal flow. With bounce-back conditions (bounce-back factor $b = 1$) on velocity at the resolved walls, solid lines figure 6.5, values of inlet velocity and k were chosen so that was large.

Figure 6.5: Diagram showing geometry of bifurcating duct.

Figure 6.6 shows, through the stream function (see below), the flow profile obtained in a bifurcating duct of figure 6.5; and figure 6.7 shows the associated pressure field. Open boundary conditions were imposed on the pressure at both outlets with Dirichlet conditions on the velocities corresponding to uniform profiles. Also, simulations were performed using our free profile conditions where uniform profiles were set at the inlet but developed naturally at both outlets. Both approaches to setting the boundary conditions yielded qualitatively similar results, but only those obtained using the latter boundary conditions are presented here. The length of both outlet channels was increased until the qualitative features of the flow in the region of the bifurcation were seen to be insensitive to any further elongation. The parameters used in simulation were $\omega = 1.9$, $k = 0.3$ (therefore $L_z \approx 1.0$), and $L_y = 45$. The pressures were set to $P1 = 0.60$, $P2 = 0.48$ and $P3$ gradually increased, using the values 0.514 , 0.528 and 0.540 until the flow direction was reversed in the horizontal exit (see figure 6.6c).

The stream function used to display the velocity field in figures 6.6 was obtained from a numerical integration (trapezium rule) approximating,

$$\psi(x,y) = \int_{y'=0}^{y'=y} v_x(x,y')dy' \ . \tag{6.25}$$

The pressure field corresponding to the flow close to the bifurcation, figures 6.7, is clearly non-uniform. The extent to which the pressure varies throughout the simulated system is clear, and whilst the qualitative features of this field are stable, variations in the value of wall collision parameter b were observed to have a marked effect upon numerical values, underlining the importance of calibrating the modelled

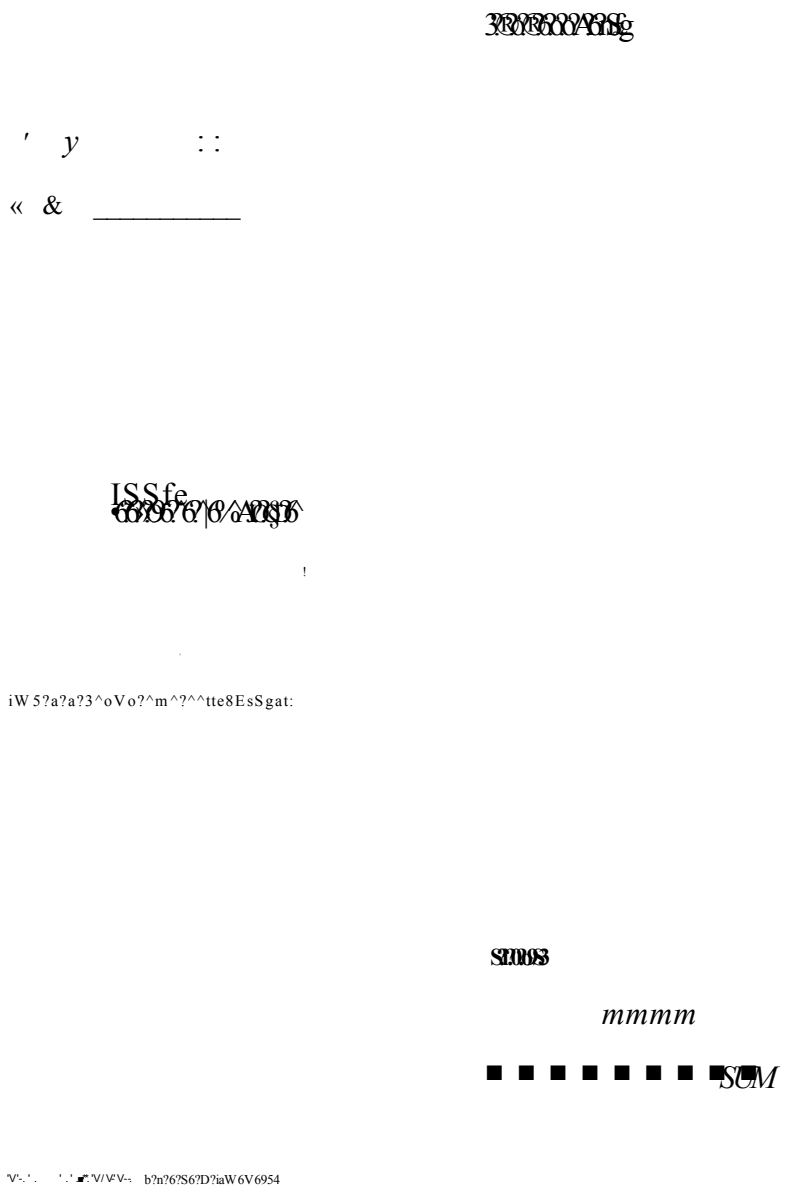

Figure 6.6: Stream lines obtained from EILBGK calculation for laminar flow in a shallow bifurcating duct, where ^ « 50. (a) Inlet pressure higher than right hand exit, which is higher than top exit. Majority of flow deflected towards top exit, (b) On increasing right hand pressure negligible flow through to right exit, (c) On further increase in pressure at right hand side exit, flow now enters here as well as inlet.

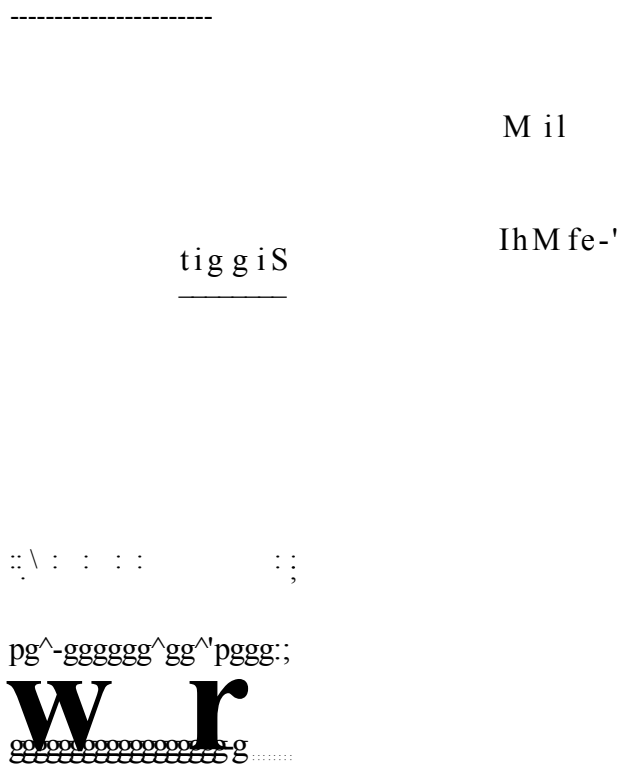

Figure 6.7: Pressure contours corresponding to velocity fields of figures 6.6. Note the uniformity of the pressure gradient in the inlet and outlet.

wall's collision step.

For the purposes of comparison, a two-dimensional model of the laminar flow within the bifurcating duct was set up using version 1.6 of the PHEONICS flow modelling package. The flow domain was represented using a non-uniform 60×40 calculational grid, in which the solid regions adjacent to the vertical exit of the duct were 'blocked off' by defining them as regions of zero porosity.

Pressure boundary conditions were defined at the inlet and exit planes of the domain, consistent with those assumed in the accompanying analysis. As a consequence of the two-dimensional treatment used in this work, the principal flow resistances arising from the shear stresses at the unmodelled surfaces of the flow domain could not be modelled directly. Therefore it was necessary to represent this effect through the use of additional momentum sinks applied to each of the velocity components distributed throughout the flow domain.

The form of the fluid momentum sinks used in this work was based on the following pressure loss definition,

$$\frac{\Delta p}{\Delta x} = -\frac{1}{2}\rho|\mathbf{u}|u_x\frac{f}{2L_z} \,. \tag{6.26}$$

We know from chapter 5 that for flow in a smooth walled duct it can be shown that the friction factor f may be expressed as,

$$f = \frac{96}{Re} \,, \tag{6.27}$$

where,

$$Re = \frac{2L_z\bar{u}}{\nu} . \tag{6.28}$$

Using this model described above, the resulting flow field was solved and the predicted streamlines are presented in figure 6.8 for comparison with those in figure 6.6.

6.4 Discussion and Conclusions.

In this work we have analysed the Navier-Stokes equations and devised, for ducts of uniform depth, a condition for the application of laminar, depth-averaged flow modelling over fully-resolved three-dimensional calculations.

Modifications to the EILBGK simulation method, mapping the scheme onto the structure of a partially-integrated, steady-state Navier-Stokes equation (with new associations for the unmodelled depth of duct, which is controlled through our parameter k) have been presented and shown to recover correct hydrodynamics. It has further been demonstrated, both by analytical calculation and by simulation, that the parameter k lies in correct relation with pressure jumps obtained by application of open boundaries to the EILBGK scheme applied to internal, pressure-driven flows.

Our method increases the capacity of LBGK simulation to deal with flows in which the principal (flow inducing) boundary conditions are specified in terms of pres-

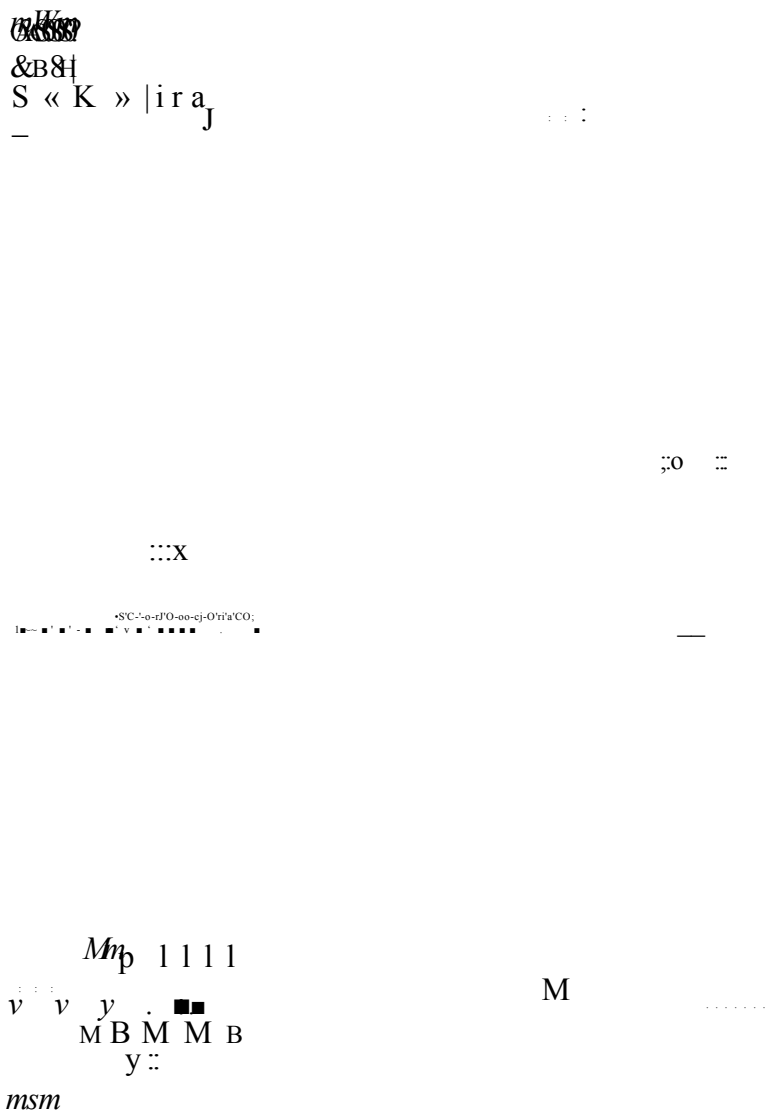

Figure 6.8: Streamlines obtained from CFD calculation of bifurcating problem, using same pressures as specified for LBGK calculation.

sure, and has brought LB methods closer to CFD practice : using the core EILBGK method again allows one to avoid both the error due to compressibility effects (whilst actually calculating pressure jumps) and the artifice of a uniformly imposed body force to drive flow. Both these benefits accrue from the manner in which the boundary conditions have been applied and not from any modification to the bulk scheme. They are therefore, quite general and not confined to purely depth-averaged flows.

In modifying the EILBGK scheme the possibility of generation of a sink term in the continuity equation has been deliberately avoided. Such a term may have proved useful in applications of the method to ducts of non-uniform depth and possibly as a means to model the shallow water equations.

Our model is still laminar. In traditional CFD the influence of turbulence is incorporated usually by some 'law of the wall'. Turbulence in the layer of fluid in contact with the no-slip boundaries of our calculation would undoubtedly modify the stress terms of (2.54) but (provided the appropriate Reynolds number could be accessed), we suggest that a phenomenological modification is all that obstructs incorporation of some turbulent effects.

Chapter 7

Thermal LBGK Simulations

7.1 Introduction

In this chapter we report the results of simulations using our thermal LBGK model as introduced in section 4.4.

Applications of LBGK schemes which incorporate energy transport have been restricted to *free* or *natural* convection flow problems such as Rayleigh-Bernárd convection [37,38,56], or, Couette flow [35,36] so that viscous dissipation terms can be studied. Certainly the geometries selected for these test simulations in [35–38,56] are of physical interest. However, in many *practical* situations viscous dissipation is often negligible. Moreover previous thermal models are known to be highly unstable (much more so than the corresponding isothermal schemes [37]) and as a result, they have been used only to treat small temperature variations [57].

We find that these limitations can be overcome by treating the temperature through a de-coupled *internal energy distribution.* That is as a passively advected scalar quantity. This is the approach we have taken in our thermal model - the macroscopic governing temperature equation is effectively solved using a *second distribution*, nominated $\varepsilon_{\sigma i}$'s, which are evolved by a relaxation method similar in nature to that controlling the momentum densities (see chapter 4). Note that with this approach it is impossible to capture the correct form for viscous dissipation in the models' resulting thermohydrodynamics. However, these effects are often negligible in engineering flow geometries.

Our model enjoys the advantage of an adjustable Prandtl number achieved by using two different BGK single-time relaxation parameters to model thermal and momentum relaxation. (Other models in the literature achieve this by resorting to more complicated collision operators [37, 56].)

The model considered in this chapter is conceived, therefore, to simulate fluid flow in the Boussinesq-Oberbeck approximation. For flow within this regime we can appeal to a particularly useful test-bench calculation with a known solution - the forced flow of a fluid between infinite parallel plates, subject to constant heat flux boundary conditions. Consequently we are able to make comparison with both analytical and standard CFD results for this geometry. We show that our model, constructed over a straightforward $D2Q9$ standard scheme (note that it is not necessary to increase the complexity of the unit cell to the extent used in other thermal LBGK models [32, 36, 56]) recovers the correct steady-state Nusselt number, Nu, for the

geometry simulated. Moreover, our thermal scheme would appear to be as stable as the parent isothermal model. (A *complete* stability analysis is however somewhat beyond the present scope of this project, although some analysis has been carried out on previous models [37, 58].)

7.2 Analytical Results

In order to establish the key analytical results, we derive here the expected Nusselt number for constant heat flux boundary conditions at the walls of an infinitely deep duct containing parabolic flow, see figure 7.1. Note that the origin of co-ordinates is in the centre plane of the duct, as marked in figure 7.1, which is significant when we come to measure observable quantities.

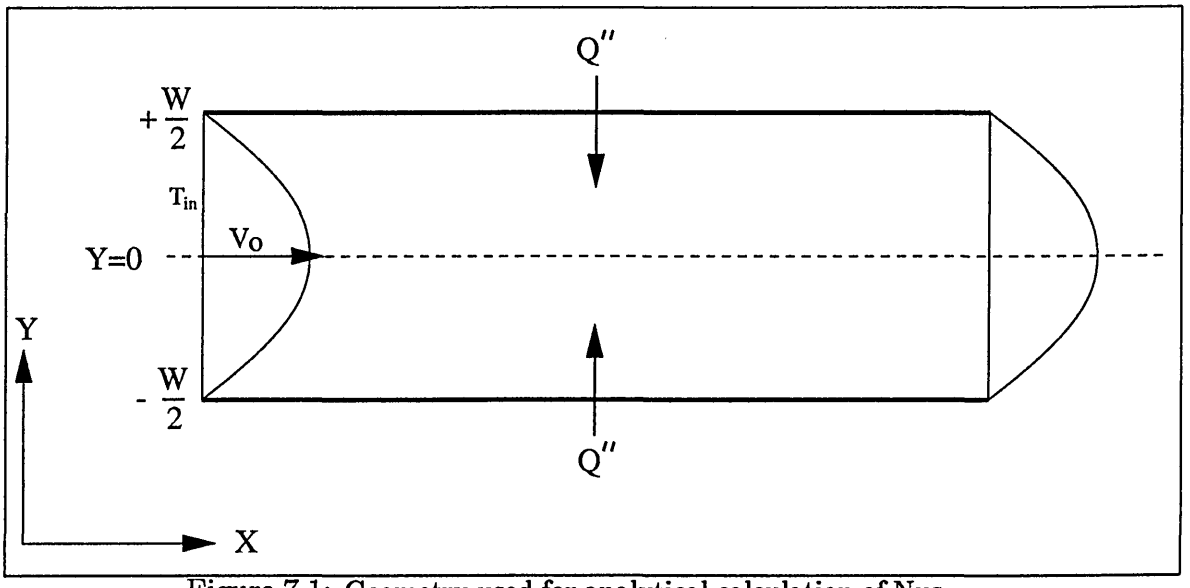

Figure 7.1: Geometry used for analytical calculation of Nusselt number.

At steady-state the governing Boussinesq equation for the temperature field is, from (2.45)

$$v_\alpha \partial_\alpha T = \chi \partial_\alpha^2 T \ , \tag{7.1}$$

which, on neglecting axial *conduction* and realising that there will be no y-component of velocity (7.1), reduces to the following partial differential equation,

$$v_x \frac{\partial T}{\partial x} = \chi \frac{\partial^2 T}{\partial y^2} \ . \tag{7.2}$$

The velocity profile across the duct is parabolic with a central maximum designated v_0,

$$v_x = -\frac{4v_0}{W^2}\left(y - \frac{W}{2}\right)\left(y + \frac{W}{2}\right) \ . \tag{7.3}$$

On general grounds of translational symmetry (with constant heat flux boundary conditions applied at the walls) in the bulk of the channel (away from the inlet), one would expect the temperature, T, to increase linearly along the axis length of a duct . T must also exhibit y-dependence so we take the following functional form for T,

$$T(x, y) = Ax + f(y) \ . \tag{7.4}$$

Substituting (7.3) and (7.4) for v_x and T into (7.2) we obtain,

$$\frac{d^2 f}{dy^2} = \frac{4v_0}{\chi W^2}\left(\frac{W}{2} - y\right)\left(y + \frac{W}{2}\right) A \ , \tag{7.5}$$

integrating, we note that the cross-duct temperature has to be an even function,

$$\left.\frac{df}{dy}\right|_{y=0} = 0 \ , \tag{7.6}$$

which implies that the integration constant is zero,

$$\frac{df}{dy} = \frac{4v_0}{\chi W^2}\left(-\frac{y^3}{3} + \frac{W^2 y}{4}\right) A \,. \tag{7.7}$$

To find a form for $f(y)$ we need to integrate (7.7), and require a boundary condition, which we take to be,

$$T = T_{in} \,, \qquad \text{at } x = y = 0 \,. \tag{7.8}$$

Performing the integration we obtain expressions for $f(y)$ which, when substituted in (7.4) yields a form for $T(x,y)$,

$$T(x,y) = Ax + \frac{4v_0}{\chi W^2}\left(-\frac{y^4}{12} + \frac{W^2 y^2}{8}\right) A + T_{in} \,. \tag{7.9}$$

To determine gradient A we consider the given wall flux Q'', evaluated at $\pm\frac{W}{2}$, which is calculated from,

$$Q'' = -k\frac{\partial T}{\partial y} \,. \tag{7.10}$$

Using (7.9) it is easily shown that,

$$A = \frac{3\chi Q''}{k v_0 W} \,. \tag{7.11}$$

Finally, from (7.11) and (7.9), the full form of $T(x,y)$ is obtained,

$$T(x,y) = \frac{3\chi Q''}{k v_0 W}\left[x + \frac{4v_0}{\chi W^2}\left(-\frac{y^4}{12} + \frac{W^2 y^2}{8}\right)\right] + T_{in} \,. \tag{7.12}$$

We define the *flow-averaged* or *bulk* temperature, T_b, which would be the measured temperature if, at position x, the channel was cut and the out-flowing fluid was collected and thoroughly mixed,

$$T_b = \frac{\int_{-W/2}^{+W/2} v_x T \, dy}{\int_{-W/2}^{+W/2} v_x \, dy} \,, \tag{7.13}$$

which for our geometry becomes,

$$T_b = \frac{3\chi Q''}{kv_0 W}\left[x + \frac{13}{560}\frac{v_0 W^2}{\chi}\right] + T_{in} \ . \tag{7.14}$$

We also require a form for the temperature along the wall T_w,

$$T_w = T(x,y)|_{W/2} \ ,$$

therefore,

$$T_w = \frac{3\chi Q''}{kv_0 W}\left[x + \frac{5}{48}\frac{v_0 W^2}{\chi}\right] + T_{in} \ . \tag{7.15}$$

We are now able to calculate the heat transfer coefficient, h, defined by

$$h = \frac{k}{|T_w - T_b|}\left.\frac{\partial T}{\partial y}\right|_{W/2} \ , \tag{7.16}$$

$$h = \frac{Q''}{|T_w - T_b|} \ . \tag{7.17}$$

On substituting in (7.17) for the relevant terms we find,

$$h = \frac{210}{51} \times \frac{k}{w} \ . \tag{7.18}$$

If we now cast (7.18) in terms of hydraulic diameter, D, which we know from (2.28) reduces to,

$$D = 2W \ , \tag{7.19}$$

for a 2D rectangular duct, equation (7.18) becomes,

$$h = \frac{420}{51} \times \frac{k}{D} \ . \tag{7.20}$$

So, for our 2D straight duct with constant heat flux boundary conditions at the wall the Nusselt number is,

$$Nu = \frac{hD}{k} = 8.235 \ . \tag{7.21}$$

The above result is the predicted value of Nusselt number in the Boussinesq-Oberbeck regime, for a fully developed flow/temperature profile at large distances of x. In fact it is possible to obtain an expression for Nu at all values of x (including the duct 'inlet' or 'entry') for the case of an assumed uniform distribution of temperature across the duct at $x = 0$ [60] .

Figure 7.2 shows the theoretical prediction (green line) for the development of Nusselt number along the channel [60]. The non-dimensionalised axial length parameter used to calibrate the abscissa is defined as,

$$x^{'} = \frac{(x/D)}{Re\,Pr} \ , \tag{7.22}$$

where D is the hydraulic diameter and x is physical distance along the channel. Note that figure 7.2 shows the solution in the *entry length*, the distance necessary for the flow to become fully developed (ie. subject to assumption (7.4), from an assumed uniform profile), to be in the order $x^{'} = 0.2$ [60].

The theoretical result expressed in figure 7.2 is an appropriate result by which we can evaluate our thermal LBGK simulations.

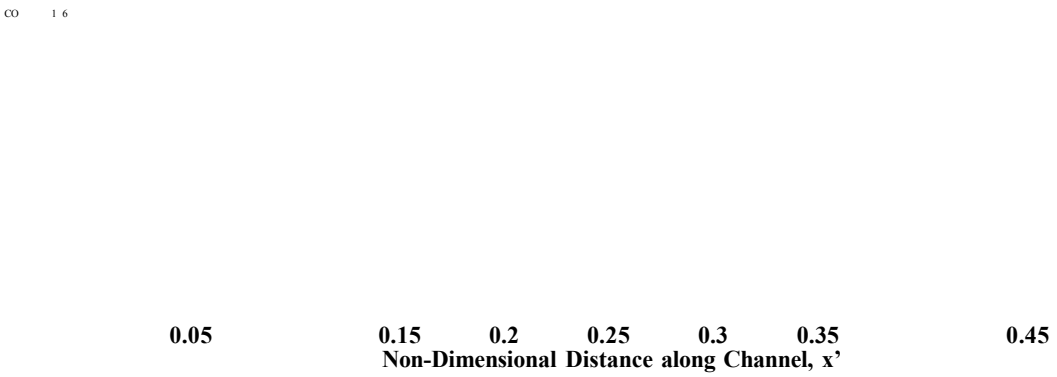

Figure 7.2: Axial development of Nu, entry length $x = 0.5$.

7.3 Simulation

Boussinesq flow assumes that fluid density is significantly influenced by the temperature but not the pressure field of the fluid. Also, in Boussinesq flow, temperature variation throughout the fluid is assumed to be small compared with the average value of that parameter (temperature). Therefore, to ensure that our test simulations remain within the Boussinesq-Oberbeck regime we must restrict the variation in internal energy parameter $e0$ to be small compared with its average value. This can be achieved by setting a large thermal conductivity (large thermal diffusivity)

through ω', which acts to limit the simulations transverse (cross-duct) internal energy (temperature) gradient.

Since we shall deliberately seek to restrict variation in our internal energy parameter to be small, in this and subsequent sections of chapter 7 we shall present results which refer to a normalised internal energy, defined by,

$$\varepsilon\phi'(x,y) = \frac{\varepsilon\phi(x,y) - \varepsilon\phi^{ref}}{\varepsilon\phi^{ref}} , \tag{7.23}$$

in which the reference energy, $\varepsilon\phi^{ref}$, is the arbitrary value of $\varepsilon\phi$ measured at the origin of the lattice co-ordinates (see figure 7.1) at steady state. This precaution also allows one to establish a simple correspondence with the temperature of the corresponding real system. We temporarily *superscript* lattice co-ordinates with an asterisk, then clearly,

$$\frac{\varepsilon\phi(x^*,y^*) - \varepsilon\phi^{ref}}{\varepsilon\phi^{ref}} = \frac{T(x,y) - T^{ref}}{T^{ref}} , \tag{7.24}$$

in which $T(x,y)$ is the absolute temperature which would be measured at position (x,y), equivalent (relative to the system boundary conditions) to a lattice location (x^*,y^*) and T^{ref} is the temperature at the centre of the duct, $(0^*,0^*)$.

Thus all quantities in figures 7.4 and 7.5 can, through equation (7.23), be interpreted as a normalised relative temperature change, which may be converted into a physical quantity after a single measurement of an appropriate reference temperature T^{ref}.

By trial and error the value of the thermal diffusivity was adjusted so that a typical variation in the internal energy variable, $\varepsilon\phi'$, is of the order 10^{-5}, safely within the Boussinesq-Oberbeck regime.

In terms of computational resource per simulation time-step our thermal scheme is little more demanding than the standard or EI LBGK schemes for our present application. Without buoyancy forces, there is no reciprocal influence of the temperature field upon the velocity field, although the latter would be simple to incorporate in the form of a body-force. This permits us to allow the LBGK momentum densities to evolve to an isothermal steady-state and thereafter to retain them in computer memory. Thermal evolution is then commenced, the energy (temperature) field being determined by the steady-state velocity field and the thermal boundary conditions (see section 7.3.1). Analagous practice is common in conventional CFD, to aid stability and to speed up convergence.

7.3.1 Boundary Conditions

In this subsection we consider the lattice closure conditions applied over the simulation lattice extremities.

First consider the momentum densities. The boundary conditions imposed at the horizontal walls, figure 7.1, on the velocity field are an extension of those used for the duct of section 5.3. We impose bounce-back conditions on the walls (remembering that the actual effective zero of velocity may lie a small distance away from the row in which the lattice closure rule is applied [25]).

Since we are using the standard LBGK momentum scheme, in driving the flow one is forced to resort to the usual approach of impressing a constant body force (using

a constant term in evolution equation [30]) throughout the fluid in order to simulate a driving pressure gradient [30, 50]. This device is perfectly accurate in a uniform duct and forces the momentum densities to a divergence-free velocity field along the duct. This allows use of wrap-around periodic conditions on the vertical walls of the simulation, leading to a velocity field consistent with an infinitely long duct.

Next we consider the boundary conditions applied to the internal energies. At the duct inlet ($x = 0$) the energy profile ($\varepsilon\emptyset$'s) was set to a constant value across the width of the duct. For the link energies, the individual $\varepsilon_{\sigma i}$'s were shared *pro rata* with the (known) momentum densities. In the geometries simulated the fully developed energy or temperature profile is expected to take the form of an inverted parabola (temperature being greater closer to the heated walls and lower in the duct centre - see (7.12)) however, published analytical results (see figure 7.2) with which we draw comparison in section 7.3.2, table the evolution of Nusselt number axially along the duct from a *uniform* inlet temperature profile / fully developed velocity boundary condition.

The outlet ($x = L_0$) boundary condition on the energy (temperature) field is based upon the gradient in energy along the duct. We expect (and do observe) a linear increase in all the $\varepsilon_{\sigma i}$'s along the duct, consistent with a linearly increasing average temperature (which results from constant flux boundary conditions). Obviously, the internal energies do not obey a periodic condition like the momentum densities. At the outlet, we extrapolate from the interior and we copy forward all the $\varepsilon_{\sigma i}$ values from $x = L_0 - 1$, then add to them an approximate gradient in $\varepsilon_{\sigma i}$.

We have chosen to simulate a system with constant heat flux at the walls and it should be noted that the thermal boundary may not necessarily lie in exactly the same plane as the no-slip velocity boundary. However, for a relatively wide duct it should be possible to minimise the effect of this error. With constant flux conditions the fluid in contact with the wall has to accept a fixed amount of energy injected, whatever the current value of energy content. We simulate this at all the wall nodes, firstly by allowing the link energies to bounce-back (according to the same prescription as their parent momentum densities in an isothermal simulation, see section 5.3 and [50]) each with an added (fixed) amount of energy. This process is applied at links with a component perpendicular to the modelled wall and facing into the fluid. This injection of energy totals the same at each node but is weighted by the relative momentum density on particular links. This seems a reasonable procedure consistent with our intuitive interpretation of the $\varepsilon_{\sigma i}$'s as internal energy. For, as we have already noted, in our thermal model energy is a passively advected scalar quantity so this method of applying constant flux boundary conditions associates energy pro-rata with the reflected momentum densities at a wall and represents the most obvious way for the fluid to accept the injected heat power. These conditions appear most satisfactory for the results presented in this chapter.

The energy field is uniformly initialised to a value equal to that set across the inlet boundary, each link being set to $\varepsilon_{\sigma i} = \frac{T_{in}}{9} \times \frac{N^{eq}_{\sigma i}(0)}{\rho}$, and the initial density at each node is set to $\rho = 1.8$. Although a given amount of energy is always being injected into the system per unit time, at steady-state the same amount of energy will be removed from the system as enters through the inlet and walls at each time step:

the total system energy, Etotai =]GVx (x,z), *reaching a steady-state constant value.* This is observed to occur at around 40,000 time steps (see figure 7.3).

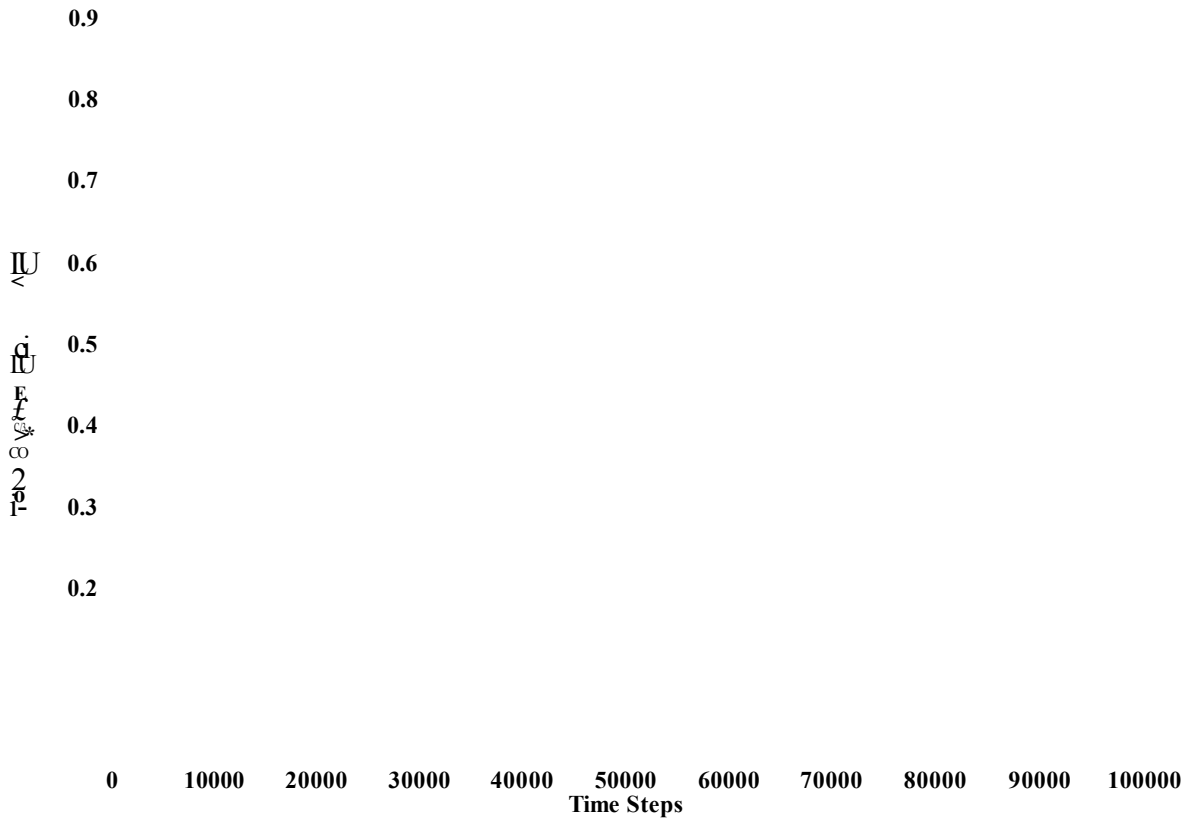

Figure 7.3: Total thermal LBGK energy as a function of time. Note that total system energy has been expressed in terms of A*E = (Etotai - E0)* where *E0* = lim*-^ *Etotai.* Here *E0* = 16199.52

The model is currently adapted to complement a standard LBGK scheme for momentum density evolution, but the Reynolds number in our particular system is not restricted: the uniformity of the system allows one accurately to use a uniform body-force to mimic the target uniform pressure gradient and thus to achieve high *Re* numbers without the compressibility errors we have noted in previous chapters, associated with actual LBGK pressure and density gradients. In any case, for the

results presented here we are interested in the temperature distributions not so much in the pressure drops.

7.3.2 Thermal LBGK Results

Of course the analytical results with which we aim to compare are valid only within the Boussinesq approximation. For the results we report in this section, body forcing (to generate flow) avoids density variation due to pressure gradients altogether. Moreover, as a glance at figures 7.4 and 7.5 will confirm, the relative variation in temperature (internal energy) is maintained small with our choice of parameters. And of course the scheme contains no viscous dissipation (coupling between advective and thermal modes), *by design.* So the results of this section are described by Boussinesq approximation and the analytical results of section 7.2 should apply. Nevertheless, as a check we shall show in this section that those assertions made in section 7.2 about the general form of the temperature field are valid. The results presented all apply to a duct of size 20×450, at a Re of 137.2 based on an hydraulic diameter of 38 lattice units, an average velocity of 0.0316, and $Pr = 0.16$ since $\chi = 1.5$ and $\nu = 1.9$, see equation (2.48).

Figure 7.4 shows that the energy field calculated by our thermal LBGK model does increase linearly along the length of the channel, except near the inlet where there is a short development or *entry* region. These curves are plotted as functions of energy, but, as the density field is constant ($\rho = 1.8\ \forall x, y$), and specific heat is assumed to be invariant with temperature, the actual temperature field of the lattice fluid will

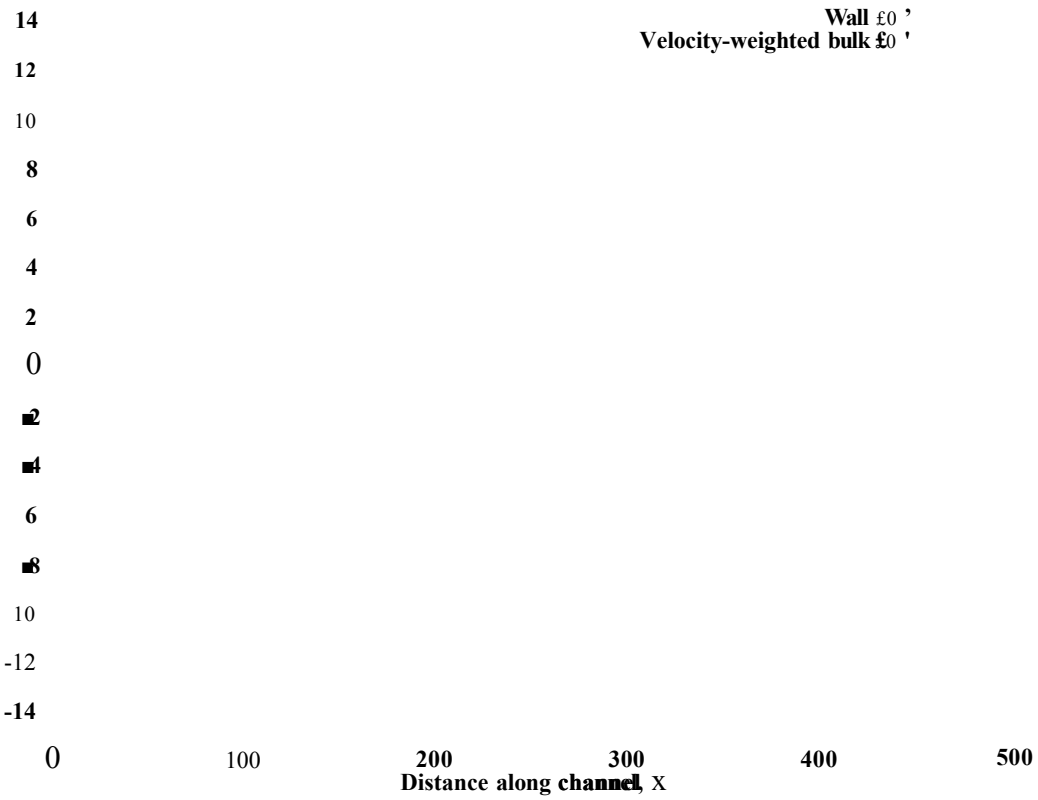

Figure 7.4: Blue line shows flow-averaged energy, green lines shows extrapolated wall energy for heated laminar duct flow problem. Note y-axis in terms of normalised energy variable, *£0 ,* as defined in (7.23). Here *£0reI* = 1.79986.

show that same quantitative behaviour (see mapping for *60* equation (4.76)). It is also useful to work in terms of energy variable *60,* as this is used to calculate LBGK Nusselt number directly, see equation (4.78).

Due to the nature of the simulation the value of *60* at a wall node is not simply related to the wall energy (temperature) - this is because the horizontal links at the wall do not form any part of the simulation and can take any value. It is safest to extrapolate from the interior in order to calculate the wall temperature. This is

achieved using simple a backward-difference, which appears to be sufficient for our purposes but tends to under-estimate the correct wall temperature.

The cross channel variation of *60* is also as expected. Figure 7.5 shows this to be parabolic, inverted if compared with the velocity profile, and is in agreement with the form derived analytically for $T(x,y)$ in equation (7.12). The line $Y = 1$ is the extrapolated wall energy. The energy field requires at least 40,000 time steps to

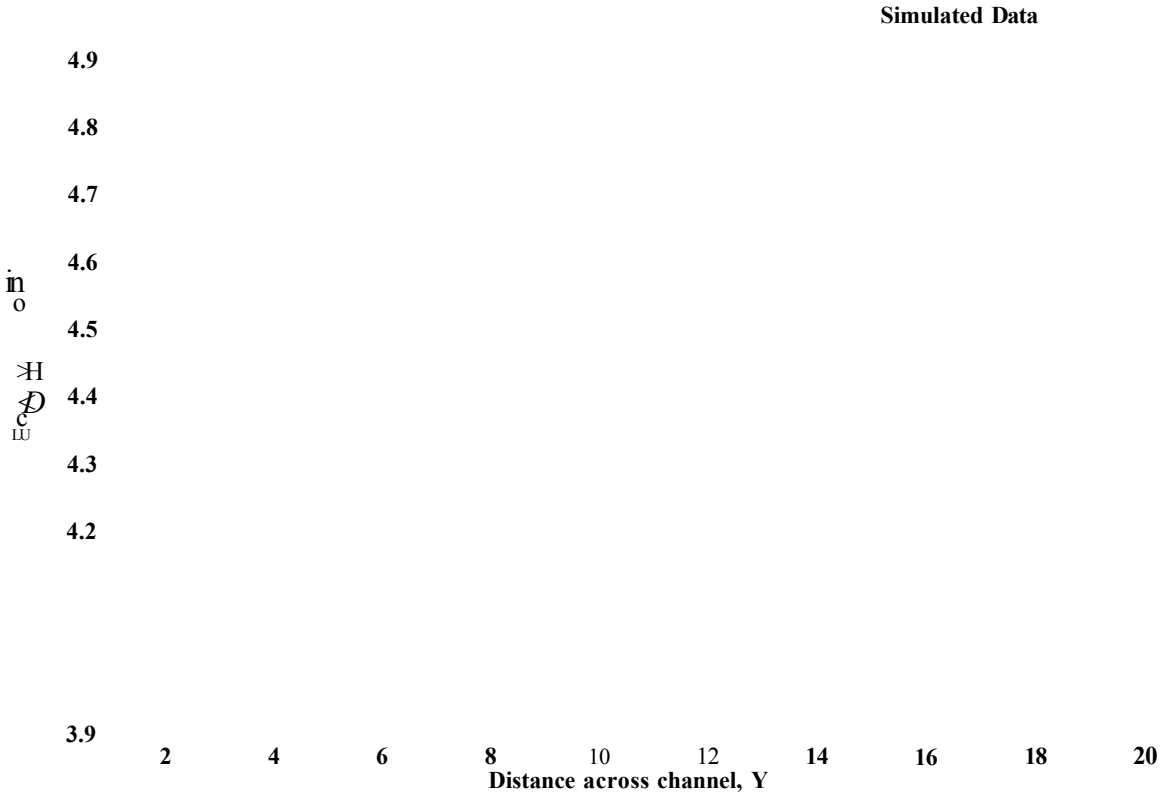

Figure 7.5: Graph showing typical cross-channel variation in 60, fitted to a parabola. Note that y-axis in terms of *£0* /10~5. Again, *£0reI* = 1.79986.

achieve a steady-state *Nu* number (see figure 7.6). This is a facet of the natural time scales of the physical processes (recall we use a large thermal diffusivity) and

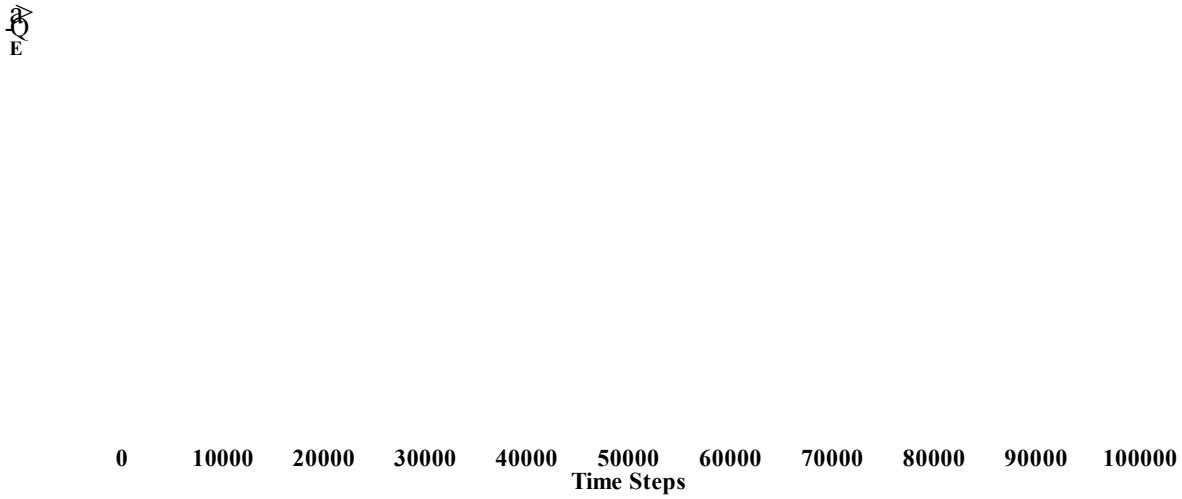

Figure 7.6: Time evolution of thermal LBGK Nusselt number.

to be expected for a model with correct physical time dependence.

As can be seen from figure 7.6 our LBGK simulation recovers a Nu of 8.243 which is in excellent agreement with the theoretical prediction of 8.235, see section 7.2. CFD also calculates a value of Nu reasonably close to the analytical one at 8.382 [59].

The value of Nu calculated by our thermal LBGK model appears to be insensitive to the value of heat flux, Q'', injected at the walls and the mass flow rate, which is as required.

The LBGK simulation's inlet energy condition is different from that applied in de-

riving the analytical solutions of figure 7.2, which apply away from the boundaries in an infinitely long channel. In an attempt to observe *entry length behaviour* we now consider how one might obtain a fully-developed uniform energy profile at a desired x. As we know from previous chapters one applies a closure rule and hopes that correct (target) behaviour develops as a result. In an attempt to allow a uniform temperature profile to develop across the duct *before* injecting a heat flux through the horizontal walls, we set zero flux at the walls in the duct entry region $0 \leq x \leq 49$, then inject a heat flux q between $50 \leq x \leq 450$. This effective shift of the x-origin for the heat-flux boundary conditions brings the axial development of thermal LBGK, in the region $x > 50$, into closer agreement with that predicted by theory (figure 7.2). Figure 7.7 shows the resulting axial development of thermal LBGK Nusselt number.

We can now use comparison with the known analytical solution, in the region $x \geq 50$, to assess where a *uniform initial profile* has developed in our simulation and take this position as our x-origin when calculating the non-dimensional axial distances. In our simulations a uniform temperature cross-section was taken to occur between $x = 49$ and $x = 50$. Figure 7.8 shows the axial development of both analytical and thermal LBGK Nusselt number in terms of dimensionless length parameter x' defined by a modified version of equation (7.22),

$$x' \approx \left(\frac{(x - 50)/D}{Re\, Pr} \right) . \tag{7.25}$$

It can be seen that, after the closure conditions have developed an approximately uniform cross-sectional temperature profile, our thermal LBGK model captures entry-

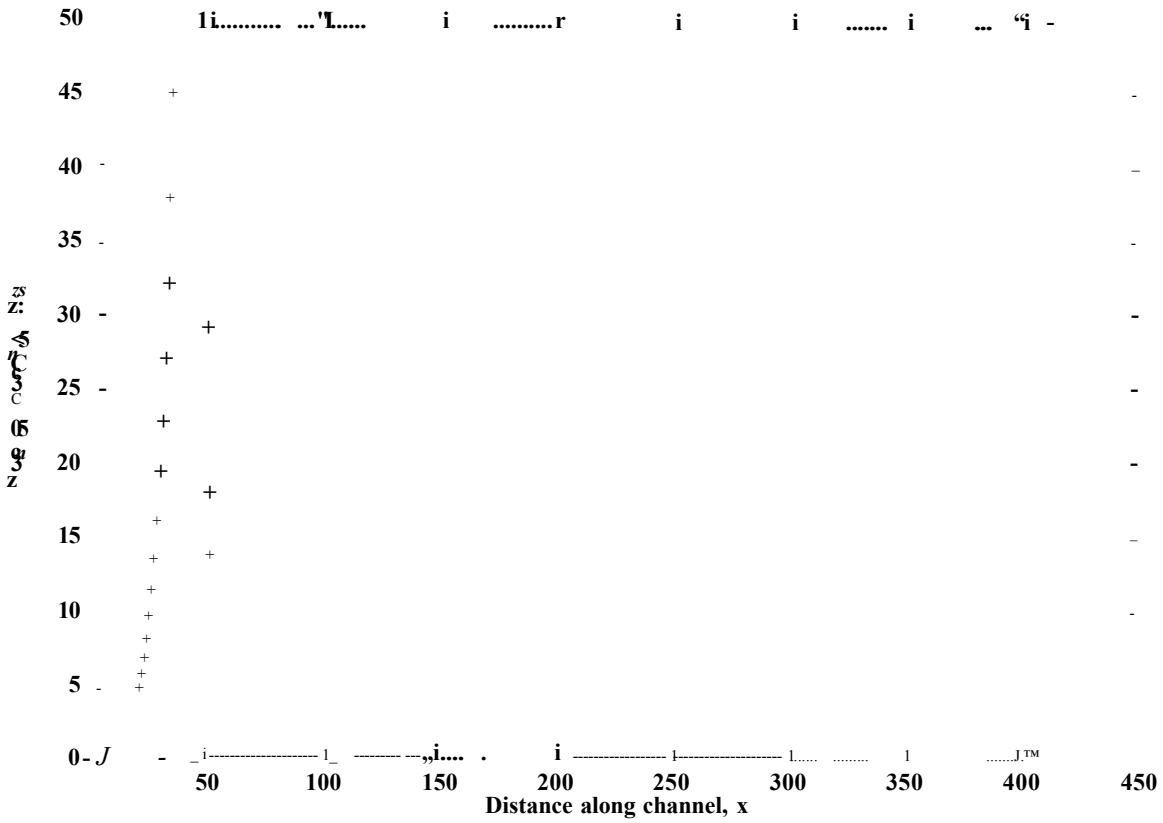

Figure 7.7: Axial development of measured LBGK Nusselt number.

length behaviour in reasonable agreement with theory.

7.4 Discussion and Conclusions

Using the thermal LBGK scheme developed in chapter 4 we have successfully simulated a forced convection flow problem. The Nusselt number, Nu, recovered from our test application is in very close agreement with the theoretical prediction and agrees well with data from more conventional CFD techniques. It has also been shown that the axial development of the Nu number agrees well with analytical

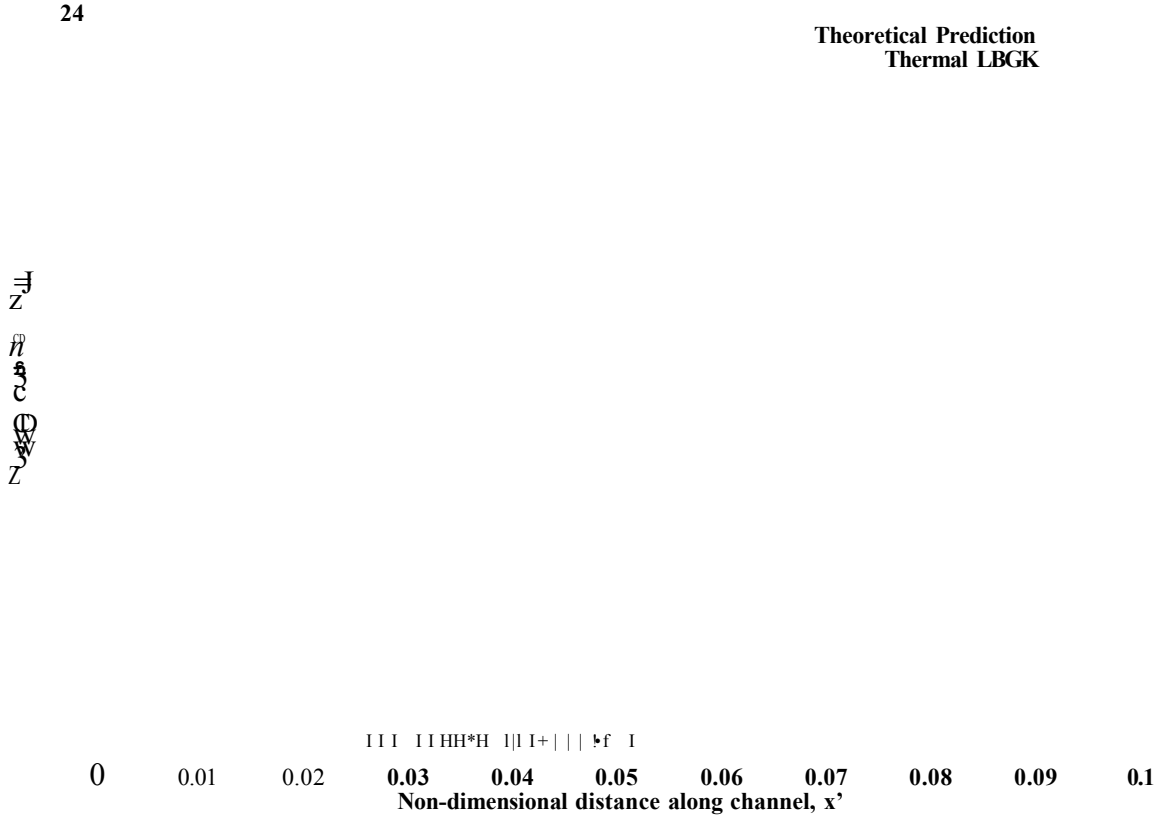

Figure 7.8: Axial development of Nusselt number. Solid line represents the analytical prediction, the crosses are our thermal LBGK results.

solutions.

The model appears to be as stable as isothermal LBGK schemes, which is not true of many other thermal LBGK models, and moreover, our model has easily adjustable thermal parameters. Whilst our scheme itself offers no real advantages over CFD for the present application, it is a simpler scheme than many of the existing thermal LBGK models and retains all the usual advantages of LB applications with more complicated boundary conditions.

There are a number of aspects to this promising work which warrant further investi-

gation. A more accurate extrapolation of the wall temperature would be worthwhile - at present the calculation of wall temperature is based on a backwards difference and tends slightly to underestimate the correct value. Also, the position of the thermal boundaries need to be located by analytical study of the model. This analysis is doubtless arduous and likely to produce only a small correction, but bearing in mind the encouraging results presented here probably worthwhile.

A potentially useful modification of the model would be to include pressure driven flows, since the current model behaves non-physically if pressure or density varies. This could probably be achieved by a modification of the equilibrium distribution.

Chapter 8

Conclusions and Future Work

8.1 Conclusions

In this thesis we have used LBGK models to achieve our aims as outlined in chapter 1. In particular, we have used an EILBGK scheme to simulate incompressible pressure-driven flows up to intermediate Reynolds numbers, and, two new schemes are introduced, allowing the calculation of depth-averaged flows and another the simulation of thermal flows within the Boussinesq-Oberbeck regime.

We showed in chapter 5 that it is necessary to use an EILBGK scheme if non-uniform pressure gradients are to be expected, and that careful consideration must be paid to the applied static wall boundary conditions to ensure that the correct pressure drops can develop. Flow in a straight duct was considered and the correct mechanical stresses were recovered at the walls, as measured by the friction factor.

A simulation of laminar pressure-driven flow over a backward-facing step yielded results in good agreement with other more usual numerical techniques. We suggest that to apply the standard scheme to this problem is logically inconsistent since one certainly cannot claim that the pressure decays uniformly along the channel (chapter 5) - see next section for further discussion.

In chapter 4 we developed an EILBGK scheme suitable for the simulation of depth-averaged flows. The assumption that the effect of the unmodelled surface can be approximated by a momentum sink consisting of stress terms alone is numerically validated in chapter 6. Application of our EILBGK depth-averaged model to a bifurcating duct is presented and again produces good qualitative agreement with CFD.

Using our thermal model (also introduced in chapter 4) we have successfully captured the correct Nusselt number for the forced convection flow problem of laminar flow in a straight duct with constant heat flux boundaries. Our model treats energy as a passively-advected scalar quantity, has (in principal) an adjustable Prandtl number and, we stress, is valid within the Boussinesq approximation. For the problem studied, entry length behaviour is also in good agreement with analytical predictions and traditional CFD calculations.

In general then, our primary aims have successfully been achieved, in that we have conclusively shown that LBGK models can be used successfully for the simulation of incompressible internal pressure-driven flows and certain flow regimes in which energy transfer is important. We have shown this to be true provided that the models

are carefully and appropriately bounded. Many interesting, and indeed unresolved, issues have arisen during the course of this work some of which are discussed in the next section.

8.2 Future Work

Lattice-Boltzmann methods, being a relatively immature technology in comparison with other numerical models used in the modelling of fluids, is beset by many unanswered questions. In this section we attempt to highlight key areas which deserve more thorough investigation, as a result of the work presented within this report.

As we know from previous chapters, LBGK simulations can be forced by applying body-forces, which is achieved by perturbing link densities uniformly over the lattice [30]. Applied to backward-facing step type geometries this approach can accurately represent the pressure upstream and downstream of the step, where the gradient in pressure is uniform, in an LBGK simulation with no compressibility effects. Close to the step the pressure field is non-uniform, but the velocity field can be investigated separately from the pressure field. Qian *et al* [44] have applied the standard LBGK scheme in this manner to the simulation of flow over a backward-facing step, of height equal to that of the narrow channel. Results reported in [44] are in better agreement with the experimental results of Armaly *et al* [55], than results presented in chapter 5 of this work with the experimental data of Denham *et al* [53]. This shows that whilst standard LBGK is susceptible to error if flow is forced via equilibrium

forcing, which is outlined in chapter 5, when pressure information is of interest, a standard LBGK calculation of velocity alone can generate data in good agreement with experiment if body-forcing is applied.

Consequently, future work should concentrate on a comprehensive assessment of the real merits of EILBGK versus LBGK applied to the problem of flow over a backward-facing step. This geometry is a suitable basis for such an exhaustive comparison because, as already noted in this work, there is a large body of experimental data available and the geometry results in a non-uniform pressure field. There should be a quantitative comparison between experiment, standard LBGK and EILBGK, applying to each scheme the most appropriate type of forcing over a range of *Re*. Any such work should be based on the data of [55] for the reasons outlined in the conclusions of chapter 5.

The restrictions imposed by the use of a regular lattice is partly responsible for many engineers' reluctance to accept lattice Boltzmann schemes as a useful tool for solving CFD type problems [40]. To be a truly useful tool, lattice Boltzmann methods will have to include irregular, unstructured and adaptive grids which are important in solving many real-life engineering flows which involve complex geometries [61]. The use of such grids can dramatically reduce the computational requirement by concentrating the distribution of lattice nodes in important areas of the flow domain and reducing the distribution elsewhere. In order to obtain this geometrical freedom it is necessary to interpolate between the particle positions calculated due to the discrete speeds and the sites of the irregular grid. Although this interpolation may

appear to introduce additional computational requirements, this is outweighed by the savings gained in terms of the number of nodes required. Also it is known that such methods may introduce *false* or *numerical* diffusion and warrants further investigation [61]. In [62] He *et al* propose a non-uniform grid algorithm suitable for implementation using a LBGK model, in which collisions take place at the grid points after which the densities move according to their velocities. The densities at the grid points is not now known but is calculated using interpolation. They apply this approach to a 2-dimensional symmetric sudden-expansion using both uniform and non-uniform rectangular grids and present results in good agreement with experiment. In [62] it is also stressed that their approach should be valid for arbitrary grids, although generating unstructured grids can be an extremely difficult and time-consuming task in itself. The so-called *interpolation-supplemented lattice Boltzmann* scheme has also been applied to the problem of vortex shedding behind a circular cylinder using a polar-circular grid [40]. Results are presented which show the method to be in good agreement with theory. Schemes incorporating body-fitted curvilinear grids are beginning to emerge [63] as are ones including adaptive meshes [64].

To allow LB models to be considered as practical tool for investigating industrial applications of practical importance such schemes have to be able to incorporate turbulent effects. Indeed suitable schemes are beginning to emerge in the literature [57]. A complete and comprehensive theory of turbulence does not exist and as a result turbulent flow predictions are generally based on semi-empirical models. A large range of scales are present in turbulent flows, and with present day computers

it has been shown that it is wholly impractical to simulate the full three-dimensional Navier-Stokes equations on fine enough grids to capture all relevant length scales for a realistic flow geometry, hence the need for such models. The direct numerical simulation (DNS) of turbulence was attempted using LB methods by Qian *et al* [14] and reported results in good agreement with theoretical predictions at high Re numbers. But this direct approach is, again, impractical due to time and memory constraints, and is the same for conventional CFD. Consequently, a subgrid-scale (SGS) model is required to simulate flows at very high Re. In 1995 Eggels *et al* [65] included the turbulent stress tensor directly in the equilibrium distribution, and in 1996 Hou *et al* [66] developed a SGS model based upon filtering the equilibrium distribution using a box filter to result in a space-dependent relaxation time. Results are presented for the simulation of two-dimensional cavity flow up to Re of 10^6 using a 256^2 lattice.

In conclusion, future work could productively concentrate on applying the above irregular grid and turbulence models to engineering geometries and again make exhaustive comparisons with both CFD and experiment in an attempt to highlight the areas in which a LB approach can be considered a most useful tool.

Appendix A

Calculation of Terms in LBGK Scheme

In this appendix we derive forms for the equilibrium distribution coefficients, $\Pi^{eq}_{\alpha\beta}$ and $\Pi^{(1)}_{\alpha\beta}$ as used in chapter 4.

To begin we sum the definition for the equilibrium distribution (4.5) over σ and i, and use the fact that A_σ, B_σ, C_σ and D_σ can only be dependent upon ρ to get the following two relationships,

$$A_0 + 4A_1 + 4A_2 = \rho \ , \tag{A.1}$$

and,

$$2C_1 + 4C_2 + D_0 + 4D_1 + 4D_2 = 0 \ . \tag{A.2}$$

To obtain a further relationship, we multiply (4.5) by $c_{\sigma i\alpha}$ and perform the usual

summation together with the relevant constraints to obtain,

$$\rho = 2B_1 + 4B_2 \ . \tag{A.3}$$

We now attempt to evaluate the term $\Pi^{eq}_{\alpha\beta}$, by substituting into its definition the general form for the equilibrium distribution (4.5), which yields

$$\Pi^{eq}_{\alpha\beta} = \left[2A_1 + 4A_2 + (4C_2 + 2D_1 + 4D_2)u^2\right]\delta_{\alpha\beta} + 8C_2 u_\alpha u_\beta + (2C_1 - 8C_2)u_\alpha u_\beta \delta_{\alpha\beta} \ . \tag{A.4}$$

The first term (enclosed in square brackets) on the rhs of (A.4) is identified with the pressure term in the hydrodynamic momentum flux tensor (2.16), in order to make this velocity-independent we choose,

$$4C_2 + 2D_1 + 4D_2 = 0 \ , \tag{A.5}$$

and to ensure Galilean invariance,

$$2C_1 - 8C_2 = 0 \ . \tag{A.6}$$

If we further choose,

$$8C_2 = \rho \ , \tag{A.7}$$

$$2A_1 + 4A_2 = c_s^2 \ , \tag{A.8}$$

where c_s^2 is the speed of sound, the LBGK momentum flux tensor is seen to have the correct form,

$$\Pi^{eq}_{\alpha\beta} = c_s^2 \rho \delta_{\alpha\beta} + \rho u_\alpha u_\beta \ . \tag{A.9}$$

The term $\Pi^{(1)}_{\alpha\beta}$ must also be evaluated to enable the $O(\delta^2)$ equations, section 4.1.4, to be fully derived. Substitute for $N^{(1)}_{\sigma i}$ in the definition of $\Pi^{(1)}_{\alpha\beta}$ using a rearranged

form of the first order equation (4.13) and then a further substitution for $N_{\sigma i}^{eq}$ is needed using (4.5). This results in,

$$\begin{aligned}\Pi_{\alpha\beta}^{(1)} &= -\frac{1}{w}\left[-c_s^2\delta_{\alpha\beta}\partial_\gamma(\rho u_\gamma) + \partial_{t_0}(\rho u_\alpha u_\beta) + \partial_\alpha(2B_1 - 8B_2)u_\beta\delta_{\alpha\beta}\right. \\ &\quad \left. +4\partial_\gamma(B_2 u_\gamma)\delta_{\alpha\beta} + 4\partial_\alpha(B_2 u_\beta) + 4\partial_\beta(B_2 u_\alpha)\right] , \qquad \text{(A.10)}\end{aligned}$$

and again to maintain isotropy the non-isotropic term is eliminated by setting,

$$2B_1 - 8B_2 = 0 . \qquad \text{(A.11)}$$

We now have enough information to calculate values for the coefficients B_1 & B_2,

$$B_1 = \frac{\rho}{3} , \quad B_2 = \frac{\rho}{12} . \qquad \text{(A.12)}$$

The second term inside the brackets in (A.10) can be re-written as,

$$\partial_{t_0}\rho u_\alpha u_\beta = -u_\alpha\partial_\beta(c_s^2\rho) - u_\beta\partial_\alpha(c_s^2\rho) - \partial_\gamma(\rho u_\alpha u_\beta u_\gamma) , \qquad \text{(A.13)}$$

which allows us to re-write $\Pi_{\alpha\beta}^{(1)}$ as,

$$\begin{aligned}\Pi_{\alpha\beta}^{(1)} &= -\frac{1}{w}\left[\left(\frac{1}{3} - c_s^2\right)\partial_\gamma(\rho u_\gamma)\delta_{\alpha\beta} + \frac{1}{3}\partial_\alpha(\rho u_\beta) + \frac{1}{3}\partial_\alpha(\rho u_\beta)\right. \\ &\quad \left. - u_\alpha\partial_\beta(c_s^2\rho) - u_\beta\partial_\alpha(c_s^2\rho) - \partial_\gamma(\rho u_\alpha u_\beta u_\gamma)\right] . \qquad \text{(A.14)}\end{aligned}$$

There is a certain amount of freedom in choosing the coefficients A_σ, although they must satisfy the constraints posed by equations (A.1) and (A.8),

$$A_0 = \frac{4}{9}\rho , \quad A_1 = \frac{1}{9}\rho , \quad A_2 = \frac{1}{36}\rho . \qquad \text{(A.15)}$$

At this stage the coefficients D_0, D_1 & D_2 remain undetermined. For all coefficients so far calculated, it is the case that for $\sigma = 2$ the expressions are a quarter of

those corresponding to the $\sigma = 1$ coefficient. Therefore, since there is still one free parameter it can be required that $D_1 = 4D_2$. Which leads to,

$$D_0 = -\frac{2}{3}\rho\,, \quad D_1 = -\frac{1}{6}\rho\,, \quad D_2 = \frac{1}{24}\rho\,. \tag{A.16}$$

Appendix B

Derivation of $\partial_\alpha \left(\sum_{i,\sigma} \varepsilon^{(1)}_{\sigma i} c_{\sigma i \alpha} \right)$

In this appendix we present the derivation for $\partial_\alpha \left(\sum_{i,\sigma} \varepsilon^{(1)}_{\sigma i} c_{\sigma i \alpha} \right)$ as presented in chapter 4.

Multiply the $O(\delta)$ equation (4.66) by $c_{\sigma i \alpha}$, ∂_α and perform the usual summation,

$$\partial_\alpha \partial_{t_0} \left(\varepsilon^{(eq)}_{\sigma i} c_{\sigma i \alpha} \right) + \partial_\alpha \partial_\beta \left(\varepsilon^{(eq)}_{\sigma i} c_{\sigma i \alpha} c_{\sigma i \beta} \right) = -\omega' \partial_\alpha \left(\varepsilon^{(1)}_{\sigma i} c_{\sigma i \alpha} \right) , \tag{B.1}$$

which is simply rearranged to give,

$$\begin{aligned} \partial_\alpha \left(\sum_{\sigma,i} \varepsilon^{(eq)}_{\sigma i} c_{\sigma i \alpha} \right) &= -\frac{1}{\omega'} \partial_\alpha \partial_{t_0} \left(\sum_{\sigma,i} \varepsilon^{(eq)}_{\sigma i} c_{\sigma i \alpha} \right) - \frac{1}{\omega'} \partial_\alpha \partial_\beta \left(\sum_{\sigma,i} \varepsilon^{(eq)}_{\sigma i} c_{\sigma i \alpha} c_{\sigma i \beta} \right) \\ &= -\frac{1}{\omega'} \partial_\alpha \partial_{t_0} \left(\varepsilon \emptyset u_\alpha \right) - \frac{1}{\omega'} \partial_\alpha \partial_\beta \left(\frac{\varepsilon \emptyset}{\rho} \sum_{\sigma,i} N^\dagger_{\sigma i} c_{\sigma i \alpha} c_{\sigma i \beta} \right) . \end{aligned} \tag{B.2}$$

The problem now becomes finding a form for term containing $N^\dagger_{\sigma i}$. To achieve this

we substitute the momentum density evolution equation and obtain,

$$\partial_\alpha \partial_\beta \left(\frac{\varepsilon \phi}{\rho} \sum_{\sigma,i} N_{\sigma i}^{\dagger} c_{\sigma i \alpha} c_{\sigma i \beta} \right) = \partial_\alpha \partial_\beta \left[\frac{\varepsilon \phi}{\rho} \sum_{\sigma,i} \left(N_{\sigma i} + \omega \left(N_{\sigma i}^{eq} - N_{\sigma i} \right) \right) c_{\sigma i \alpha} c_{\sigma i \beta} \right] ,$$

$$= \partial_\alpha \partial_\beta \left[\frac{\varepsilon \phi}{\rho} (1 - \omega) \sum_{\sigma,i} N_{\sigma i} c_{\sigma i \alpha} c_{\sigma i \beta} + \frac{\varepsilon \phi}{\rho} \omega \sum_{\sigma,i} N_{\sigma i}^{eq} c_{\sigma i \alpha} c_{\sigma i \beta} \right] . \tag{B.3}$$

On applying power series expansion to $N_{\sigma i}$(first term inside square bracket), we need only retain $N_{\sigma i}^{eq}$ term as any higher would result in a term of $O(\delta^3)$, and we are only interested in terms up to $O(\delta^2)$, this leaves,

$$\partial_\alpha \partial_\beta \left(\frac{\varepsilon \phi}{\rho} \sum_{\sigma,i} N_{\sigma i}^{\dagger} c_{\sigma i \alpha} c_{\sigma i \beta} \right) = \partial_\alpha \partial_\beta \left[\frac{\varepsilon \phi}{\rho} \sum_{\sigma,i} N_{\sigma i}^{eq} c_{\sigma i \alpha} c_{\sigma i \beta} \right] . \tag{B.4}$$

We recognise the summation term as the momentum flux tensor, for which we have already derived a form for see equation (A.9). Therefore (B.4) becomes,

$$= \partial_\alpha \partial_\beta \left[\frac{\varepsilon \phi}{\rho} \left(\frac{1}{c_s^2} \rho \delta_{\alpha\beta} + \rho u_\alpha u_\beta \right) \right] , \tag{B.5}$$

$$= \frac{1}{c_s^2} \partial_\alpha \partial_\alpha \varepsilon \phi + \partial_\alpha \partial_\beta \varepsilon \phi u_\alpha u_\beta . \tag{B.6}$$

Bibliography

[1] J. D. Anderson, *Computational Fluid Dynamics*, McGraw-Hill Inc. ,1995.

[2] U. Frisch, D. d'Humiéres, B. Hasslacher, P. Lallemand, Y. Pomeau, and J. P. Rivet, *Complex Systems*, 1 (1987) pp649–707.

[3] Y. H. Qian, D. d'Humiéres, and P. Lallemand, *Europhys. Letts.*, **17**(6) (1992) pp479–484.

[4] L. D. Landau, and E. M. Lifshitz, *Fluid Mechanics*, Pergamon Press, 1966.

[5] R. B. Bird, W. E. Stewart and E. N. Lightfoot, *Transport Phenomena*, Wiley, 1966.

[6] G. A. Bird, *Molecular Gas Dynamics and the Direct Simulation of Gas Flows* , Oxford University Press, 1994.

[7] X. He, and L-S. Luo, *Phys. Rev. E*, **55**(6) (1997) ppR6333–R6336.

[8] U. Frisch, B. Hasslacher and Y. Pomeau, *Phys. Rev. Letts*, **56**(14) (1986) pp1505–1508.

[9] J. Hardy, O. de Pazzis, and Y. Pomeau, *Phys. Rev. A*, **13** (1976) pp1949–1961.

[10] B. M. Boghosian, and W. Taylor, *Phys. Rev. E*, **52**(1A) (1995) pp510–554.

[11] S. Wolfram, *J. Stat. Phys.*, **45**(3/4) (1986) pp471–525.

[12] S. Chen, M. Lee, K. H. Zhao and G. D. Doolen, *Physica D*, **37** (1989) pp42–59.

[13] H. Benzi, S. Succi and M. Vergassola, *Physics Reports (Review section of Physics Letters)*, **222** (3) (1992) pp145–197.

[14] Y. H. Qian, S. Succi, and S. A. Orzag, *Ann. Rev. Comp. Phys.*, **3** (1995) pp195–242.

[15] G. McNamara, and G. Zanetti. *Phys. Rev. Lett.*, **61**(6) (1988) pp2332–2335.

[16] R. D. Kingdon, *AEA–InTec–1298 Report*, March 1993.

[17] F. J. Higuera and J. Jiménez, *Europhys. Letts.*, **9**(7) (1989) pp663–668.

[18] F. J. Higuera, S. Succi and R. Benzi, *Europhys. Letts.*, **9**(4) (1989) pp345–349.

[19] S. Chen, H. Chen and W. H. Matthaeus, *Phys. Rev. A*, **45**(8) (1992) pp5339–5342.

[20] A. K. Gunstensen, D. H. Rothman, S. Zaleski and G. Zanetti, *Phys. Rev. A*, **43**(8) (1991) pp4320–4327.

[21] P. Bhatnagar, E. P. Gross and M. K. Krook, *Phys. Rev.*, **94** (1954) pp511.

[22] C. Cercignani, *Theory and Application of the Boltzmann Equation*, Scottish Academic Press, 1975.

[23] J. D. Sterling and S. Y. Chen, *J. Comp. Phys.*, **123**(1) (1996) pp196–206.

[24] R. A. Worthing, J. Mozer and G. Seeley, *Phys. Rev. E*, **56**(2) (1997) pp2243–2253.

[25] R. Cornubert, D. d'Humiéres and D. Levermore, *Physica D*, **47** (1991) pp241–259, and later Ginzbourg and Adler, *J. Phys. II (France)*, **4** (1994).

[26] X. He, Q. Zou, L-S. Luo, and M. Dembo, *J. Stat. Phys.*, **87** (1997) pp115–136.

[27] P. A. Skordos, *Phys. Rev. E*, **48**(6) (1993) pp4823–4842.

[28] D. R. Noble, J. G. Georgiadis and R. O. Buckius, *J. Stat. Phys.*, **81**(1/2) (1995) pp17–33.

[29] T. Inamuro, M. Yoshino, and F. Ogino, *Phys. Fluids*, **7**(12) (1995) pp2928–2930.

[30] Q. Zou,S. Hou, and G. D. Doolen, *J. Stat. Phys.* **81**(1/2) pp319 (1995)

[31] Y. H. Qian and S. A. Orzag, *Europhys. Letts.*, **21**(3) (1993) pp255–259.

[32] Y. Chen, H. Ohashi and M. Akiyama, *Phys. Rev. E*, **50**(4) (1994) pp2776–2783.

[33] Y. H. Qian and Y. Zhou, *Europhys. Letts.*, **42**(4) (1998) pp359–364.

[34] Z. Lin, H. Fang and R. Tao, *Phys. Rev. E* **54**(6) pp6323 (1996) and references therein.

[35] F. J. Alexander, S. Chen and J. D. Sterling, *Phys. Rev. E*, **47**(4) (1993) pp2249–2252.

[36] Y. Chen, H. Ohashi and M. Akiyama, *J. Stat. Phys.*, **81**(1/2) (1995) pp71–85.

[37] G.R. McNamara, A.L. Garcia and B.J. Alder, *J. Stat. Phys.*, **81**(1/2) (1995) pp395–408.

[38] X. Shan, *Phys. Rev. E*, **55**(3) (1997) pp2780–2788.

[39] X. Shan, H. Chen, *Phys. Rev. E*, **47**(3) (1993) pp1815–1819.

[40] X. He, G.D. Doolen, *Phys. Rev. E*, **56**(1) (1997) pp434–440.

[41] S. Hou, Q. Zou, S. Chen, G. Doolen and A.C. Cogley, *J. Comp. Phys.*, **118** (1995) pp329–347.

[42] W. Miller, *Phys. Rev. E*, **51**(4) (1995) pp3659.

[43] L.S. Luo, *Int. J. of Mod. Phys.*, **8**(4) (1997) pp859–867.

[44] Y.H. Qian, S. Succi, F. Massaila and S.A. Orzag, *Fields Inst. Comms.*, **6** (1996) pp207-215.

[45] D.H. Rothman and J.M. Keller, *J. Stat. Phys.*, **52**(3-4) (1988) pp1119–1127.

[46] I. Halliday, C.M. Care, S. Thompson and D. White, *Phys. Rev. E.*, **54**(3) (1996) pp2573–2576.

[47] M.-L. Tan, Y.H. Qian, I. Goldhirsch and S.A. Orzag, *J. Stat. Phys.*, **81**(1/2) (1995) pp87–103.

[48] Y.H. Qian and S.A. Orzag, *J. Stat. Phys.*, **81**(1/2) (1995) pp237–253.

[49] D.H. Rothman, S. Zaleski, *Lattice-Gas Cellular Automata*, Cambridge University Press, 1997.

[50] D. M. White I. Halliday and C. M. Care, *Physica D* to appear.

[51] O. Behrend, R. Harris and P. B Warren, *Phys. Rev E*, **50**(6) (1994) pp4586.

[52] D. d'Humiéres, private communications based upon forthcoming publication, *"Efficient Lattice-Boltzmann calculations in porous media",D. d'Humiéres, L. Giraud and I. Ginzbourg.*

[53] M. K. Denham and M. A. Patrick, *Trans. Instn. Chem. Engrs*, **52** (1974) pp361.

[54] C. Young, *PhD. Thesis* , Rolls Royce & Associates, Derby 1996.

[55] B. F. Armaly, F. Durst, J. C. F. Pereira and B. Schönung, *J. Fluid Mech.*, **127** (1983) pp473–496.

[56] G. R. McNamara, A. L. Garcia and B. J. Alder, *J. Stat. Phys.*, **87**(5/6) (1997) pp1111-1121.

[57] S. Chen and G. D. Doolen, *Annu. Rev. Fluid Mech.*, **30** (1998) pp329-364.

[58] P. Pavlo, G. Vahala and M. Soe, *J. Comp. Phys.*, **139** (1998) pp79–91.

[59] A. C. Thompson, *Private Communication.*

[60] W. M. Rohsenow, J. P. Hartnett, and E. N. Ganic (editors), *Handbook of heat transfer fundamentals*, 2nd ed McGraw-Hill, 1985.

[61] S. Succi, *Physica A*, **240** (1997) pp221–228.

[62] X. He, L.-S. Luo and M. Dembo, *J. Stat. Phys.*, **129** (1996) pp357–363.

[63] R. Mei and W. Shyy, *J. Stat. Phys.*, **143** (1998) pp426–448.

[64] C. Kim and A. Jameson, *J. Stat. Phys.*, **143** (1998) pp598–627.

[65] J. G. M. Eggels and J. A. Somers, *Int. J. Heat and Fluid Flow*, **16** (1995) pp357–364.

[66] S. Hou, J. Sterling, S. Chen and G. D. Doolen, *Fields Inst. Comms.*, **6** (1996) pp151–166.